DISSERTATION

UNTANGLING SOURCES AND DEPOSITION OF AIRBORNE NUTRIENTS

Submitted by
Lillian E. Naimie
Department of Atmospheric Science

In partial fulfillment of the requirements
For the Degree of Doctor of Philosophy
Colorado State University
Fort Collins, Colorado
Fall 2025

Doctoral Committee:

Advisor: Jeffrey L. Collett Jr.

Emily V. Fischer
Russ Schumacher
Jill Baron
Megan Willis

ABSTRACT

UNTANGLING SOURCES AND DEPOSITION OF AIRBORNE NUTRIENTS

Deposition of excess nutrients, nitrogen (N) and phosphorus (P), can have negative impacts on ecosystem health. This work will focus on frontiers in reactive N (N_r) and P deposition and emissions. N_r deposition in the US has experienced a regime shift, due to effective NO_x emissions regulations, and is now dominated by reduced N (gaseous ammonia (NH_3) and particulate ammonium (NH_4^+)). Wet deposition of inorganic N_r is routinely measured by the National Atmospheric Deposition Program, and is of particular interest in sensitive ecosystems, including Rocky Mountain National Park (RMNP). Reduced inorganic N_r dominates wet N_r deposition in RMNP. Dry deposition of NH_3 is rarely quantified due to the complexity in simulating its bidirectional exchange with surfaces. Bidirectional NH_3 flux simulations require high time resolution NH_3 concentration and micrometeorology data, both of which are technically challenging, costly, and generally unavailable. Here, we test whether more commonly available biweekly NH_3 concentration data and meteorological reanalysis data can be substituted with acceptable results. Fluxes simulated with biweekly NH_3 concentrations, commonly available from NH_3 monitoring networks, underestimated NH_3 dry deposition by 45%. These fluxes were strongly correlated with 30-minute fluxes integrated to a biweekly basis ($R^2 = 0.88$), indicating that a correction factor could be applied to mitigate the observed bias. Application of an average NH_3 diel concentration pattern to the biweekly NH_3 concentration data removed the observed low bias. Annual NH_3 dry deposition from fluxes simulated with reanalysis meteorological inputs exceeded simulations using *in situ* meteorology measurements by a factor of 2.

Upslope flows driven by mountain-plains and synoptic-scale circulations frequently transport emissions from the Colorado Front Range urban corridor and nearby agricultural operations to RMNP. Spatial patterns of NH_3 in this NE Colorado source region, from both satellite (IASI, In-

frared Atmospheric Sounding Interferometer) and *in situ* observations, were strongly correlated with the number of animals in nearby confined animal feeding operations (CAFOs). Satellite observations reveal large increases over NE Colorado during the period 2013-2023, with increases over an agricultural region more than three times greater than over the Denver metro region. Decreases in particulate NH_4^+ formation, following emissions reductions in sulfur and nitrogen oxides, and increases in wildfire smoke are estimated to account for a small portion of the increase, which appears spatially to be dominated by increased emissions from agricultural sources.

The western US is home to additional agricultural regions, ecosystems that are sensitive to excess inorganic N_r deposition, and increasing wildfire frequency. The effects of changing agricultural and smoke emissions are quantified using oversampled data from the Cross-track Infrared Sounder (CrIS), at 2 km resolution, for the warm season when peak agricultural emissions and wildfire frequency occur. The largest total column NH_3 increases were associated with agricultural regions across the western US, ranging from a 1.5 to 4.8% increase per year. In the Colorado Front Range, the NH_3 concentration trend above the agricultural subregion averaged 2.7% per year, decreasing to 2.5% per year when periods of wildfire smoke were removed. Over Idaho's Snake River Valley, the NH_3 concentration trend of +1.5% per year did not change when smoke periods were removed. The spatial footprint of agricultural hotspots is increased by 7% per year across the western US from 2013 to 2023, a trend that may indicate expansion of agricultural activities, increasing lifetime of emitted NH_3, or both, with important implications for increased NH_3 deposition to nearby sensitive ecosystems.

Research on the deposition of P is much more limited than N deposition, despite potential ecosystem impacts. The US NADP network has not previously quantified wet P deposition, in part due to a lack of a suitably tested method for trace-level measurements of ionic phosphate (PO_4^{3-}). Flow injection analysis, a well-established technique for measuring PO_4^{3-} in surface water, is tested and optimized here for measurements down to $< 1\ \mu$g P L^{-1}. This technique was used to successfully quantify PO_4^{3-} wet deposition from precipitation and snowpack samples, with concentrations

ranging from below detection limit to 37.5 μg P L^{-1} in Colorado and Kentucky, laying important groundwork for a future national P monitoring effort.

ACKNOWLEDGEMENTS

I would like to thank my advisor, Jeffrey L. Collett Jr., for his mentorship and guidance through my PhD. Jeff gave me the freedom to pursue research topics that sparked my interest and demonstrated what it means to be a thoughtful and committed collaborator. I would like to thank Jeff for guiding me through the research and publication process. I would also like to thank my committee members Emily Fischer, Russ Schumacher, Jill Baron, and Megan Willis. I would like to especially thank Emily Fischer for her mentorship, thoughtful co-author contributions, and guidance during challenging moments. I would like to thank all of my other co-authors who contributed to the projects included in this work: Da Pan, Kimberley Corwin, Amy Sullivan, Lena Low, Katherine Benedict, John Walker, Aleksandra Djurkovic, Bret Schichtel, Karen Cady-Pereira, Michael Iacono, and Lauren Magliozzi. I would also like the thank the Atmospheric Science Department staff, including Sarah Tisdale, Heidi Hammon, Amanda Davey, and Nate Gronlund. For their support and encouragement, I would like to thank my parents, Tina and Chris, my brother, Nick, and my soon-to-be in-laws, Sam, Jeff, and Lisa. For helping me relieve stress in the mountains, I would like to thank my dog, Astrid. Lastly, I would like to thank my partner, Chloe, for cheering me on, bringing me lattes during long days, encouraging me to take breaks, and never letting me sleep in my office. This dissertation would not have happened without all of you, and I am incredibly grateful.

TABLE OF CONTENTS

LIST OF TABLES

LIST OF FIGURES

Chapter 1

Introduction

The global biogeochemical cycles of carbon (C), nitrogen (N), and phosphorus (P) are complex and interconnected systems that play a key role in the worldwide processing of nutrients in living organisms, atmosphere, land surface, and oceans. The carbon cycle is connected to ecosystem productivity, ocean acidification, air quality, and climate change (IPCC, 2022). The global cycles of N and P are coupled to the C cycle and have direct impacts of their own (Wang et al., 2020). N and P availability can be responsible for nutrient limitation in ecosystems, which places an important constraint on ecosystem productivity (Vitousek et al., 2010). The deposition of excess nutrients, reactive N and P, to ecosystems can have negative impacts on ecosystem health (Baron et al., 2000; Boot et al., 2016; Zhan et al., 2017). Reactive N and P refer to the chemical species that are readily bioavailable and will undergo reactions in the atmosphere. Primary emissions of gas-phase reactive N species can also play a key role in particle formation. In contrast, P is emitted predominantly in the particle phase (Ruttenberg, 2003).

Reactive N (N_r) deposition and the associated ecosystem impacts have been a major focus of worldwide research (e.g., Gao et al., 2019; Walker et al., 2019a; Driscoll et al., 2024). Through this research, critical loads have been established to estimate the level of N_r deposition that will result in negative ecosystem impacts (Baron, 2006; Ellis et al., 2013). These critical loads, however, only consider wet deposition of inorganic N_r while total N_r deposition typically considers wet and dry deposition of inorganic nitrogen species, including ammonia (NH_3), particle ammonium (NH_4^+), nitric acid (HNO_3), and particle nitrate (NO_3^-). Total N_r deposition may also include contributions from organic N compounds (e.g., peroxyacetyl nitrate (PAN), alkyl amines, and biologically relevant compounds such as amino acids and proteins). HNO_3 is formed in the atmosphere through the oxidation of primary NO_x emissions. Effective NO_x emission controls have effectively reduced wet deposition from oxidized-N species (HNO_3 & NO_3^-) and shifted the balance of wet deposition towards reduced-N species (NH_3 & NH_4^+) (Li et al., 2016; Walker et al., 2019a; Driscoll et al., 2024).

NH_3 is the main form of emissions of reduced-N to the atmosphere and is the primary alkaline gas in the atmosphere. NH_3 can form particulate NH_4^+ via reaction with acidic species, predominantly sulfuric and nitric acids (Behera et al., 2013). NH_3 is directly emitted from agricultural activities, traffic, wastewater treatment, and biomass burning (Walker et al., 2019b; Tomsche et al., 2023). The lifetime of NH_3 against dry deposition is on the order of minutes to hours, while particle NH_4^+ has a much longer atmospheric lifetime, which increases the likelihood of deposition to remote ecosystems (Aneja et al., 2001; Napari et al., 2002; Ianniello et al., 2011). The formation of fine particulate matter ($PM_{2.5}$) is a major concern because it is harmful to human health (Xing et al., 2016). Wet deposition of inorganic N_r is routinely measured by the National Trends Network (NTN) operated by the National Atmospheric Deposition Program (NADP). The dry deposition of NH_3 is rarely measured and remains a large source of uncertainty in total N_r deposition (Walker et al., 2019b). Dry deposition of particulate NH_4^+ is unlikely to play a large role in N_r deposition due to the long atmospheric lifetime (e.g., days to weeks) of $PM_{2.5}$ species against dry deposition.

NH_3 dry deposition has been previously estimated using inferential methods with an approximated deposition velocity (Beem et al., 2010; Benedict et al., 2013a). However, NH_3 flux processes include both emission from and deposition to the surface (Sutton et al., 1995). NH_3 fluxes are rarely measured but can be simulated with a few different bi-directional models (Massad et al., 2010; Zhang et al., 2010; Pleim et al., 2013). NH_3 fluxes can change quickly, both in sign and magnitude, under changing NH_3 concentrations or meteorological parameters.

To best capture the direction and magnitude of NH_3 fluxes, high-time resolution NH_3 concentration, and micrometeorological parameters are required. Unfortunately, NH_3 is difficult and expensive to measure at high time resolution. Biweekly passive NH_3 measurements can be made at significantly lower cost and have been implemented in long-term monitoring networks (Butler et al., 2016; Schiferl et al., 2016). Due to the high temporal variability in NH_3 atmospheric concentrations, however, these measurements may not be well-suited to NH_3 flux simulations (Shen et al., 2016; Schrader et al., 2018; Tanner et al., 2022). Flux tower micrometeorological measurements are similarly difficult and expensive to make. Reanalysis meteorological data are available for regions that may lack *in situ* measurements; however, the impact of using this data on NH_3 flux simulations is not well understood (Wichink Kruit et al., 2012; Schrader et al., 2018). High time resolution and biweekly NH_3 concentration data will be used to quantify the impact on NH_3 fluxes above a sub-alpine forest ecosystem in RMNP. Simulated NH_3 fluxes will also be compared using *in situ* micrometeorology and reanalysis meteorology to understand the impacts on NH_3 fluxes.

Approximately 80% of NH_3 emissions across the globe have been attributed to agricultural activities (Wyer et al., 2022). The two main sources of NH_3 from agriculture are nitrogen fertilizer application and livestock waste, both of which have significantly increased in the last 50 years (Lamarque et al., 2010). NH_3 is routinely measured in the US by the Ammonia Monitoring Network (AMoN) operated by the NADP (Puchalski et al., 2011; Puchalski et al., 2015). The network consists of approximately 100 sites; however, they are mostly in rural and remote areas. In northeast Colorado, a region of heavy agricultural development, a network of NH_3 measurements was deployed to understand the spatial and temporal variability in NH_3 concentrations across remote, agricultural, and urban source regions (Day et al., 2012; Li et al., 2016). Measurements were made using two-week integrated passive NH_3 samplers, installed approximately 1 meter above the surface. This measurement technique does not capture the diel pattern of NH_3 concentrations, which can be strongly influenced by temperature-driven emissions and a changing boundary layer. NH_3 concentration data are also available from satellites, which can bridge spatial gaps of *in situ* monitoring networks (Wang et al., 2023). Satellite retrievals are used to estimate total column NH_3 concentration, as opposed to the surface concentrations monitored by *in situ* sampling. The *in situ* NH_3 network and satellite data will be used to assess (1) how atmospheric NH_3 concentrations have changed from 2013 to 2023 over NE Colorado, an important source region for excess N_r deposition in Rocky Mountain National Park (Benedict et al., 2018), (2) if the observed trends differ between agricultural and urban source regions, and (3) attribute those changes to potential sources.

One source that may be contributing significantly to atmospheric NH_3 across the western US is wildfire smoke. After agriculture, wildfire smoke is the next largest source of NH_3 in the US. In the past decade, the frequency of wildfire smoke has increased across the US (Bray et al., 2018; Corwin et al., 2022). Wildfires typically occur during the spring and summer in the western US (Picotte et al., 2020), when NH_3 emissions from agriculture are also the largest. Increased NH_3 emissions from wildfire smoke could have a large impact on deposition in remote ecosystems because emissions are injected higher into the atmosphere (Lindaas et al., 2021), which increases the atmospheric lifetime against dry deposition. Pairing modelled wildfire smoke plumes and satellite retrievals of NH_3 will allow for the impact of wildfire smoke to be removed from the NH_3 data record. Using this data, the increase in atmospheric NH_3 attributed to wildfire smoke will be quantified in the western US. Understanding the changing NH_3 emissions in the region will inform the expected changes to N_r deposition and potential ecosystem impacts.

In contrast to N_r deposition, there is limited research looking at P deposition. Excess deposition of P likely also results in harmful ecosystem effects in protected areas (Tipping et al., 2014; Brahney et al., 2015; Lynam et al., 2023). Ionic phosphate (PO_4^{3-}) is the main form of bioavailable P, or P that can be readily used by living organisms. To help fill this research gap, a new pilot P wet deposition sampling program has been designed in collaboration with the NADP, National Park Service, US Environmental Protection Agency, and the US Forest Service. However, a new technique for quantification of P in wet deposition will be required to measure sample concentration. Quantification of PO_4^{3-} deposition has not been previously included in routine US monitoring networks, like the NTN. This is due in part to the challenges associated with measuring P concentration at the low levels expected in wet deposition. Flow injection analysis is a common technique for measuring PO_4^{3-} in surface waters (Lyddy-Meaney et al., 2002, although it has not been used for measuring US wet deposition data, which typically have much lower concentrations.

Across this dissertation, open questions about the deposition and emission of NH_3 will be answered, and the wet deposition of PO_4^{3-} will be quantified. First, bidirectional NH_3 fluxes were simulated above a sensitive ecosystem to better understand the impact of substituting low-cost measurements and reanalysis data, where high time resolution *in situ* data are not available. This informs the application of bidirectional NH_3 flux models and the data requirements for future work. Next, a combination of satellite data from the Infrared Atmospheric Sounding Interferometer (IASI) and ground-based NH_3 data were used to understand the dominant sources and trends in atmospheric NH_3 in northeast CO. Satellite data were also used to assess changing NH_3 from agricultural activities and wildfire smoke across the western US, taking advantage of high-resolution oversampled data from the Cross-track Infrared Sounder (CrIS). Changes to the spatial footprint of high NH_3 concentrations inform the impact of changing NH_3 emissions for transport to sensitive ecosystems and particle formation. Lastly, a novel measurement technique is described for quantifying PO_4^{3-} wet deposition, and PO_4^{3-} wet deposition concentrations are reported from three test field sites in Colorado and Kentucky. The technique described can be used for future quantification of P wet deposition and the initial field measurements help set expectations for likely PO_4^{3-} concentrations in US wet deposition samples.

Chapter 2

Sensitivity of Simulated Ammonia Fluxes in Rocky Mountain National Park to Measurement Time Resolution and Meteorological Inputs

[1] Gaseous ammonia (NH_3) is an important precursor for secondary aerosol formation and contributes to reactive nitrogen deposition. NH_3 dry deposition is rarely quantified due to the complex bidirectional nature of NH_3 atmosphere-surface exchange and lack of high time-resolution *in situ* NH_3 concentration and meteorological measurements. To better quantify NH_3 dry deposition, measurements of NH_3 were made above a subalpine forest canopy in Rocky Mountain National Park (RMNP) and used *in situ* micrometeorology to simulate bidirectional fluxes. NH_3 dry deposition was largest during the summer, with 47% of annual net NH_3 dry deposition occurring in June, July, and August. Because *in situ*, high-time resolution concentration and meteorological data are often unavailable, the impact on estimated deposition from more commonly available biweekly NH_3 measurements and ERA5 meteorology were evaluated. Fluxes simulated with biweekly NH_3 concentrations, commonly available from NH_3 monitoring networks, underestimated NH_3 dry deposition by 45%. These fluxes were strongly correlated with 30-minute fluxes integrated to a biweekly basis ($R^2 = 0.88$), indicating that a correction factor could be applied to mitigate the observed bias. Application of an average NH_3 diel concentration pattern to the biweekly NH_3 concentration data removed the observed low bias. Annual NH_3 dry deposition from fluxes simulated with reanalysis meteorological inputs exceeded simulations using *in situ* meteorology measurements by a factor of 2.

---

[1] Naimie, L. E., Pan, D., Sullivan, A. P., Walker, J. T., Djurkovic, A., Schichtel, B. A., and Collett Jr., J. L.: Sensitivity of Simulated Ammonia Fluxes in Rocky Mountain National Park to Measurement Time Resolution and Meteorological Inputs, EGUsphere [preprint], https://doi.org/10.5194/egusphere-2025-1167, 2025.

2.1 Introduction

Gaseous ammonia (NH_3) is an important atmospheric constituent, with effects on atmospheric chemistry and the nitrogen cycle. Atmospheric deposition of reactive nitrogen (N_r) is linked to nitrogen oxides (NO_x) and NH_3 emissions. Emissions of NO_x and NH_3 have many potential fates including chemical transformation, dry deposition, particle formation, and wet deposition. Anthropogenic emissions of NO_x and NH_3 are produced predominantly by combustion and agriculture, respectively (Walker et al., 2019a), although there are also NH_3 emissions from traffic, wastewater treatment, and wildfires (Walker et al., 2019b; Tomsche et al., 2023). Due to increased food demand and industrialization, anthropogenic N_r has been increasing annually (Galloway et al., 2008; Kanakidou et al., 2016). Excess reactive nitrogen deposition has well-documented adverse effects on ecosystem health including eutrophication, soil acidification, decreased biodiversity, and increased N in freshwater bodies (Bobbink, 1991; Baron, 2006; Holtgrieve et al., 2011; Boot et al., 2016; Zhan et al., 2017; Pan et al., 2021).

As a result of effective NO_x emission controls, the balance of N_r wet deposition across the US has shifted from oxidized N-dominated to reduced N-dominated, and dry deposition of NH_3 at times dominates total N_r deposition (Li et al., 2016, Walker et al., 2019a; Driscoll et al., 2024). The National Emission Inventory (NEI) indicates that US NO_x emissions were reduced by 46% between 2013 and 2023, while NH_3 emissions increased by 13% (US EPA, 2020).

Critical loads, deposition levels below which harmful effects are not expected to occur, have been estimated for many ecosystems (e.g., Bowman et al., 2012; Schwede and Lear, 2014). In Rocky Mountain National Park (RMNP), a critical load of 1.5 kg N ha^{-1} yr^{-1}, based on wet deposition of NO_3^- and NH_4^+, has been established to avoid adverse effects on the ecosystem (Baron, 2006). The pre-industrial nitrogen load has been estimated at 0.2 kg N ha^{-1} yr^{-1} while the current deposition rate is as high as 3.65 kg N ha^{-1} yr^{-1}, approximately 15x the natural background and significantly higher than the critical load (Burns, 2003; CDPHE, 2007; Benedict et al., 2013a). Although the RMNP N_r critical load only considers wet deposition of NO_3^- and NH_4^+, dry deposition can also contribute significantly to total N_r deposition. NH_3 dry deposition in RMNP was estimated to be the third largest contributor to total N_r deposition, accounting for 18% of N_r deposition from November 2008 to November 2009 (Benedict et al., 2013a).

NH_3 dry deposition, however, remains a highly uncertain component of N_r deposition, and fluxes are rarely measured (Walker et al., 2019b). Previous studies in RMNP have estimated NH_3 dry deposition using unidirectional inferential models, where the NH_3 deposition velocity (V_d) was approximated as 70% of the HNO_3 deposition velocity (Beem et al., 2010; Benedict et al., 2013a; Benedict et al., 2013b) and NH_3 emission from the surface was ignored. In reality, NH_3 exchange between the atmosphere and surface is bidirectional, including deposition to and emission from the surface (Sutton et al., 1995). Several models have been developed to simulate the bidirectional exchange of NH_3 with the surface (Massad et al., 2010; Zhang et al., 2010; Pleim et al., 2013). Key model inputs include micrometeorology, soil and vegetation parameters, and atmospheric concentrations. In practice, fluxes can change quickly and even reverse direction with changing environmental conditions. Gaseous NH_3 is challenging and expensive to measure at high time resolution; lower-cost weekly or biweekly passive diffusion-based sampler measurements are more commonly utilized for long-term monitoring (Butler et al., 2016; Li et al., 2016; Schiferl et al., 2016; Hu et al., 2021). Previous efforts have used these low-cost measurements to quantify NH_3 dry deposition (Walker et al., 2008; Shen et al., 2016; Tanner et al., 2022). Detailed, high-time resolution meteorological observations at the location of interest are also desired when estimating dry deposition. Due to the frequent unavailability of such data, reanalysis meteorological data are often used as a substitute (Wichink Kruit et al., 2012; Schrader et al., 2018).

Schrader et al. (2018) investigated the impact of low time-resolution NH_3 concentrations on modeled fluxes. They found that using monthly NH_3 concentrations underestimates total NH_3 dry deposition. However, due to a linear relationship between simulations using monthly NH_3 concentrations and those using hourly NH_3 concentrations, they were able to generate a site-specific correction to compensate for the use of low time-resolution concentration data. Simulations were done using a simplified parameterization of the bidirectional exchange model described in Massad et al. (2010) and the NH_3 concentrations were simulated using the LOTOS-EUROS model (Hendricks et al., 2016).

Understanding and managing these biases could unveil opportunities to estimate NH_3 deposition when high-time resolution, *in situ* concentration, and meteorological observations are unavailable. Using high-time resolution NH_3 concentration measurements, we provide the first estimate of NH_3 annual dry deposition to an RMNP forest canopy using a bidirectional exchange model driven by high-time resolution NH_3 concentration data and *in situ* micro-meteorological measurements. We use *in situ* data collected in RMNP to determine if site-specific correction factors suggested by Schrader et al. (2018) apply to real-world observations and whether correction factors can be employed to reduce biases associated with NH_3 simulations using lower-cost, low-time resolution NH_3 measurements such as those available from the US Ammonia Monitoring network (AMoN) (Puchalski et al., 2011). We also tested if an average NH_3 diel pattern could be applied to reduce these biases and, if so, the length of measurements necessary to adequately describe the diel pattern. Finally, we examine biases introduced by substituting reanalysis meteorological data for high-time resolution *in situ* measurements.

2.2 Data and methods

2.2.1 Site location

Study observations were collected in RMNP in northern Colorado. The park, established to preserve the natural landscape, including montane, subalpine, and alpine ecosystems, is predominantly above 3000 m, where ecosystems developed under nutrient-deprived conditions and are therefore sensitive to excess nitrogen inputs. Nitrogen deposition has been a historical problem in RMNP; with diatom changes documented starting in the 1950s and more recent effects including eutrophication and changes to plant species (Baron et al., 2000; Korb and Ranker, 2001; Baron, 2006).

The area east of RMNP (Figure 2.1) includes a large urban corridor and extensive agricultural activity in the plains. The urban corridor of the Front range, spanning from Denver to Fort Collins, is a major source of nitrogen oxide emissions (Benedict et al., 2013b). The northeast plains of Colorado are predominantly agricultural and include major sources of NH_3 emissions from both animal feeding operations and crop production. The spatial pattern seen for feedlots is broadly consistent with the spatial distribution of other agricultural activities. Pan et al. (2021) found that 40% of summertime dry deposition of NH_3 in RMNP was associated with transport from agricultural regions to the east.

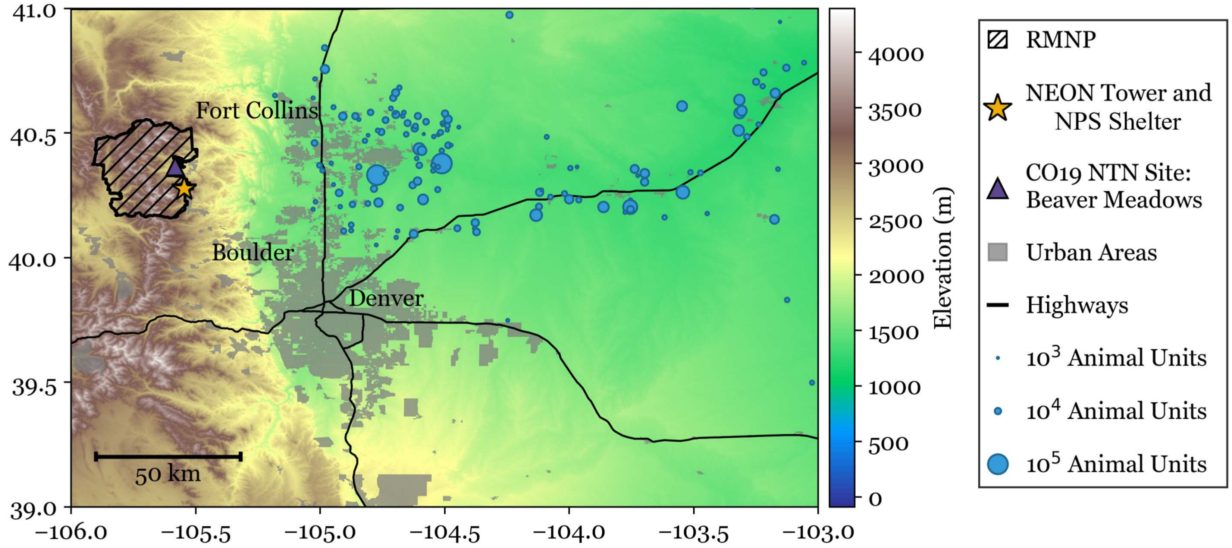

Figure 2.1: A map of the study region. Animal units are shown as the number of permitted animals as of 2017, scaled by an animal unit factor relative to the species. Elevation data are from the US Geological Survey Global Multi-resolution Terrain Elevation Data 2010 (GMTED2010) at 7.5-arc-second spatial resolution, or 225 m (available at: https://earthexplorer.usgs.gov/).

Data were collected at two adjacent locations for this study, both near the base of Longs Peak in Rocky Mountain National Park: a tower site of the National Ecological Observatory Network (NEON) (40.275903, -105.54596) and a nearby National Park Service shelter (~500 m north of the NEON tower), from September 2021 to August 2022. The study location, denoted with a star in Figure 2.1, is 2750 m above sea level. The tower is surrounded by lower montane forest, composed predominantly of evergreen needleleaf species, including ponderosa pine, juniper, and Douglas fir. There are also groves of quaking aspen in the region. Meteorological transport to the site is generally bimodal. The preceding downslope transport from the northwest occurs generally overnight and during the cooler months, when NH_3 concentrations are typically low. The mountain plains circulation generates daytime upslope transport, bringing air masses from the plains east of the park to RMNP. This pattern strengthens during warmer seasons. Periods of synoptically forced sustained upslope transport are also common, especially during spring and autumn (Gebhart et al., 2011). Downslope and upslope transport patterns are not due west and east at the study site because of channeling by local topography.

At RMNP, a diel pattern in ambient NH_3 concentrations has commonly been observed in past measurements. This pattern is primarily driven by changes in transport patterns that carry NH_3 emissions to the park (Benedict et al., 2013b; Juncosa Calahorrano et al., 2024) and, sometimes, modified by changes in the atmosphere-surface exchange of NH_3, especially during NH_3 uptake and emission from dew formation and evaporation (Wentworth et al., 2016).

2.2.2 Micrometeorological data

in situ micrometeorology

Meteorological and soil data were accessed from the RMNP NEON flux tower. The mean canopy height in the area surrounding the tower is 19 m. Temperature (mean = 6 °C), relative humidity (mean = 40%), and annual days of precipitation are highly variable at the site due to its high elevation. Mean values were calculated from September 2021 to September 2022. Snowfall typically occurs between October and May. The seasonal mean temperatures (relative humidities) are as follows: winter (December, January, and February) mean is -3 °C (30%), spring (March, April, and May) mean is 2 °C (44%), the summer (June, July, and August) mean is 15 °C (49%), and the fall (September, October, and November) mean is 8 °C (37%). Precipitation is measured at 1-minute resolution by a Belfort AEPG II 600M weighing gauge. Precipitation events were defined as periods of rainfall separated by at least one hour without precipitation. During our study period, there were 27 precipitation events in the winter, 62 in the spring, 63 in the summer, and 26 in the fall.

Meteorological data accessed from the NEON site includes wind vectors, friction velocity, Obukhov length, soil temperature, short wave radiation, relative humidity, air density, air pressure, and air temperature above the tree canopy. The meteorological observations used from the NEON tower are 30-minute mean values. Direct measurements of wind vectors, air temperature, short wave radiation, relative humidity, air density, and air pressure were used from the tower-top measurements (25 m-agl). 3D wind vectors were measured at 20 Hz using the CSAT-3 sonic anemometer (Campbell Scientific Inc., Logan, Utah, USA). Soil temperature was taken as the average across 5 collection sites within 200 m of the flux tower. Leaf area index (LAI) is estimated at the site using remotely sensed data. The square kilometer of leaf area index values surrounding the tower site is shown in Fig. S5. A mean value of 0.8 was estimated using the landscape surrounding the site. The sensitivity to LAI can also be found in section 5 of the supplementary information. Additional information about each of the reported NEON datasets can be found in the Site Management and Event Reporting documentation (available at: https://doi.org/10.48443/9p2t-hj77).

NEON meteorological data contained gaps due to power outages and scheduled instrument maintenance. Across the year of data, the gaps comprised 5.8% of the data (1021 data points). To quantify the annual deposition of NH_3 in RMNP, these gaps were filled using the average diel pattern of fluxes during the current biweekly NH_3 sampling period.

Reanalysis meteorology data

Detailed meteorological and soil data are not available at many locations where NH_3 dry deposition is of interest. Reanalysis data, which combine short-range weather forecasts with assimilated observations, are a common source of meteorological data that can be used in the absence of local observations. To probe the impact of using reanalysis data in place of *in situ* observations, a set of bidirectional flux simulations was conducted using ERA5 hourly reanalysis data (Hersbach et al., 2020). ERA5 hourly reanalysis data has a spatial resolution of 0.25 degrees, or approximately 30 km. The parameters used from the ERA5 data are as follows: air temperature, air pressure, dewpoint temperature, turbulent surface stress, moisture flux, sensible heat flux, friction velocity, standard deviation of filtered subgrid orography, solar radiation, and soil temperature. Obukhov length (L) is not given in the ERA5 dataset and was calculated using Eq. (2.1) from Stull (1988), shown below. Obukhov Length is the characteristic length scale of the atmosphere and is calculated from ERA5 data using instantaneous surface sensible heat and moisture fluxes based on the suggested calculation from the European Centre for Medium-Range Weather Forecasts (Gusti, 2024).

$$L = \frac{-\overline{\theta'_v} u_*^3}{kg\overline{(w'\theta'_v)}_s} \tag{2.1}$$

where k is the von Karman constant, g is gravitational acceleration, $\overline{\theta'_v}$ is the mean virtual temperature near the surface, $\overline{w'\theta'_v}$ is the surface flux of virtual potential temperature, and u_* is the friction velocity.

Where k is the von Karman constant, g is gravitational acceleration, tvst is the turbulent temperature scale, T_v is the virtual temperature and u_* is the friction velocity.

2.2.3 NH_3 data

Biweekly NH_3 measurements

Biweekly NH_3 ambient air concentration was measured using Radiello passive diffusion samplers purchased from Sigma Aldrich. The Radiello sampling system includes a diffusive body (part number: RAD1201) and an adsorbing cartridge (part number: RAD168) coated with phosphoric acid. NH_3 (g) diffuses across the exterior diffusive body and is collected on the adsorbing cartridge as ammonium (NH_4^+) over two weeks. Collected NH_3 (as NH_4^+) is extracted from the cartridge into deionized water and analyzed on a cation IC using a 20 mM methanesulfonic acid eluent (0.5 mL min^1) on a Dionex CS12A ion exchange column with a CSRS ULTRA II suppressor and Dionex conductivity detector (Li et al., 2016). NH_3 passive samples were collected in duplicate ($\sigma = \pm 0.25\ \mu$g m^{-3}) on top of the NEON tower (25.35 m-agl). Across the study period, there were 27 sampling periods. Due to site access issues, some samples had durations longer than 2 weeks. To create a consistent dataset, all data were aggregated to a 2-week average. In the case where two samples overlapped during a 2-week period, they were combined using a weighted average.

One sample was below the detection limit and was removed from this analysis. Passive NH_3 sampling methods have been shown to have a low bias when compared with other sampling methods, including annular denuders and Picarro Cavity Ringdown spectroscopy methods (Puchalski et al., 2011; Pan et al., 2020).

High temporal resolution NH_3 measurements

NH_3 (g) air concentration was also measured using an ion mobility spectrometer (IMS). Ion mobility spectroscopy separates ionized molecules based on their mobility through a carrier gas, under the influence of an electric field. The instrument used was the AirSentry II Point-of-Use IMS from Particle Measuring Systems (Boulder, CO). The instrument was in the National Park Service (NPS) shelter (located at 40.278129, -105.545635), 500 meters north of the NEON site, with an inlet located approximately 2 m above natural grassland. The sampling inlet was ¼” Teflon tubing, heated to 40 °C to reduce NH_3 loss to the sampling tube. Inlet length was kept as short as possible to further prevent NH_3 loss. Particles were removed by a fiber filter at the tip of the inlet. Due to the high altitude of the site location, the instrument was zeroed to account for pressure differences upon installation. Multi-point calibrations were conducted at the beginning and end of sampling. Calibration was confirmed using a known concentration ammonia gas sample split between the instrument and a phosphoric acid-coated denuder, where the NH_3 collected by the denuder is extracted into deionized water and analyzed using ion chromatography. Zero measurements were made periodically by overflowing the inlet with ultra-high purity clean air. The AirSentry samples at a 30-second frequency. During the study the AirSentry collected 919,000 data points. The limit of detection for 30-second measurementsis 70 pptv. For this data analysis, NH_3 concentration data were averaged to 30-minute mean values. Averaging data points increases the signal-to-noise ratio. We approximate that the signal-to-noise ratio increases proportionally to the square root of the number of samples ($n = 60$) (Dempster, 2001). In this case, the signal-to-noise ratio increases by a factor of 7.7, reducing the limit of detection to 9 pptv for 30-minute mean NH_3 concentrations. Across the year of data collection, 101 30-minute mean NH_3 points fell below the detection limit.

NH_3 data preparation

To investigate the effect of NH_3 (g) sampling time resolution, bidirectional fluxes were simulated with concentration data at: (i) 30-minute frequency (30-minute NH_3), (ii) with the 2-week integrated passive NH_3 (Biweekly Passive NH_3), and lastly with an average diel profile applied to each day within the 2-week passive period (Average Diel Pattern NH_3). The three NH_3 data products are shown in Figure 2.2.

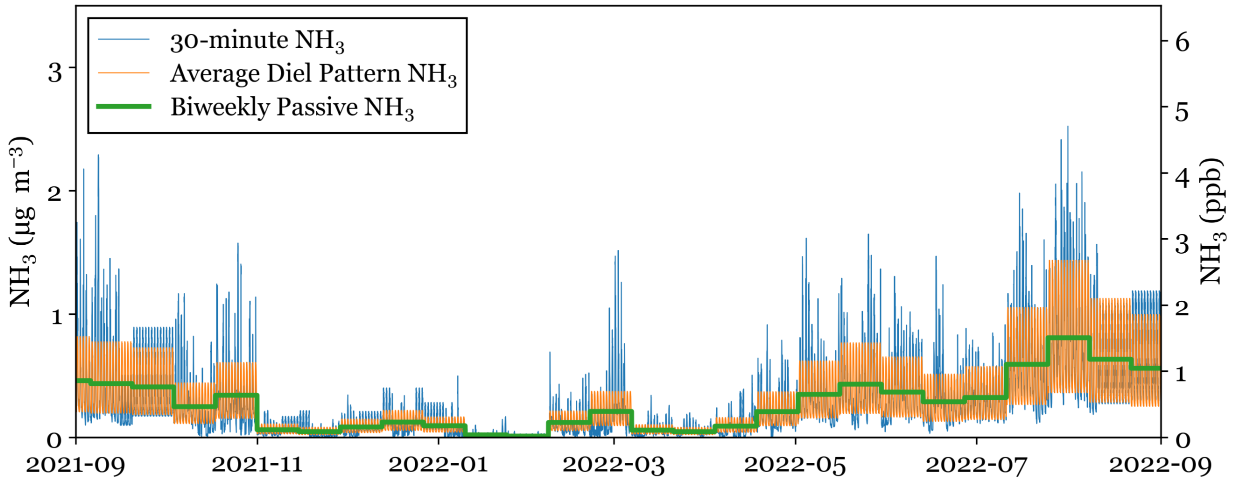

Figure 2.2: Three NH_3 concentration data sets are shown for the entire study period. The two-week average across each concentration data product is the same.

The 30-minute NH_3 concentration data are generated using a combination of data from the AirSentry NH_3 located at the NPS shelter and passive NH_3 samples collected on the NEON tower. Data gaps, due to power outages and regular maintenance, were filled using the average diel pattern across the year of data collection. Data gaps accounted for about 3000 points across the study period. To generate a 30-minute NH_3 data set above the tree canopy, the data were divided into biweekly periods which match the passive NH_3 collection periods. The average concentration from the AirSentry across each period was then scaled to match the biweekly passive NH_3 concentration. The 101 NH_3 concentration values below the AirSentry detection limit, representing 0.5% of the total measurement period, were assumed to represent a random distribution below the detection limit and retained for post-process scaling from the passive observations. This preserves the temporal variability of NH_3 concentrations while ensuring that the average air concentration across the sampling period is consistent with the passive NH_3 measurements atop the NEON tower which can differ from those above the adjacent grassland where the AirSentry measurements are made.

The biweekly passive NH_3 with diel profile applied is generated using the annual average diel pattern of NH_3 from the AirSentry data. To determine if there are systematic differences between the NH_3 diel pattern at the two sites, raw and scaled AirSentry concentrations were compared to 4- and 6-hour University Research Glassware denuder measurements taken on the NEON tower. The NH_3 concentrations were well correlated between sites. This comparison is shown in Fig. S1. To determine if there are systematic differences between the NH_3 diel pattern at the two sites, AirSentry concentrations were compared to 4- and 6-hour University Research Glassware denuder measurements taken on the NEON tower. The NH_3 concentrations were well correlated between sites. This comparison is shown in Figure A.1. Each day of the biweekly passive period is assigned the average diel pattern, and then the biweekly mean is scaled to match the biweekly passive concentration. This dataset was generated to investigate if the inclusion of a simple diel profile was sufficient to correct for the bias in bidirectional fluxes created by using low time-resolution NH_3 concentrations as shown by Schrader et al. (2018).

These three concentration data sets will be used for bidirectional flux simulations of NH_3. For the rest of this work, the three NH_3 data sets will be referred to using the following nomenclature.

- **30-minute NH_3**: NH_3 concentration data at 30-minute resolution
- **Biweekly NH_3**: Biweekly Passive NH_3 concentration data
- **Average Diel Pattern NH_3**: Passive NH_3 concentration scaled using an average diel profile from the 30-minute NH_3 dataset

2.2.4 Additional measurements

Wet deposition data

Weekly wet deposition data were obtained from the National Trends Network (NTN) (NADP, 2022) site at Beaver Meadows in RMNP ('CO19': located at 40.3639, -105.5810). The Beaver Meadows site location, at 2477 m elevation and located approximately 10 km north of the CASTNET site, is shown in Figure 2.1.

Additional gas and particle measurements

Additional air concentration data were obtained from the US EPA Clean Air Status and Trends Network (CASTNET) site at the NPS shelter ('ROM206': located at 40.278129, -105.545635). Weekly filter pack concentrations of nitric acid (HNO_3) and sulfur dioxide (SO_2) were used to calculate the acid ratio (Eq. 10) in the bidirectional exchange simulations of NH_3 (US EPA, 2024a).

Weekly dry deposition of HNO_3, NO_3^-, and NH_4^+ was generated by CASTNET (US EPA, 2024b) using the weekly filter pack concentrations and historical values of deposition velocity from the US EPA Multi-Layer Model (MLM) (Meyers et al., 1998). The generation of deposition velocities was discontinued in 2019. Bowker et al. (2011) found that using historical values of deposition velocity from the US EPA Multi-Layer Model did not significantly bias the annual mean of deposition.

One approach to estimating NH_3 deposition is to estimate the deposition velocity (V_d) as a fixed fraction (70%) of the deposition velocity of HNO_3, shown in Eq. (2.2). This approach has been historically used to estimate the dry deposition velocity of NH_3 in RMNP (Beem et al., 2010; Benedict et al., 2013a; Benedict et al., 2013b).

$$V_d(NH_3) = 0.7 * V_d(HNO_3) \tag{2.2}$$

2.2.5 Bidirection flux modelling of NH_3

Bidirectional NH_3 fluxes are simulated across the study period using the dry deposition inferential model described in Massad et al. (2010). This model was selected because it estimates both emissions and deposition of NH_3, uses a compensation point framework to capture these complex dynamics, and takes into account rapidly changing micrometeorology. The simulation framework (Figure 2.3) accounts for the bidirectional nature of NH_3 fluxes and allows for deposition and emission. The model determines if the flux will be negative (deposition) or positive (emission) based on the relationship between the atmospheric concentration (χ_a) at a given reference height (z) and the compensation point (χ_{z0}) at a defined distance (d) above the roughness length (z_0).

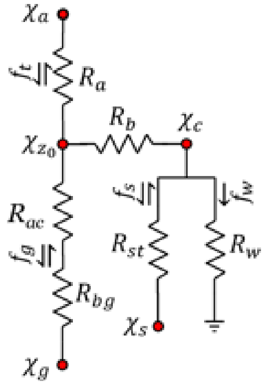

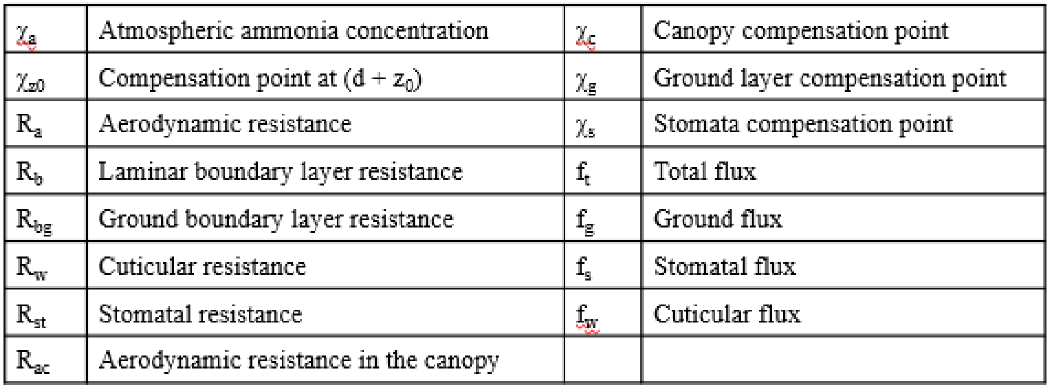

χ_a	Atmospheric ammonia concentration	χ_c	Canopy compensation point
χ_{z0}	Compensation point at (d + z_0)	χ_g	Ground layer compensation point
R_a	Aerodynamic resistance	χ_s	Stomata compensation point
R_b	Laminar boundary layer resistance	f_t	Total flux
R_{bg}	Ground boundary layer resistance	f_g	Ground flux
R_w	Cuticular resistance	f_s	Stomatal flux
R_{st}	Stomatal resistance	f_w	Cuticular flux
R_{ac}	Aerodynamic resistance in the canopy		

Figure 2.3: Dry deposition inferential model proposed in Massad et al. (2010). The table describes each model element. Arrows next to each flux show the allowed flux directions of the given pathway.

A conceptual diagram of resistances and compensation points is shown in Figure 2.3. Aerodynamic (R_a) and laminar boundary layer resistance (R_b) capture the effects of turbulent and diffusive transfer from the atmosphere to the surface, respectively. R_a was calculated according to Thom (1975), where z is 25.35 m, d is 7.15 m, and z_0 is 1.65 m. The stability functions are Ψ_H and Ψ_M for scalars and momentum, respectively, are empirical relationships dependent on L (Thom 1975). Displacement and roughness length were provided from the RMNP NEON Tower (NEON, 2023).

$$R_a = (ku^*)^{-1}(ln(\frac{z-d}{z_0}) - \Psi_H + \Psi_M) \tag{2.3}$$

R_b is modeled as described in Xiu and Pleim (2001), where γ_{air} is the kinematic diffusivity of air, and D_{NH_3} is the diffusivity of NH_3.

$$R_b = \frac{5}{u^*}(\frac{\gamma_{air}}{D_{NH_3}})^{2/3} \tag{2.4}$$

In-canopy resistance (R_g) is the sum of aerodynamic resistance within the canopy (R_{ac}) and ground boundary layer resistance (R_{bg}). R_{ac} was calculated based on Nemitz et al. (2001) using Eq. (2.5), where α is a height-dependent constant calculated using Eq. 16 and Eq. 17 from Massad et al. (2010).

$$R_{ac(d+z_0)} = \frac{\alpha_{(d+z_0)}}{u^*} \tag{2.5}$$

Ground boundary layer resistance (R_{bg}) is based on Nemitz et al. (2001), where u_g is the wind speed at the ground, which we approximate as 5% of the wind speed at tower top (25 m), and z_1 is the upper bound height of the logarithmic wind profile above the ground, which we approximate as 10% of the canopy height (Nemitz et al., 2001).

$$R_{bg} = (\frac{\gamma_{air}}{D_{NH_3}} - ln(\frac{D_{NH_3}}{k \times u_g \times z_1}))\frac{1}{k \times u_g} \tag{2.6}$$

Stomatal resistance (R$_{st}$) captures the diffusion of NH$_3$ through plant stomata and is calculated as a minimum value related to the plant type proposed by Hicks et al. (1987). Further parameterization proposed by Nemitz et al. (2001) was used here to calculate R$_{st}$, where SR (W m^{-2}) is the solar radiation (2.7). The minimum value for R$_{st}$ (225 s m^{-1}) was determined using Table 1 of Zhang et al. (2003), assuming 75% of the land surface was evergreen needleaf trees and 25% was deciduous broadleaf trees and shrubs.

$$R_{st} = min\{5000(sm^{-1}), 225(sm^{-1})(1 + \frac{180}{SR})\} \tag{2.7}$$

Cuticlar resistance (R$_w$) was calculated according to the proposed corrected parameterization for forest ecosystems predominantly composed of Douglas Fir, as described in Massad et al. (2010). When relative humidity (RH) is below 100%, Eq. (2.8) is used, and when RH exceeds or is equal to 100%, Eq. (2.9) is used.

$$R_w = (\frac{31.5}{AR})e^{0.0318(100-RH)} \tag{2.8}$$

$$R_w = \frac{31.5}{AR} \tag{2.9}$$

In both equations, AR is the acid ratio, which is calculated using the molar ratio of acids and bases in the atmosphere (2.10). The calculated acid ratio had a mean value of 1.3, a minimum of 0.22, and a maximum of 11.6. Acid ratios were the largest in the winter months.

$$AR = \frac{2[SO_2] + [HNO_3]}{[NH_3]} \tag{2.10}$$

For this study period, the acid ratio was calculated using weekly CASTNET measurements of SO$_2$ and HNO$_3$ paired with our measurements of NH$_3$.

Stomatal compensation points were calculated according to Massad et al. (2010). In the stomatal compensation point (2.11), Γ_{st} is the emission potential of the stomata and is approximated as 29 based on vegetation samples from the area surrounding the NEON Tower. The sampling methods and determination of this value can be found in the supplementary information. Emission potentials describe the potential for surface emission.

$$\chi_{st} = \frac{2.7457 \times 10^{15}}{T}(e^{-\frac{10378}{T}})\Gamma_{st} \tag{2.11}$$

Soil compensation point was calculated according to Eq. (3) through Eq. (5) of Stratton et al. (2018). In Eq. (2.12), TAN is the concentration of total ammonical N (the sum of NH_3 and NH_4^+) in the soil aqueous phase (mg kg^{-1}), KH is the Henry constant, and Ka is the equilibrium constant. TAN was estimated at 10.6 mg kg^{-1} based on soil measurements in RMNP from Stratton et al. (2018). NH_3 flux simulations are very sensitive to TAN value. Appendix A includes a test of the sensitivity of these flux results to TAN values within one standard deviation for the measurements taken by Stratton et al. (2018).

$$\chi_g = \frac{K_H}{1 + \frac{(10^{-pH})}{K_a}} \times TAN \tag{2.12}$$

K_H and K_a were predicted using Eq. (2.13) and Eq. (2.14) based on the models of Montes et al. (2009), where T is temperature.

$$K_H = \frac{0.2138}{T} \times 10^{(6.123 - \frac{1825}{T})} \tag{2.13}$$

$$K_a = 10^{(0.05 - \frac{2788}{T})} \tag{2.14}$$

Canopy compensation point, Eq. (2.15) below, was calculated using Eq. (12) from Massad et al. (2010), where χ_a is the atmospheric NH_3 concentration.

$$\chi_c = \frac{\chi_a(R_aR_b)^{-1} + \chi_{st}[(R_aR_{st})^{-1} + (R_bR_{st})^{-1} + (R_gR_{st})^{-1}] + \chi_g(R_bR_g)^{-1}}{(R_aR_b)^{-1} + (R_aR_{st})^{-1} + (R_aR_w)^{-1} + (R_bR_g)^{-1} + (R_bR_{st})^{-1} + (R_bR_w)^{-1} + (R_gR_{st})^{-1} + (R_gR_w)^{-1}} \tag{2.15}$$

Compensation point at the displacement height (d) above the roughness length (z_0) is calculated using Eq. (2.16) below as proposed in Massad et al. (2010). χ_{z_0} takes all other compensation points and resistances into account.

$$\chi_{z_0} = \frac{\frac{\chi_a}{R_a} + \frac{\chi_g}{R_g} + \frac{\chi_c}{R_b}}{\frac{1}{R_a} + \frac{1}{R_g} + \frac{1}{R_b}} \tag{2.16}$$

Finally, the total flux was calculated following Eq. (2.17) (Massad et al., 2010). NH_3 flux is defined in this framework as a difference between the roughness height compensation point and the NH_3 concentration at that height, scaled by the aerodynamic resistance.

$$F_{NH_3} = \frac{\chi_{z_0} - \chi_a}{R_a} \tag{2.17}$$

Total exchange flux (F_{NH_3}) from the dry deposition inferential model gives the direction and magnitude of NH_3 fluxes.

2.3 Results and discussion

2.3.1 Simulated bidirectional exchange of NH_3

Bidirectional fluxes were simulated using the 30-minute NH_3 concentration data set and *in situ* meteorological data as inputs to the Massad et al. (2010) model, described above. NH_3 concentration, roughness length compensation point, and fluxes have a strong seasonal cycle in RMNP (see Figure 2.4). NH_3 flux direction is determined by the relative magnitudes of the NH_3 concentration and the roughness length compensation point (Figure 2.4a). When NH_3 concentration exceeds the compensation point, NH_3 is deposited to the surface (a negative flux value). Both NH_3 concentrations and deposition fluxes tend to be greatest during the summer, with 48% of NH_3 modeled annual dry deposition occurring during June, July, and August. NH_3 fluxes also had the largest variability in the summer. Deposition in the spring closely follows, with 40% of NH_3 modeled annual dry deposition occurring during March, April, and May. During all seasons, there are periods of net emission from the surface (Figure 2.4b). The largest periods of net emission occur in

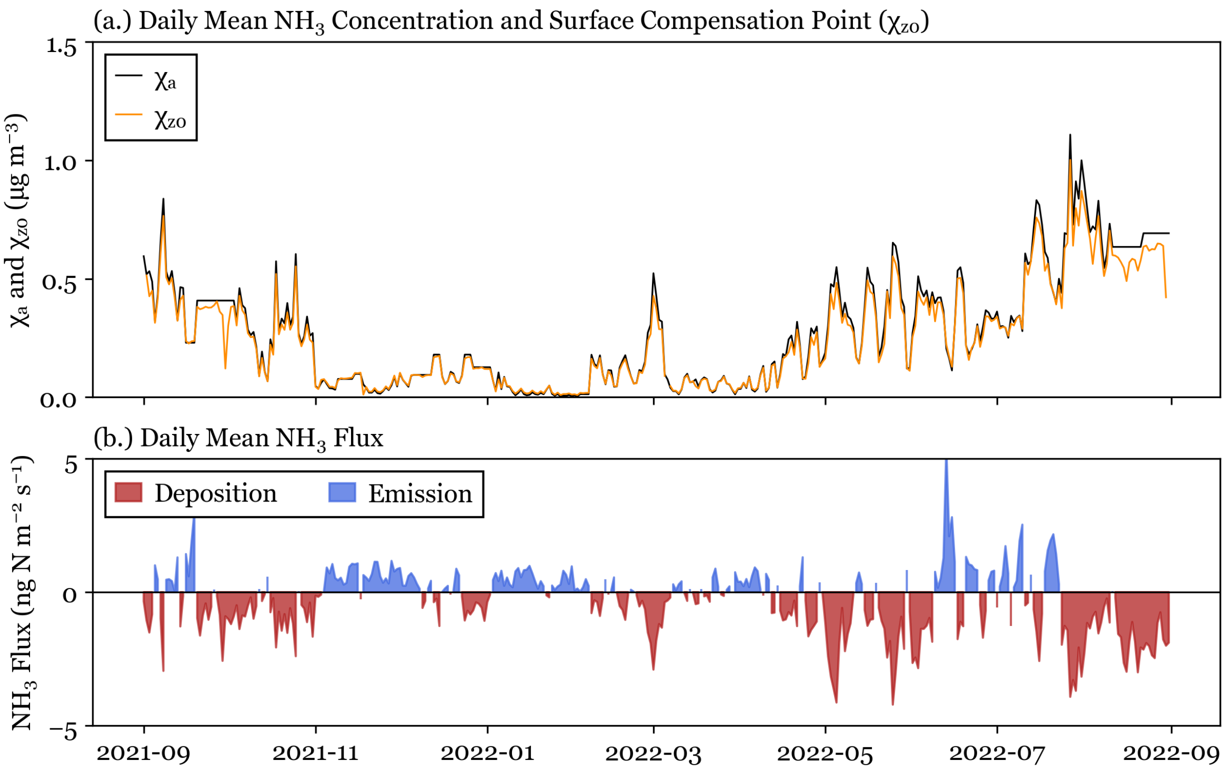

Figure 2.4: Daily mean values of: (a.) Daily mean NH_3 concentration and roughness length compensation point, and (b) NH_3 flux.

the spring. Daily NH_3 emission fluxes are most common in the winter where they are an order of magnitude smaller than typical deposition fluxes in the spring and summer.

Total modeled NH_3 flux can be broken down into stomatal, ground, and cuticular fluxes. Figure 2.5 shows the distribution of simulated NH_3 fluxes for each of these components. Deposition is driven primarily by stomatal and cuticular fluxes, while ground emission fluxes are sometimes observed. Winter periods of net emission (see Figure 2.4b) are driven by the ground flux. One potential limitation of the model used for simulations is that it does not consider snow cover on the ground, which could alter winter fluxes in RMNP.

NH_3 concentrations at RMNP are impacted by emission and transport patterns, which can both increase daytime NH_3 concentrations. NH_3 emissions from agricultural sources have a strong diel pattern driven by volatilization during warmer daytime temperatures. At RMNP, transport from these regions is driven on many days by the mountain-plains circulation, which begins in the late

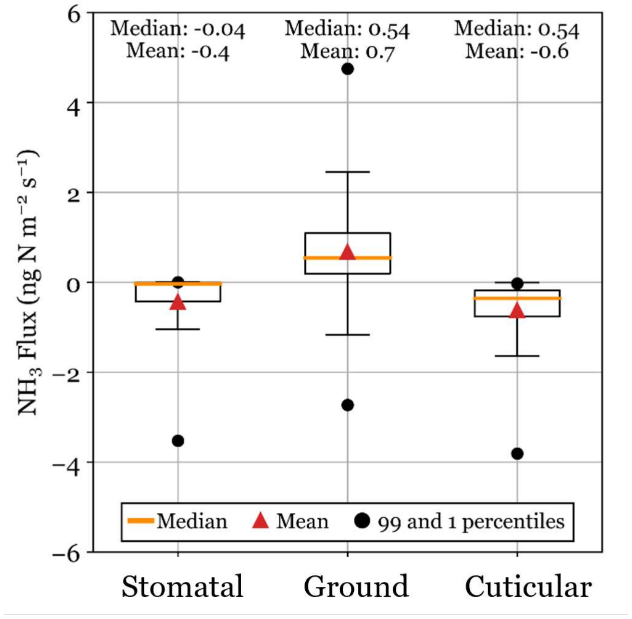

Figure 2.5: Total NH$_3$ simulated fluxes are separated into their component fluxes (stomatal, ground, and cuticular). Simulated fluxes are shown for the entire study period. Boxes show the 25th and 75th percentile, and whiskers are determined at 1.5 times the interquartile range.

morning and transports polluted air masses westward and upslope to the park (Gebhart et al., 2011). Previous studies have demonstrated that the upslope transport from sources in the Front Range has impacts on deposition and air concentrations in RMNP (Benedict et al., 2018; Pan et al., 2021). During this study, the largest χ_a values are also observed during upslope transport from source regions in the CO Front Range. These source regions likely disproportionately contribute to NH$_3$ dry deposition because the difference between χ_a and χ_{z_0} drives the sign and magnitude of the NH$_3$ flux. On mornings following overnight dew formation, local volatilization from evaporating dew has also been shown to increase morning NH$_3$ concentrations (Wentworth et al., 2016). This phenomenon was observed in RMNP and corresponds to the increase in the NH$_3$ diel pattern around 10:00 observed in Figure 2.6a. One limitation of the bidirectional flux model used is that NH$_3$ uptake and emission from dew are not simulated. NH$_3$ concentration, compensation point, and simulated fluxes each have a strong diel pattern, which peaks during the middle of the day (see Figure 2.6). The peak value typically occurs close to 13:00. The soil temperature diel pattern contributes to a higher roughness length compensation point during the middle of the day.

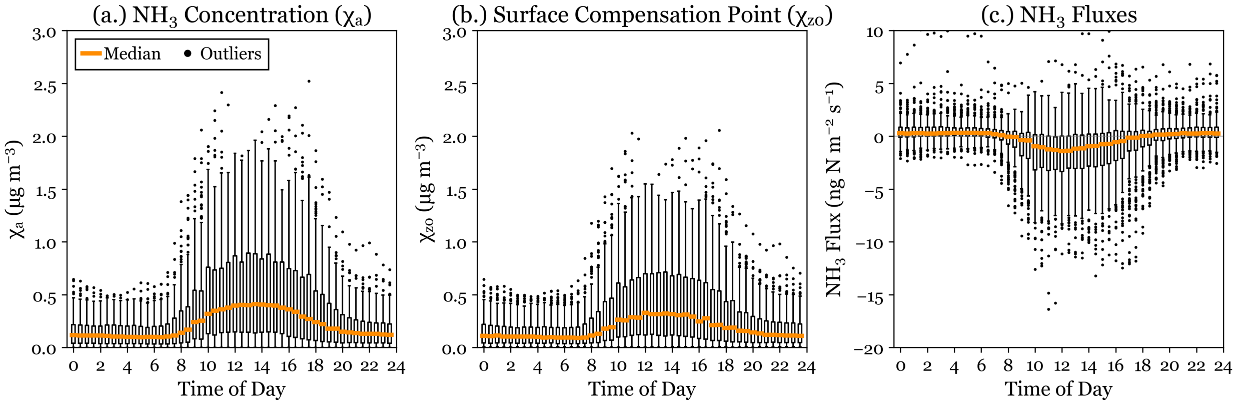

Figure 2.6: Diel pattern of: (a.) NH_3 concentration, (b.) simulated roughness length compensation point, and (c.) NH_3 fluxes are shown for the full study period in RMNP. Boxes show the 25^{th} and 75^{th} percentiles, and whiskers are determined at 1.5 times the interquartile range.

The annual cycle of soil temperature also contributes to the higher roughness length compensation points observed in summer. Although both NH_3 concentration and compensation point peak during the mid-day, we also observe peak fluxes during the middle of the day, indicating that the influence of the diel pattern of NH_3 concentration is stronger than that from the compensation point diel pattern.

To understand the relative importance of NH_3 deposition in RMNP, NH_3 flux simulation results are combined with NADP/NTN wet deposition fluxes and dry deposition fluxes for particulate ammonium (NH_4^+) and nitrate (NO_3^-) and gaseous HNO_3 derived from CASTNET concentration observations and MLM deposition velocities, to construct an updated seasonal and annual budget of inorganic N deposition at RMNP. This N_r deposition budget for all measured inorganic species is shown in Figure 2.7a. Due to the lack of current measurements, wet and dry deposition of organic nitrogen are not included. Benedict et al. (2013b) reported annual organic nitrogen wet deposition of 0.6 kg N ha^{-1} yr^{-1} during their 2008-2009 study. NH_3 dry deposition is the net surface flux from the simulations using 30-minute NH_3 concentration. The inorganic annual N_r deposition budget totals 3.4 kg N ha^{-1} yr^{-1}, with the largest contributions coming from NH_4^+ wet deposition (1.34 kg N ha^{-1} yr^{-1}), NH_3 net dry deposition (0.12 kg N ha^{-1} yr^{-1}), NO_3^- wet deposition (0.71 kg N ha^{-1} yr^{-1}), and HNO_3 dry deposition (0.33 kg N ha^{-1} yr^{-1}). Overall, reduced N_r deposition

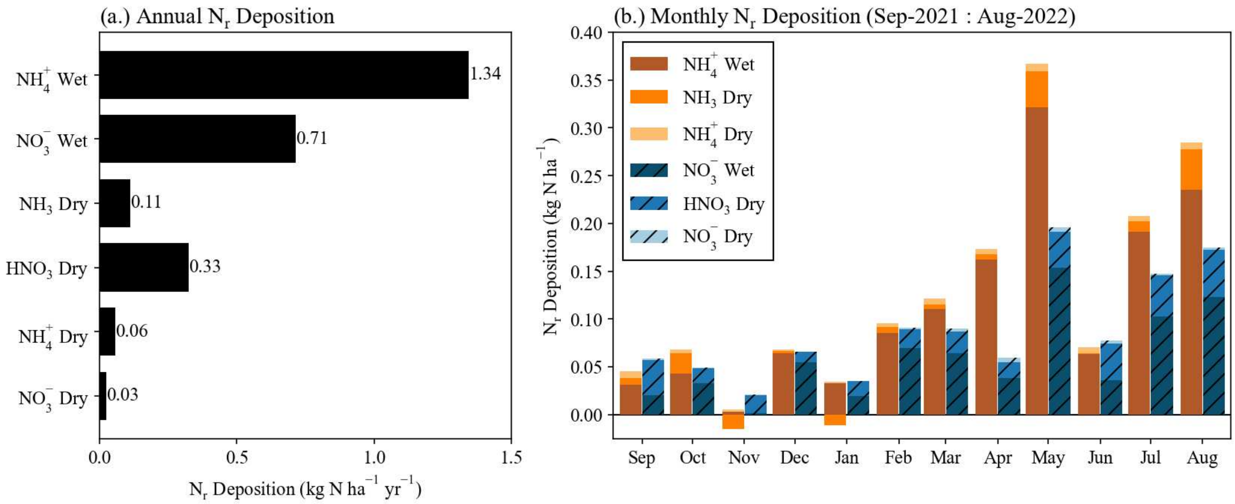

Figure 2.7: Reactive nitrogen deposition is shown for all species with measured concentrations or deposition for the full year of study. Wet deposition data are from the NADP NTN site at Beaver Meadows. NH_3 dry deposition is modeled using the bidirectional framework from Massad et. al (2010) and 30-minute NH_3 concentration data. Dry deposition of HNO_3 (g), NH_4^+ (p), and NO_3^- (p) are calculated from the nearby CASTNET site concentration data and deposition velocities from the US EPA MLM. Panel (a.) has the annual deposition of all measured species. Panel (b.) has deposition of all measured N_r species grouped by month. Reduced N species are green. Oxidized N species are blue. Only one period of wet deposition was collected by the NADP NTN site during November 2021.

comprises 59% of the total inorganic N deposition to RMNP. NH_3 dry deposition comprises 5% of total inorganic N_r deposition.

Speciated monthly dry deposition is plotted in Figure 2.7b to probe the seasonality of N_r deposition in RMNP. Net dry deposition of NH_3 was largest during July and August. Total inorganic N_r deposition peaked during May, due to increased wet deposition. Reduced N_r deposition exceeded oxidized N_r deposition in October, December, February, March, April, May, July, and August. Excluding November, where only one period of wet deposition was recorded by the NADP NTN site, reduced Nr deposition had a fractional contribution ranging from 43 to 74%. In November and January, net NH_3 emission was estimated from the surface.

2.3.2 Impacts of biweekly NH_3 concentration data on simulated fluxes

The use of low time-resolution NH_3 concentrations for flux simulations can produce a low bias compared with fluxes simulated using higher time-resolution NH_3 concentrations. Simulated

NH_3 fluxes have a strong diel pattern when simulated at 30-minute resolution (Figure 2.6), due to changes in NH_3 concentration and meteorology. These complex dynamics are averaged out when an average NH_3 concentration is used, which leads to an underestimation in deposition. Here, we demonstrate that a site-specific correction can be generated to account for the bias introduced by lower time resolution NH_3 concentration data. Our methods differ from Schrader et al. (2018) in 3 major ways: (i) *in situ* data are used for both the higher frequency, 30-minute NH_3 concentration, and meteorology, (ii) biweekly passive NH_3 data are used instead of monthly NH_3 data, and (iii) Massad et al. (2010) is used as described instead of using a simplified parameterization. The results of the 30-minute NH_3 and Biweekly NH_3 bidirectional flux simulations are compared to generate a site-specific factor to correct for any low bias in the lower time resolution flux calculations. Simulated fluxes at biweekly time resolution (Figure 2.8) using the two NH_3 concentration data sets are well correlated (R^2 = 0.88) and the NH_3 flux simulation using biweekly integrated NH_3 data can be corrected to match the control flux simulation using a linear fit (slope = 1.04, y-intercept = -1.647). As noted above, RMNP has few two-week periods of net NH_3 emission, and the efficacy of this method should be confirmed at a location with more extensive periods of net NH_3 emission. In particular, NH_3 fluxes above managed agricultural land could differ significantly from the pattern observed in RMNP. This study also focused on fluxes above a forest canopy, and results could differ for grassland ecosystems, which also occur in RMNP. To determine the efficacy in other locations, future investigations should select several sites with different land surface types and NH_3 concentrations to make biweekly and high-time resolution measurements for a year.

Considering the net flux of NH_3 across the full study period, using the best available time resolution of 30 minutes, we find a total annual net NH_3 dry deposition flux of 0.12 kg N ha^{-1} yr^{-1} (Figure 2.9). The estimated NH_3 dry deposition drops by 42% to 0.07 kg N ha^{-1} yr^{-1} using biweekly vs. 30-min NH_3 concentration measurements. The annual NH_3 dry deposition flux increases to 0.78 kg N ha^{-1} yr^{-1} when simulating fluxes in a deposition-only unidirectional framework where the NH_3 deposition velocity is scaled as 0.7 times the nitric acid deposition velocity

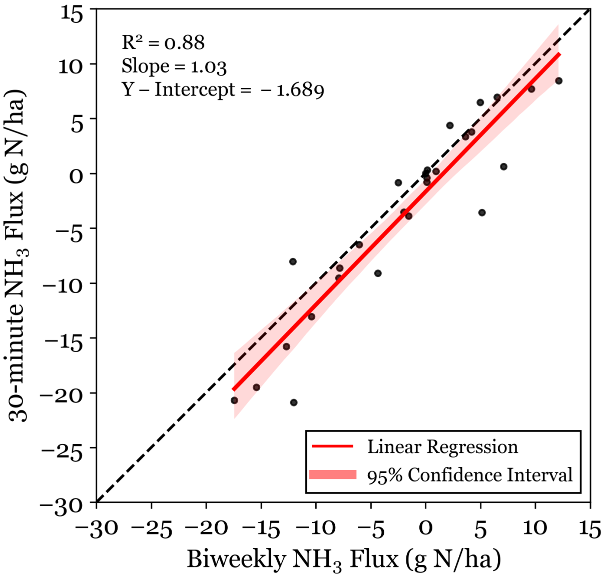

Figure 2.8: Bidirectional NH_3 flux simulated at 30-minute resolution is plotted for 30-minute NH_3 concentration data and biweekly integrated NH_3 concentration data. Fluxes are given as net flux over a two-week period. The least squares linear regression is plotted for the data.

(generated by the US EPA MLM), an approach previously used for RMNP N deposition budgets (Beem et al., 2010; Benedict et al., 2013a; Benedict et al., 2013b).

Bidirectional flux simulations using biweekly NH_3 data with an average diel pattern of NH_3 yield the same annual NH_3 dry deposition flux as the simulations run using 30-minute NH_3 concentration. This indicates that capturing daily variability in NH_3 concentration profiles is not critical to accurately simulating the annual NH_3 flux. Application of an annual averaged diel pattern misses the highest NH_3 concentrations (Figure 2.10), however, across a full year of data, the diel pattern effectively captures the net surface flux. Despite the scatter in Figure 2.10a., fluxes simulated with an average diel pattern NH_3 data set are well correlated with simulations using 30-minute NH_3 concentrations ($R^2 = 0.6$) and have a fit close to unity. The daily mean fluxes (Figure 2.10b and Figure 2.10c) of each simulation have similar seasonal patterns, with periods of net emission and deposition aligned between simulations.

At RMNP, there is a large daily variability in concentration due especially to changes in upslope transport. When an air mass arrives from the Colorado Front Range and NE Colorado, NH_3 concentrations rise significantly due to the large emission sources upwind. For the comparison

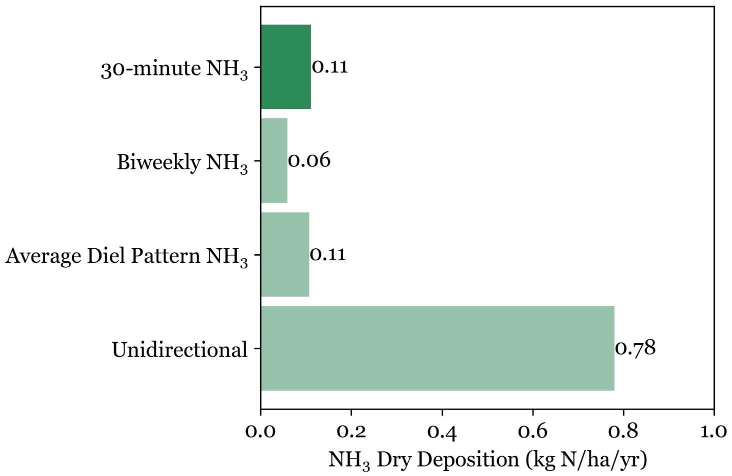

Figure 2.9: Annual NH_3 dry deposition at the NEON Flux Tower in RMNP is shown for three bidirectional simulations using three sets of NH_3 concentration data (30-minute NH_3, Biweekly NH_3, and Average Diel Pattern NH_3) and one unidirectional simulation. Each simulation was run at 30-minute time steps with meteorological parameters from the NEON Flux Tower. The unidirectional simulation uses biweekly NH_3 concentrations and deposition velocities based on the US EPA MLM.

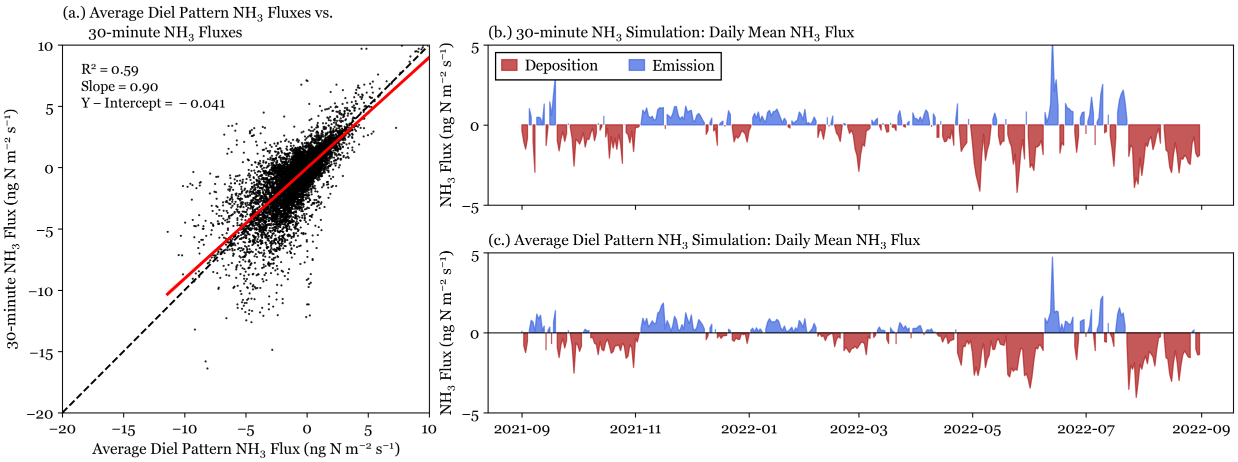

Figure 2.10: NH_3 fluxes simulated with 30-minute NH_3 concentrations and annual average diel pattern NH_3 concentrations are shown for the full year of data. Panel (a.) directly compares 30-minute simulated fluxes for each data set. Panels (b.) and (c.) show the daily mean fluxes for simulations with 30-minute NH_3 concentration and average diel pattern NH_3 concentration, respectively.

shown in Figure 2.10, the diel pattern was determined using a full year of NH_3 concentration data. Fluxes were also simulated using diel patterns determined with only a month of data, to probe the necessary length of measurements to generate an effective diel pattern. Annual deposition from all flux simulations using a monthly diel pattern fell within 2% of the annual deposition using the annual average diel pattern. Therefore, in RMNP, one month of 30-minute measurements appears sufficient to generate a diel pattern that will effectively correct the net NH_3 surface flux. Other locations may have larger variability in NH_3 diel pattern and may require longer periods of data collection to establish an effective NH_3 diel pattern.

2.3.3 Impacts of reanalysis meteorological data on simulated NH_3 fluxes

Dry deposition inferential models require several meteorological and soil parameters, which may not be readily available for many locations of interest. Reanalysis data can provide meteorological inputs for locations where required *in situ* meteorological and soil measurements are unavailable. To examine the impact on flux simulation accuracy resulting from this substitution at RMNP, the same simulations of NH_3 bidirectional fluxes were run using ERA5 meteorology and soil data. 30-minute NH_3 simulations run with reanalysis data inputs are well correlated ($R^2 = 0.77$) with 30-minute NH_3 simulations run with *in situ* data inputs (see Figure 2.11) but overestimate the annual NH_3 deposition flux by a factor of 2. From Figure 2.11, we find that the use of ERA5 reanalysis data in the simulation of NH_3 bidirectional fluxes introduces a low bias to the flux magnitude in RMNP compared to *in situ* meteorological data, for both positive (emission) and negative (deposition) fluxes. However, because the decrease to periods of deposition is larger than periods of emission, we observe an annual overestimation from simulations using ERA5. Based on this result, ERA5 reanalysis data should not be used to estimate NH_3 fluxes before additional sites and data have been considered using *in situ* data.

The low bias for fluxes simulated using ERA5 reanalysis data are investigated further to explore what parameter differences influence this bias. Net NH_3 fluxes are simulated using Eq. (2.16), which relies on χ_{z_0}, NH_3 concentration, and aerodynamic resistance (R_a). We find that

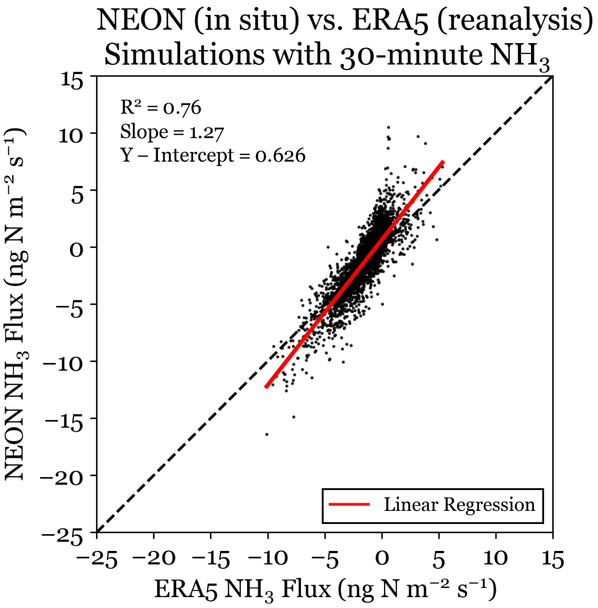

Figure 2.11: Bidirectional NH_3 flux simulated with ERA5 meteorology and NEON meteorology at 30-minute resolution using the 30-minute NH_3 concentration. The least squares linear regression is plotted for the data in red.

the simulations using reanalysis data generate roughness length compensation points (χ_{z_0}) which agree well with the simulations that used *in situ* measurements (Slope = 1.03, R^2 = 0.98).

Although the general diel pattern of R_a is well captured using reanalysis data, R_a magnitudes differ substantially between the two simulations (Figure 2.12a and Figure 2.12b), with the largest difference occurring overnight. Maximum R_a values from the reanalysis simulations are an order of magnitude larger than those derived using *in situ* meteorology. A comparison of the two data sets shows (Figure 2.12c) a typical enhancement of approximately a factor of four. Increased R_a values result in lower simulated NH_3 fluxes. The R_a bias is likely driven by differences in the friction velocity (u^*) and Obukhov Length, which are used to simulate R_a. ERA5 data underestimates u^* by a factor of 5 when compared with the *in situ* NEON data (slope = 0.2). The *in situ* NEON data also sets a minimum u^* value (0.2 m s^{-1}), while the ERA5 data allows u^* values below 0.2 m s^{-1}. Comparisons of all meteorological parameters used can be found in Appendix A. This discrepancy in modeled R_a may be due to the gridded nature of reanalysis data, which represents a large area of variable land types and complex topography using only a single value (Hogrefe et

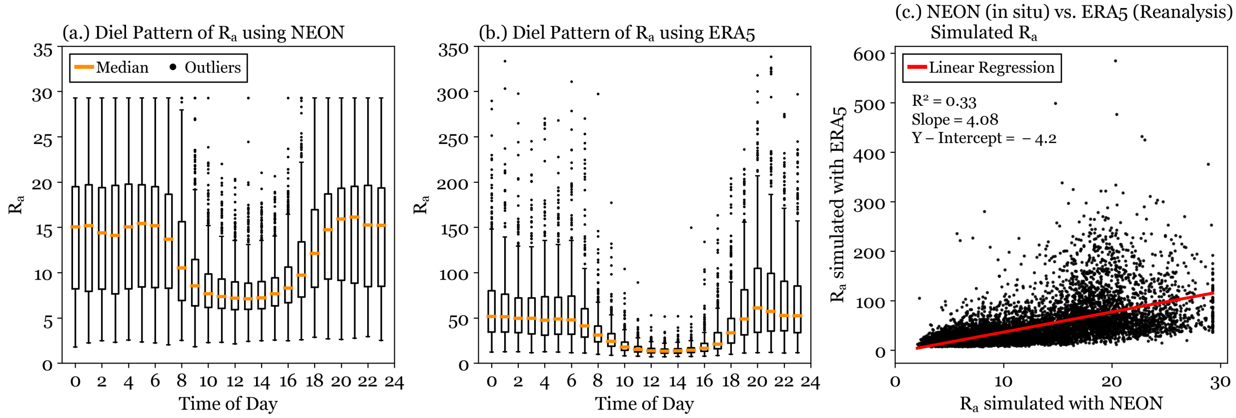

Figure 2.12: Aerodynamic resistances are shown for simulations using *in situ* meteorological data from the NEON flux tower and reanalysis meteorological data from ERA5. The diel patterns are shown in panels (a.) and (b.), respectively. Panel (c.) directly compares simulated R_a values using NEON *in situ* and ERA5 reanalysis data.

al., 2023). Obukhov Length is the characteristic length scale of the atmosphere and is calculated from ERA5 data using surface sensible heat and moisture fluxes. Previous work has identified heat and moisture fluxes as large areas of uncertainty in ERA5 Reanalysis (Kong et al., 2022; Mayer et al., 2022). Two case studies were conducted to probe the relative importance of u^* and Obukhov Length. The case studies are described in Appendix A. Differences in R_a were driven by Obukhov Length, accounting for 10% of the discrepancy between *in situ* and ERA5 flux simulations.

2.4 Conclusion

Fluxes of NH_3 (g) can be simulated using a bidirectional model, which uses rapidly changing meteorology paired with air concentrations and soil parameters to infer flux direction and magnitude. We use a bidirectional NH_3 flux model to simulate a year of NH_3 fluxes above a subalpine forest ecosystem in Rocky Mountain National Park. The net NH_3 dry deposition to the ecosystem is estimated at 0.11 kg N ha^{-1} yr^{-1}, comprising 5% of total inorganic reactive nitrogen deposition. This is significantly lower than previous estimates for RMNP, which did not consider the bi-directional nature of the exchange. Due to the observed low bias in passive NH_3 observations and the sensitivity of simulations to NH_3 concentrations, this is likely a low bound. The sensitivity of NH_3 flux modelling to χ_a was tested by scaling the input concentration by 9% to account for the error discussed in Puchalski et al. (2011). This resulted in an annual deposition increase of 47%, indicating the importance of accurate NH_3 measurements for flux modelling. Additionally, since the highest NH_3 concentrations occur during upslope events, the sources contributing to these events likely have a disproportionate effect on deposition. One limitation of this model is the exclusion of snow cover, which could significantly change NH_3 fluxes in the winter, when RMNP has frequent snow events. To probe the impact of snow cover, a sensitivity test was conducted setting χ_g equal to zero during the winter (December, January, and February), which increased annual deposition by 0.06 kg N ha^{-1} yr^{-1}. However, this analysis does not take into account how the surface differences may change NH_3 fluxes above snow. Future work should investigate NH_3 fluxes above snow cover to better simulate the exchange of NH_3 in regions with snow.

Due to the cost and technical challenges of making continual, high-time resolution NH_3 concentration measurements, there is growing interest in using integrated biweekly passive NH_3 measurements, such as those from the NADP AMoN network, for flux simulations. Here, we establish that a site-specific correction can be used to correct a bias introduced by using lower time resolution passive NH_3 measurements over the studied forest canopy in RMNP. We also establish that an average NH_3 diel pattern can be used to interpolate 30-minute NH_3 concentration and correct for the bias introduced by passive NH_3 measurements. In RMNP, a month of measurements proved sufficient to determine the diel pattern used for flux simulations. The correction factor and diel pattern, however, likely vary by location due to differences in ecosystem characteristics and factors influencing NH_3 concentrations. Due to the potential regional differences and changes associated with land surface type, additional sites should be studied to assess the impact of measurement time resolution on NH_3 flux simulations. To understand the seasonal variability in diel pattern and efficacy of diel pattern application for flux simulations, measurements should be conducted for a full year.

Local micrometeorological and soil measurements are also frequently unavailable, making the use of reanalysis data a desirable alternative for NH_3 flux simulations. In our location, the use of reanalysis data adds a bias that leads to overestimates of net NH_3 deposition. We found it was possible to apply a correction to address this bias, but this factor likely varies by location, in particular over different land surface types within a reanalysis grid cell. Future studies should explore the relationship between *in situ* measurements and reanalysis products above different land surface types, above varied topography, and in different regions. Understanding how to correct for the biases introduced through the use of reanalysis data would allow improved modelling of NH_3 bidirectional fluxes in regions lacking high time-resolution measurements

In this analysis, we simulated the bidirectional exchange of NH_3 above a forest ecosystem using the model proposed in Massad et al. (2010). However, there are other bidirectional exchange models (e.g., Zhang et al., 2010; Pleim et al., 2013) and their simulated fluxes may differ significantly from the model used here (Jongenelen et al., 2025). In the bidirectional exchange model used here, we observe that the selected inputs for NH_3 concentration and meteorological data may introduce biases into the simulated NH_3 fluxes. This may also be true for the other models when simulating NH_3 bidirectional exchange, a good topic for future research.

Chapter 3

Ammonia in Northeast Colorado is Increasing, Rising Most Quickly in Regions Close to Confined Animal Feeding Operations

The Colorado Front Range urban corridor and nearby agricultural operations are important source regions of atmospheric ammonia (NH_3). Upslope flows driven by mountain-plains and synoptic-scale circulations periodically transport these emissions into Rocky Mountain National Park, located 50 km west of the urban corridor, where wet and dry deposition of excess reactive nitrogen (N) contributes to ecosystem impacts. We use a combination of *in situ* passive sampler NH_3 measurements and NH_3 vertical column density retrievals from the Infrared Atmospheric Sounding Interferometer (IASI) to assess variability in NH_3 across three land use categories in the source region: agricultural, urban, and remote during the period 2013-2023. A strong seasonal cycle is present across the region with increased NH_3 during summer months. Spatial NH_3 enhancements are correlated with the number of permitted animal units in confined animal feeding operations (CAFOs) within a 12 km radius. Ground-level NH_3 concentrations are strongly correlated with monthly gridded IASI satellite column densities. Satellite retrievals reveal an increasing trend in NH_3 column amounts of ~3% per year in agricultural and ~2% per year in urban sub-regions. The absolute trend observed in NH_3 columns averaged over the agricultural sub-region is > 3 times larger than observed near and over Denver. Reductions in particle sulfate associated with declining sulfur dioxide (SO_2) emissions could account for a ~0.1% per year increase in gaseous NH_3. Increased wildfire smoke across the region during the study period appears unlikely to explain the majority of the observed NH_3 increase. The largest increases in NH_3 are closely aligned with the distribution of large CAFOs.

3.1 Introduction

Atmospheric gas-phase ammonia (NH_3) contributes significantly to fine particle formation and impacts ecosystem health through deposition processes (Baron et al., 2000; Driscoll et al., 2024; Hill et al., 2019; Li et al., 2016). Despite these important adverse effects, NH_3 emissions to the atmosphere are unregulated in the US. NH_3 increases the formation of submicron particles when combined with acidic species such as sulfuric and nitric acids produced through the atmospheric oxidation of sulfur dioxide (SO_2) and nitrogen oxides (NO_x). The atmospheric lifetime of NH_3 (g) is on the order of hours, due to rapid dry deposition and particle formation reactions, while the lifetime of particle ammonium (NH_4^+) is on the order of days, increasing the potential for long-range transport and deposition further from source regions (Aneja et al., 2001; Ianniello et al., 2011; Napari et al., 2002).

The main sources of atmospheric NH_3 are agriculture, industry, traffic, and biomass burning, with an estimated 80% of global emissions from anthropogenic sources (Butler et al., 2016; Sutton et al., 2013). In the US, the National Emissions Inventory attributed 82% of total NH_3 emissions in 2020 to emissions from livestock waste and fertilizer applications (US EPA, 2020). Additional anthropogenic NH_3 emissions include sewage treatment (Bouwman et al., 1997), 3-way catalysts in gasoline-powered engines (Jeong et al., 2024), selective catalytic reduction of NO_x in diesel engines (Li et al., 2021), and industrial sources (e.g., fertilizer production, coke production, and refrigeration) (Cheng et al., 2022; de Oliveira Carneiro et al., 2021; Kang et al., 2022). Wildfire smoke accounts for 98% of NEI NH_3 emissions from biomass burning (US EPA, 2020). The frequency of wildfire smoke in the atmosphere over the US has increased across the United States in recent years (Bray et al., 2018; Corwin et al., 2022). Within the atmosphere, NH_3 is mostly contained within the planetary boundary layer (PBL), although vertical profiles are variable (Guo et al., 2021; Sun et al., 2015). Large wildfire plumes can transport NH_3 into the free troposphere and increase the atmospheric lifetime against deposition (Lindaas et al., 2021). Although NEI NH_3 emissions have been fairly constant, measurements of NH_3 concentrations show increases over time in the US (Butler et al., 2016; Wang et al., 2023; Yu et al., 2018).

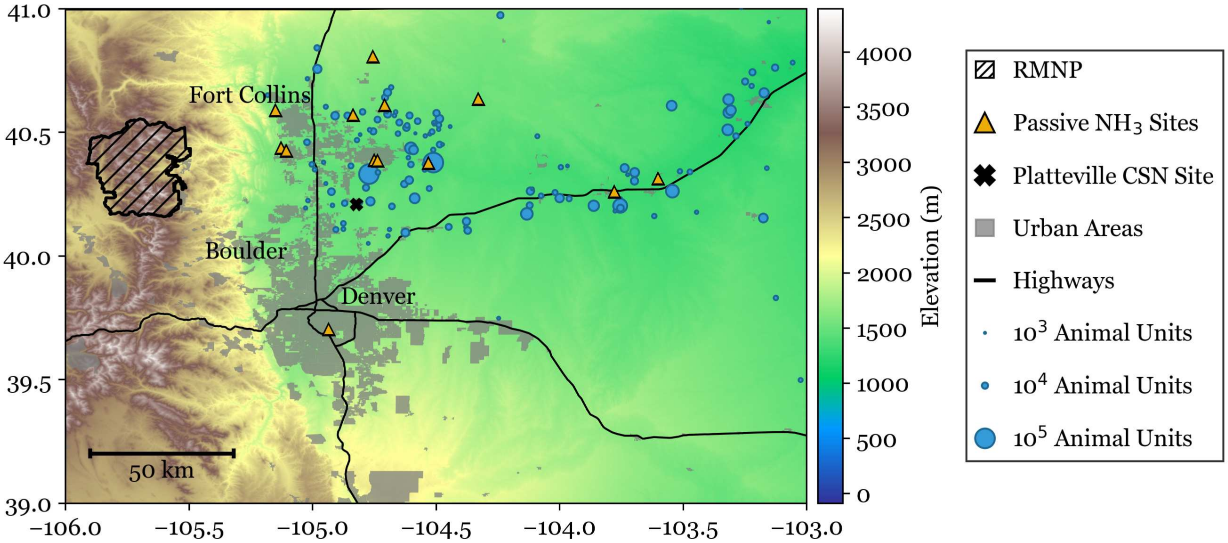

Figure 3.1: A map of the study region. Animal units are shown as the number of permitted animal capacity as of 2017, scaled by an animal unit factor relative to the species. Elevation data are from the US Geological Survey Global Multi-resolution Terrain Elevation Data 2010 (GMTED2010) at 7.5-arc-second spatial resolution (available at: https://earthexplorer.usgs.gov/).

NEI data for Colorado place the largest emissions by county in the northeast, a region with heavy agricultural activities and a large urban corridor (see Figure 3.1). NH_3 concentrations are highly variable across this continuum of remote, agricultural, and urban regions, with the highest observations closest to agricultural activities (Day et al., 2012; Li et al., 2017). Prior work in this region has focused on direct NH_3 from CAFOs (Juncosa Calahorrano et al., 2024), comparison with model results (Li et al., 2017), and spatiotemporal variability (Day et al., 2012).

Reactive nitrogen is a limiting nutrient in natural environments. Increased deposition of reactive nitrogen, above the natural background, can lead to decreased biodiversity, soil acidification, and lake eutrophication (Baron et al., 2000; Boot et al., 2016; Clark and Tilman, 2008; Galloway et al., 2008; Holtgrieve et al., 2011). Critical loads have been established to define the amount of reactive nitrogen deposition that ecosystems can withstand before experiencing deleterious effects. Using modeled deposition, Ellis et al. (2013) found that critical loads were exceeded in 24 of 45 US national parks. Primary emissions of SO_2 and NO_x, predominantly from power generation and transportation, in the United States, have been decreasing due to effective regulatory controls (Coughlin et al., 2023; LaCount et al., 2021). This has caused a regime shift from oxidized nitrogen (HNO_3 + NO_3^-) to reduced nitrogen (NH_3 + NH_4^+) dominated reactive nitrogen deposition (Driscoll et al., 2024; Li et al., 2016; Pan et al., 2024). This regime shift is observed in RMNP, where reduced nitrogen species dominate deposition in the park (Benedict et al., 2013a; Benedict et al., 2013b). Pan et al. (2021) identified 10 US National Parks within 100 km of an agricultural hotspot of NH_3 emissions and at elevated risk for nitrogen deposition, particularly from dry deposition of gas-phase NH_3. Rocky Mountain National Park is within 100 km of an agricultural hotspot and experiences consistent annual deposition above the critical load (Benedict et al., 2013a; Benedict et al., 2013b; Benedict et al., 2018; Juncosa Calahorrano et al., 2024).

There are limited routine measurements of NH_3 in the US, reflecting a lack of regulatory monitoring requirements. The Ammonia Monitoring Network (AMoN), operated by the National Atmospheric Deposition Program, is the only routine national monitoring network of NH_3 in the US (Puchalski et al., 2015). The network consists of approximately 100 sites with passive NH_3 samplers, mostly in rural locations. Passive NH_3 measurements, which rely on diffusion-driven collection on an acid-impregnated substrate, are advantageous because they are cost-effective and easy to install. However, due to the short atmospheric lifetime of gaseous NH_3 and the limited spatial coverage of the network, AMoN network observations may not capture strong spatial gradients in NH_3 source regions (Juncosa Calahorrano et al., 2024; Wang et al., 2023).

Atmospheric NH_3 is also measured at high spatial resolution from satellites. Ground-based passive NH_3 measurements typically have good agreement with satellite retrievals of NH_3 (Guo et al., 2021; Pinder et al., 2011; Sun et al., 2015; Wang et al., 2023). Satellite retrievals of NH_3 are available from the Tropospheric Emission Spectrometer (TES) (Beer et al., 2008), Infrared Atmospheric Sounding Interferometer (IASI) (Clarisse et al., 2009), Cross-track Infrared Sounder (CrIS) (Shephard and Cady-Pereira, 2015), Atmospheric Infrared Sounder (AIRS) (Warner et al., 2016), and Thermal and Near Infrared Sensor for Carbon Observations – Fourier Transform Spectrometer (TANSO-FTS) (Someya et al., 2020). Satellite retrievals provide spatial data that can be used to bridge gaps between surface monitoring stations (Wang et al., 2023). We utilize IASI satellite retrievals to examine spatial and temporal variability in NH_3 over NE Colorado because of the agreement with passive measurement sample collection period (2013-current on Metop-B), lack of biases when compared with ground concentrations, and availability of the corrected Level 3 post-processed data product (Clarisse et al., 2023; Guo et al., 2021; Wang et al., 2021).

In this work, we use surface observations and daytime IASI satellite retrievals to probe spatial and temporal trends in NH_3 across the important NH_3 source region in northeast Colorado. Spatial patterns in NH_3 are examined with respect to proximity to confined animal feedlot operations, the largest NH_3 source in the regional emissions inventory. Temporal trends analysis is conducted with both datasets to assess 1. changes in atmospheric NH_3 across the period of record, 2. whether observed trends differ between urban and agricultural source regions, and 3. whether observed trends are consistent with expectations from increasing wildfires or decreasing emissions of acid precursors.

3.2 Methods

To supplement the spatial resolution of the AMoN network, we deployed passive NH_3 samplers to collect integrated 2-week samples in northeast Colorado to monitor surface NH_3 concentration between 2010 and 2023. Figure 3.1 shows the measurement locations and proximity to agricultural and urban source regions. Our network has sites close to agricultural and urban activities and in remote regions away from major sources. Earlier subsets of this data were used to probe spatial variability across regions, temporal trends, and comparison with model results and satellite retrievals (Day et al., 2012; Li et al., 2017).

Low-cost passive NH_3 samplers from Radiello (https://radiello.com/) were deployed to measure 2-week, time-integrated NH_3 mixing ratios. The sample collection system includes a porous diffuse body, which transmits gaseous NH_3 but excludes the collection of particulate NH_4^+, and an interior absorbing cartridge coated with phosphoric acid for NH_3 collection. Samples are extracted in deionized water and analyzed using ion chromatography (Li et al., 2017). Samples were prepared in a laminar-flow hood free of NH_3 and then sealed for transport to the monitoring site locations (Day et al., 2012).

Sample collectors are covered to protect them from precipitation and installed at ~1 meter above ground level. Table 3.1 describes the general classification of each site, the summertime mean mixing ratio, and the period of collection. From 2010 to 2014, samples were collected from May to September at a weekly frequency. From 2015 to 2023, samples were collected from March to October at a biweekly frequency. Samples deployed at Fort Morgan, Burlington, and Denver were mailed to/from Fort Collins; other samples were deployed and retrieved directly by project staff.

Table 3.1: Sampling site locations and years that passive NH_3 data were collected. Mean summer NH_3 mixing ratios are calculated as the means across all years of data for June, July, and August.

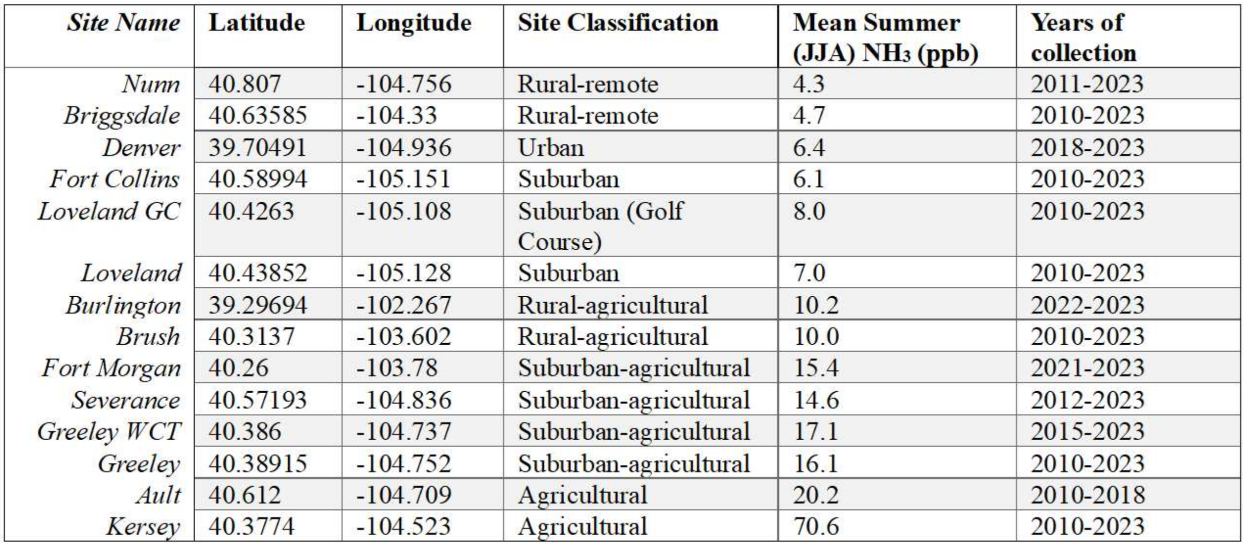

Site Name	Latitude	Longitude	Site Classification	Mean Summer (JJA) NH_3 (ppb)	Years of collection
Nunn	40.807	-104.756	Rural-remote	4.3	2011-2023
Briggsdale	40.63585	-104.33	Rural-remote	4.7	2010-2023
Denver	39.70491	-104.936	Urban	6.4	2018-2023
Fort Collins	40.58994	-105.151	Suburban	6.1	2010-2023
Loveland GC	40.4263	-105.108	Suburban (Golf Course)	8.0	2010-2023
Loveland	40.43852	-105.128	Suburban	7.0	2010-2023
Burlington	39.29694	-102.267	Rural-agricultural	10.2	2022-2023
Brush	40.3137	-103.602	Rural-agricultural	10.0	2010-2023
Fort Morgan	40.26	-103.78	Suburban-agricultural	15.4	2021-2023
Severance	40.57193	-104.836	Suburban-agricultural	14.6	2012-2023
Greeley WCT	40.386	-104.737	Suburban-agricultural	17.1	2015-2023
Greeley	40.38915	-104.752	Suburban-agricultural	16.1	2010-2023
Ault	40.612	-104.709	Agricultural	20.2	2010-2018
Kersey	40.3774	-104.523	Agricultural	70.6	2010-2023

3.2.1 Satellite retrievals

Total column NH_3 concentrations were obtained from the Infrared-Atmospheric Sounding Interferometer (IASI). IASI orbits at nadir on the Meteorological Operating (MetOp) satellites, operated by the European Space Agency. IASI uses a Fourier Transform Spectrometer measuring in the infrared band between 3.4 and 15.5 microns (Clarisse et al., 2009; Van Damme et al., 2015). IASI provides twice daily retrievals at 09:30 and 21:30 local time, with a circular pixel of 12 km diameter at nadir. The detection limit of IASI retrievals depends strongly on thermal contrast

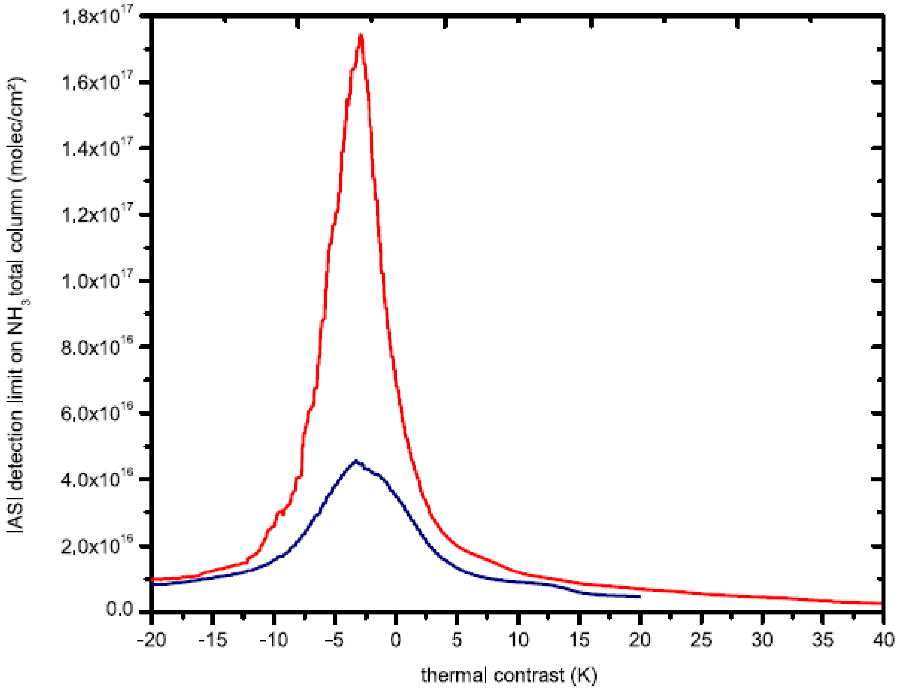

Figure 3.2: Figure 5 from Van Damme et al. (2014), showing the relationship between IASI detection limit and thermal contrast for retrievals over land (red) and sea (blue).

and the vertical profile of NH_3, with higher thermal contrast and NH_3 concentrations located in the peak sensitivity window lowering the detection limit (Van Damme et al., 2014). Figure 3.2 illustrates the relationship between thermal contrast, or the relative difference in surface and air temperatures, and IASI total column NH_3 detection limit. Thermal contrast values are typically negative overnight, when the surface temperature exceeds the near-surface air temperature. Only daytime retrievals are used in this work because the higher thermal contrast reduces the detection limit. Van Damme et al. (2014) found that favorable TC (TC > 10 K) had a detection limit of ~10^{16} molec. cm^{-2}.

We obtained data from the MetOp-B satellite due to its temporal overlap with ground-based measurements (last accessed: 08/01/2024). Data are available for download at (https://iasi.aeris-data.fr/catalog). Data spans from March 8, 2013, to March 31, 2023. For this application, we use the Level 3, Version 4 Artificial Neural Network with Reanalysis (ANNI-NH3-V4R) product, which offers monthly data at 0.125 by 0.125-degree grid cell resolution. ANNI Version 4 introduced a total column averaging kernel and improved the consistency of measurements (Clarisse et al., 2023). The median global uncertainty of version 4 of the Level 3 for morning IASI overpasses is 4×10^{15} molec. cm^{-2}, with a 20 to 80 quantile range of 2.5 to 6.6×10^{15} molec. cm^{-2} (Clarisse et al., 2023). The reanalysis version relies on ERA5 ECMWF meteorological input data, surface temperature, and cloud retrievals (Hersbach et al., 2020; Van Damme et al., 2018). Only the morning overpasses (09:30 local time) were analyzed due to their higher daytime thermal contrast (Clarisse et al., 2010). IASI retrievals are well correlated with ground-based measurements, showing good agreement for NH_3 spatial patterns (Guo et al., 2021; Wang et al., 2023).

3.2.2 Aerosol measurements

Speciated aerosol measurements were taken from the US EPA Chemical Speciation Network (CSN, data available at: https://www.epa.gov/amtic/chemical-speciation-network-csn). The CSN was established in 2000 to monitor fine particulate matter (aerodynamic diameters < 2.5 microns) in the US. CSN sites collect 24-hour aerosol samples on Teflon and quartz filters. Additional information about the network can be found in Solomon et al. (2014). Data were downloaded for the Platteville, CO, USA site (40.209387°N, -104.824050°W) in our study region. Data collection at Platteville began in 2002 and is ongoing (last accessed: 05/02/2024).

3.2.3 Monthly reanalysis data

The European Centre for Medium-Range Weather Forecasts (ECMWF) Reanalysis version 5 (ERA5) monthly reanalysis dataset (Hersbach et al., 2020) at 0.25-degree resolution was accessed for Colorado from 2013 to 2023 (last accessed: 07/18/2024). Two-meter temperature and boundary layer height (BLH) datasets were used to analyze trends in meteorology.

3.2.4 Modeled smoke plumes

We use smoke plume from the Hazard Mapping System (HMS) (data available at: https://www.ospo.noaa.gov/Products/land/hms.html) operated by the National Oceanic and Atmospheric Administration's (NOAA) National Environmental Satellite, Data, and Information Service

(NESDIS). To generate the HMS dataset, analysts use a suite of satellite data products to manually outline the extent of detected smoke plumes. HMS smoke plumes are given a qualitative density flag (light, medium, or heavy). HMS smoke plumes have been used to estimate smoke exposure, assess smoke trends, and determine radiative impacts of smoke plumes (Corwin et al., 2025; Corwin et al., 2022; O'Dell et al., 2021; Zhou et al., 2021). We use HMS smoke plumes between 15:30 UTC (8:30 MST) and 17:30 UTC (10:30 MST) to determine which days in the study period were impacted by smoke. If a smoke plume polygon of any density overlaps the mid-point of an IASI grid cell, we classify that grid cell for that day as smoke-impacted. Days affected by smoke in the agricultural and urban source regions are determined as any day there was an HMS smoke plume overhead in any section of the source region.

3.2.5 Trend analysis

Trends are calculated using a Theil-Sen estimator (Sen, 1968). The Theil-Sen estimator is non-parametric and less sensitive to outliers than optimized least squares linear regression. Unless otherwise noted, statistical significance is determined using a Mann-Kendall test at the 95 percent confidence level (Hussain et al., 2019). Before trend analysis, the seasonal cycle was removed from all data by subtracting the monthly mean across the data record. NH_3 trends are assessed for agricultural and urban source regions to compare changes associated with each region (Figure 3.3). Agricultural and urban source regions are qualitatively defined using the spatial distribution of urban areas and CAFO locations. These regions are similar to those defined by Pan et al. (2021) to assess the transport of NH_3 to RMNP from urban and agricultural source regions.

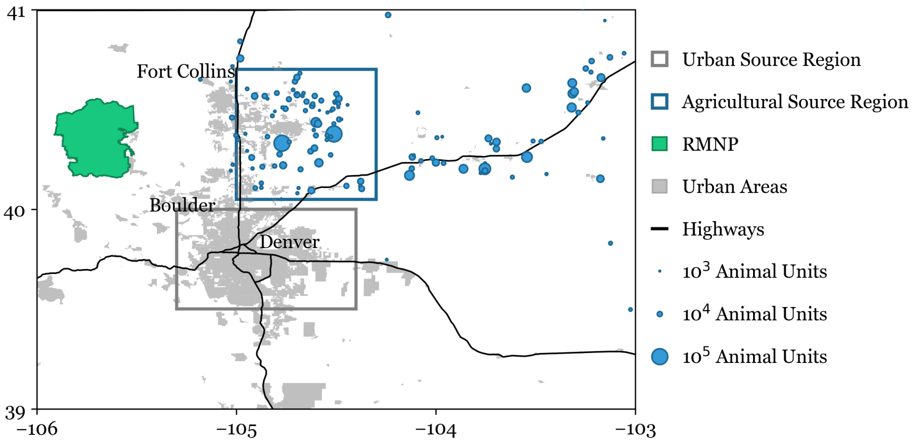

Figure 3.3: A map of the study regions with key source regions outlined.

3.3 Results and discussion

3.3.1 Variability in atmospheric NH_3

NH_3 has high spatial variability in northeast Colorado, with measured 2-week *in situ* mixing ratios ranging from 1 to 159 ppb. Mean mixing ratios from June, July, and August (JJA) are reported annually in Figure 3.4. Observed summertime mean mixing ratios range from 1.8 to 86.1 ppb. This range is larger than previously reported by Li et al. (2017) for a 2010-2015 subset of the data, with the maximum value occurring in 2020. Since these mixing ratios are from two-week integrated sampling periods, peak daily values are likely much larger due to the strong diel pattern of NH_3 emissions.

Measurement sites in Figure 3.4 are ordered based on the site classification listed in Table 3.1. From left to right, the figure goes from rural-remote to urban to agricultural. The largest mixing ratios are observed at agricultural sites. Mixing ratios observed at Kersey, our most agricultural source-influenced site, are typically more than three times larger than the other sites classified as agricultural. The site in Kersey is located within 0.5 km of one of the largest feedlot operations in Colorado, with a capacity of approximately 100,000 head of cattle. Statistically significant temporal trends for each site are shown in Figure 3.4 and will be discussed further in this work.

Spatial variability in NH_3 concentrations is also observed in the satellite data; annual summertime mean NH_3 column concentrations span an order of magnitude, ranging from 1.8×10^{15} to

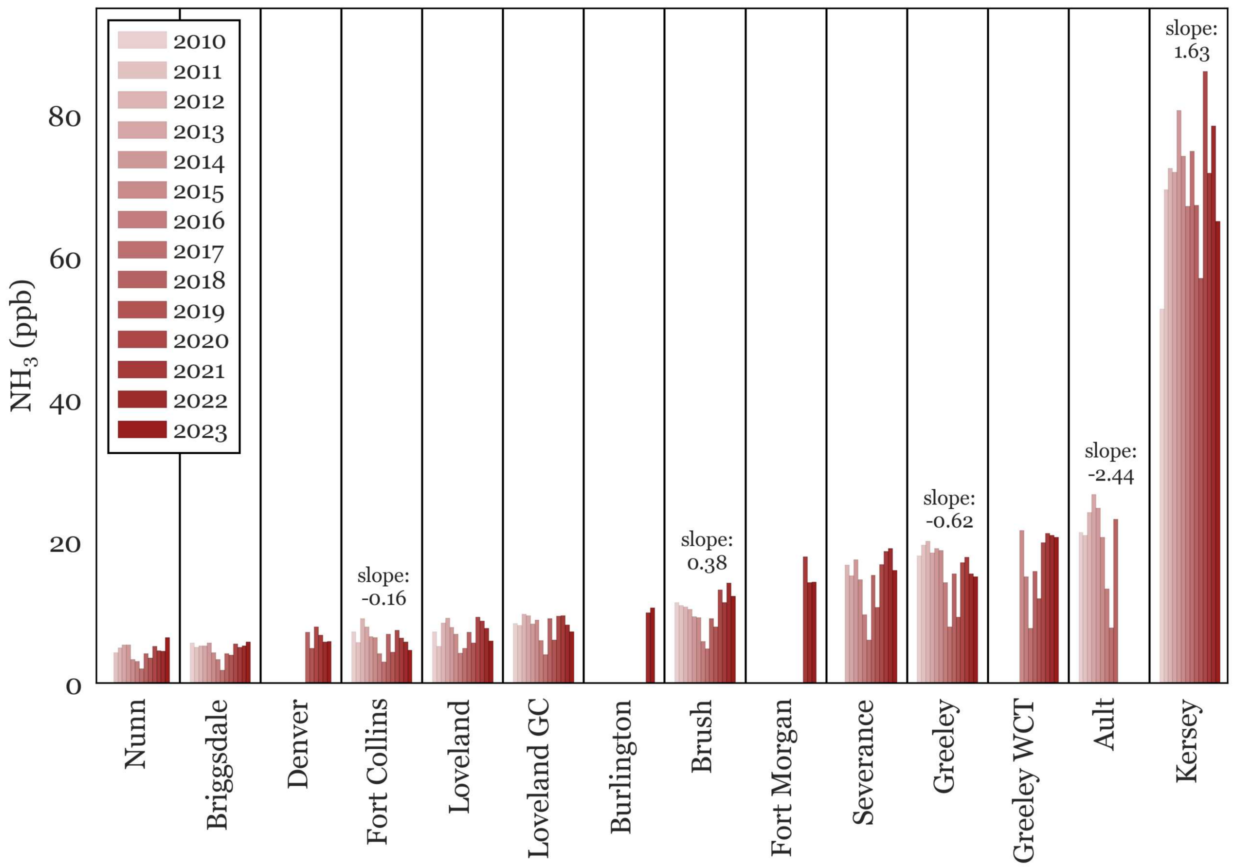

Figure 3.4: Annual summertime (JJA) mean NH_3 mixing ratios are shown for passive NH_3 observations. Trend analysis was conducted for each site. The slope of statistically significant trends is printed above the data for each site, with units of ppb per year. 95 CL trend slopes do not overlap zero for statistically significant trends.

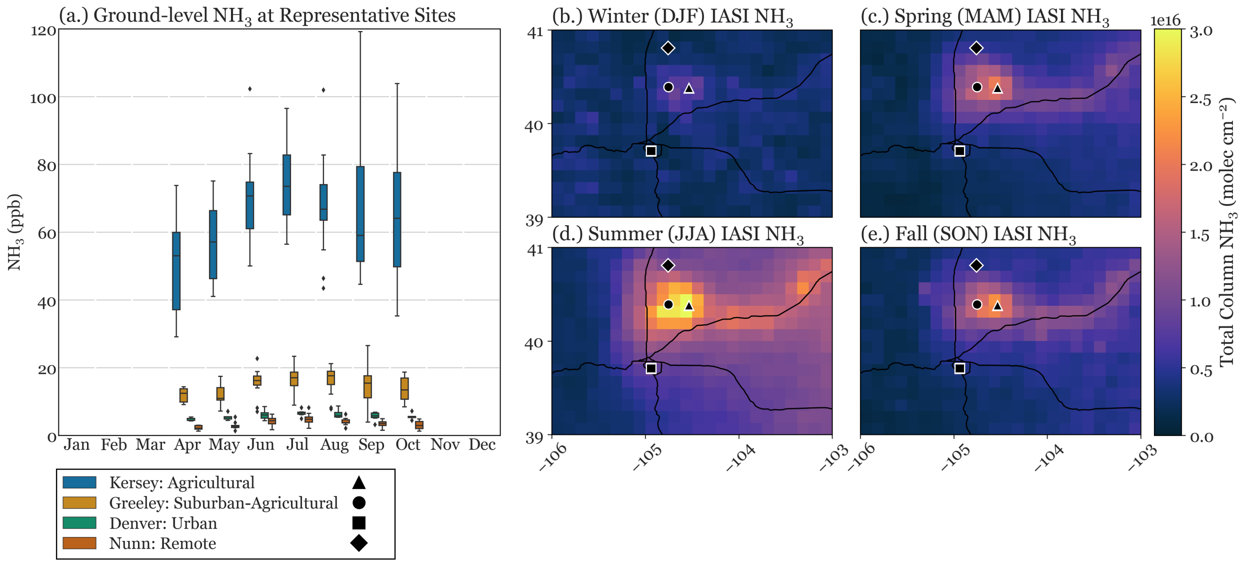

Figure 3.5: (a.) A boxplot of monthly mean *in situ* NH_3 mixing ratios is shown for four representative sites, spanning remote, urban, and agricultural impacts. For each box, the median is a horizontal line, box limits show the 25^{th} to 75^{th} percentile or interquartile range (IQR), whiskers are determined at 1.5 times the IQR, and outliers are diamonds. (b.) – (e.) Seasonal plots of IASI total column NH_3 are shown, with the location of each representative site from subplot (a.).

3.1×10^{16} molec. cm^{-2}. Figure 3.5 displays the spatial variability and seasonal cycle observed in the satellite and *in situ* data sets. The seasonal cycle of 4 example sites spanning agriculture, urban, and rural-remote environments is shown in Figure 3.5a. Each site shown has a seasonal pattern with the highest mean and median values occurring during June, July, and August. The largest values across seasons are observed in the agricultural sites Kersey and Greeley. Locations of the four representative sites are overlaid in Figure 3.5b through e on the seasonally averaged observations from the IASI satellite retrievals. IASI total column NH_3 concentrations also peak in the summer and broadly follow the spatial pattern of CAFO locations shown in Figure 3.1. The two agricultural *in situ* sites, Kersey and Greeley, are located within the peak NH_3 region observed from the satellite.

Passive NH_3 mean mixing ratios in this region differ by more than an order of magnitude, while IASI total column concentrations differ by less than a factor of 3, indicating that greater spatial variability is detected in the surface NH_3 observations. The spatial distributions of mean NH_3 integrated column concentration from IASI and mixing ratios from all *in situ* passive NH_3

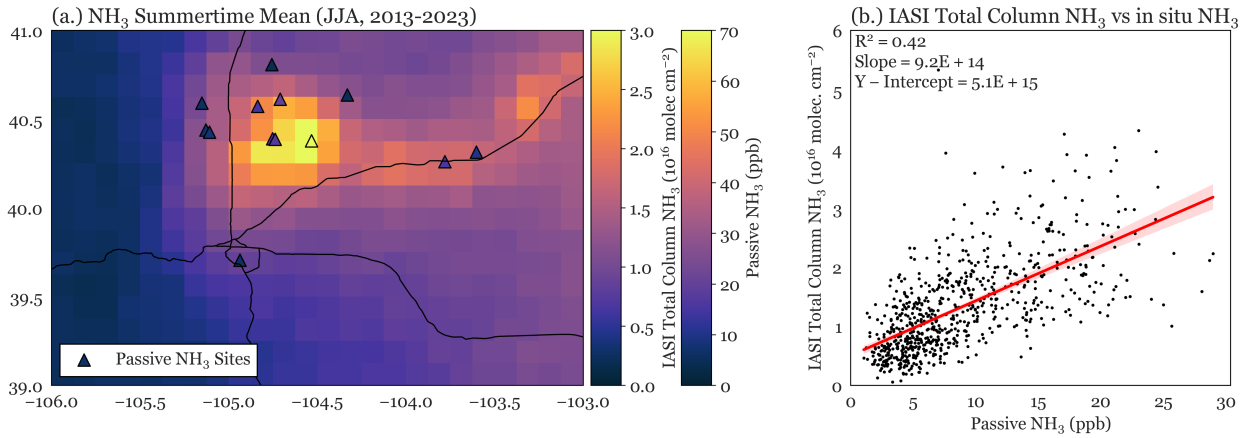

Figure 3.6: (a.) The spatial distributions of IASI satellite NH_3 columns and *in situ* passive surface NH_3 concentrations are shown for 2013 to 2023. Both datasets depict JJA mean values. (b.) IASI total column NH_3 concentrations for the corresponding grid cell are plotted against monthly mean NH_3 concentrations from passive monitoring network sites. Data are only shown for JJA. Kersey data are omitted from the comparison due to large influence of nearby feedlot emissions.

observations from 2013 to 2023 are shown in Figure 3.6a. The largest values from both datasets are in areas of heavy agricultural development. However, the spatial gradient observed in the *in situ* measurements is sharper than the IASI satellite retrievals. The peak NH_3 value for the 2013 to 2023 JJA mean (Figure 3.6a) in the satellite data and *in situ* data occurs in Kersey, at 3.1×10^{16} molec. cm^{-2} and 86 ppb, respectively. Within the agricultural region defined in Figure 3.3, summertime mean IASI total column NH_3 concentrations across 2013 to 2023 range from 1.2×10^{16} to 3.1×10^{16} molec. cm^{-2}. In the same region and period, mean *in situ* NH_3 observations range from 1.8 ppb to 86 ppb. This reflects the proximity of the Kersey monitoring site to one of the largest CAFOs in Colorado. Aircraft NH_3 from this region also found a steep gradient in NH_3 concentrations around CAFO, with an estimated NH_3 lifetime against deposition and transformation of only 87–120 min (Juncosa Calahorrano et al., 2023). Such sharp local concentration gradients are not evident in the IASI column concentration data due to sub-grid spatial averaging.

Figure 3.6b directly compares monthly mean passive NH_3 mixing ratios with IASI total column NH_3 concentrations in the corresponding grid cell. Data are omitted from Kersey due to its proximity to a very large CAFO and the expected steep gradient in NH_3 concentrations at the sub-grid level. The IASI grid cells are 0.125 by 0.125 degrees, or approximately 12 km, and therefore unlikely to capture maximum values very close to large emission sources due to dispersion and deposition of NH_3 moving away from the source. The IASI total column NH_3 and monthly mean passive NH_3 mixing ratios are positively correlated ($R^2 = 0.42$) despite expected variability in the relationship between surface and column concentrations due to differences in source locations across grid cells and variable meteorology, including wind direction and boundary layer height.

Elevated NH_3 concentrations have previously been observed to be spatially correlated with agricultural activity, especially the presence of CAFOs, in Colorado (Juncosa Calahorrano et al., 2023; Juncosa Calahorrano et al., 2024; Wang et al., 2021). The characteristic length scale of NH_3 emission hotspots was determined as 12 km by Wang et al. (2021) over the contiguous US. Figure 3.7 shows the correlation between permitted animal units in CAFOs in northeast Colorado and elevated NH_3. Animal units are counted for CAFO locations within 12 km of each ground-based site (Figure 3.7a) or within each IASI grid cell (Figure 3.7b). For both datasets, elevated NH_3 is well correlated with total animal units, explaining 78% and 50% of the variability for *in situ* and satellite NH_3, respectively. Kersey data are again omitted in Figure 3.7a. Additional factors expected to influence measured NH_3 include differences between permitted and actual livestock head at CAFOs in the region, transport of NH_3 from more distant CAFOs, emissions from other source types, and variations in meteorological conditions that influence NH_3 dispersion and deposition.

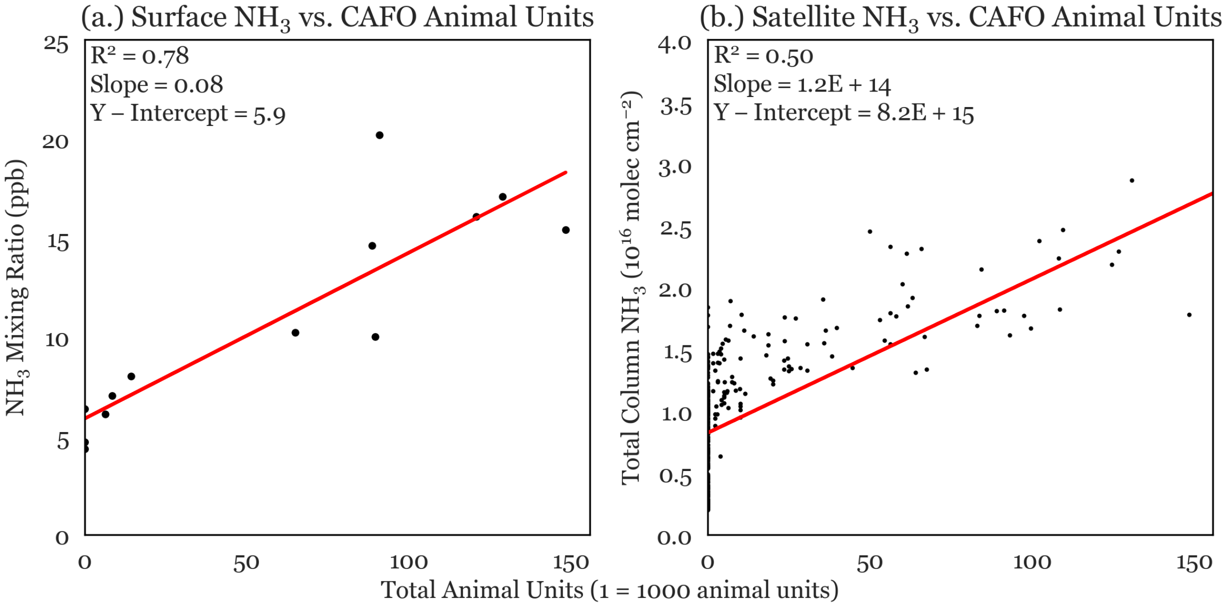

Figure 3.7: Animal units for both plots are shown as the number of permitted animals as of 2017, scaled by an animal unit factor relative to the species. Optimized least squares regression is shown in red. (a.) NH_3 mixing ratio from passive sites is plotted against total animal units within 12 km of the site. Kersey data are omitted as in Figure 3.6 and discussed in the text. (b.) IASI total column NH_3 concentration is plotted against total animal units within each grid cell. Grid cells are 0.125-degree resolution, or approximately 12 km.

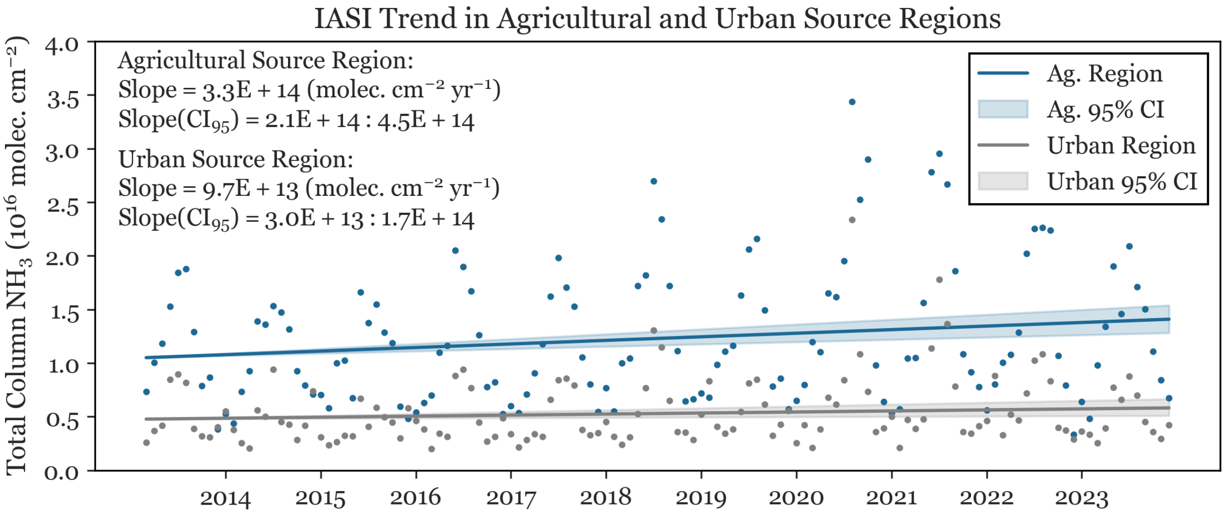

Figure 3.8: Satellite NH_3 data were assessed for trends using the urban and agricultural source regions defined in Figure 3.3. Trend analysis was conducted using the Theil-Sen estimator and Mann-Kendall test for statistical significance at the 95^{th} percentile. The seasonal cycle was removed from each spatial monthly mean before trend analysis. The 95^{th} percentile confidence interval for the Theil-Sen slope is shaded around each fit.

3.3.2 NH_3 trends in northeast Colorado

Temporal trends were assessed at each ground site for the entire data record using the Theil-Sen estimator. The slopes of the trends at sites with statistically significant trends at the 95^{th} percentile are shown in Figure 3.8. Five of the 14 passive NH_3 monitoring locations had a significant trend, with the largest changes observed in Ault (decreasing) and Kersey (increasing). The trends observed in the passive NH_3 monitoring locations included increasing and decreasing trends. The largest change is a decreasing trend of 2.44 ppb NH_3 yr^{-1} (12% yr^{-1}) observed at Ault; however, the data record from Ault ends in 2018 and may not capture recent changes in NH_3. The second largest change is an increasing trend of 1.63 ppb NH_3 yr^{-1} (2.3% yr^{-1}) observed at Kersey.

A significant increasing trend in total column NH_3 concentration is observed in the agricultural and urban source regions (Figure 3.8), at rates of 2.6% yr^{-1} in the agricultural region and 1.7% yr^{-1} in the urban region. The absolute slope in the agricultural source region is three times larger than the slope in the urban source region, and the 95^{th} percentile confidence intervals do not overlap.

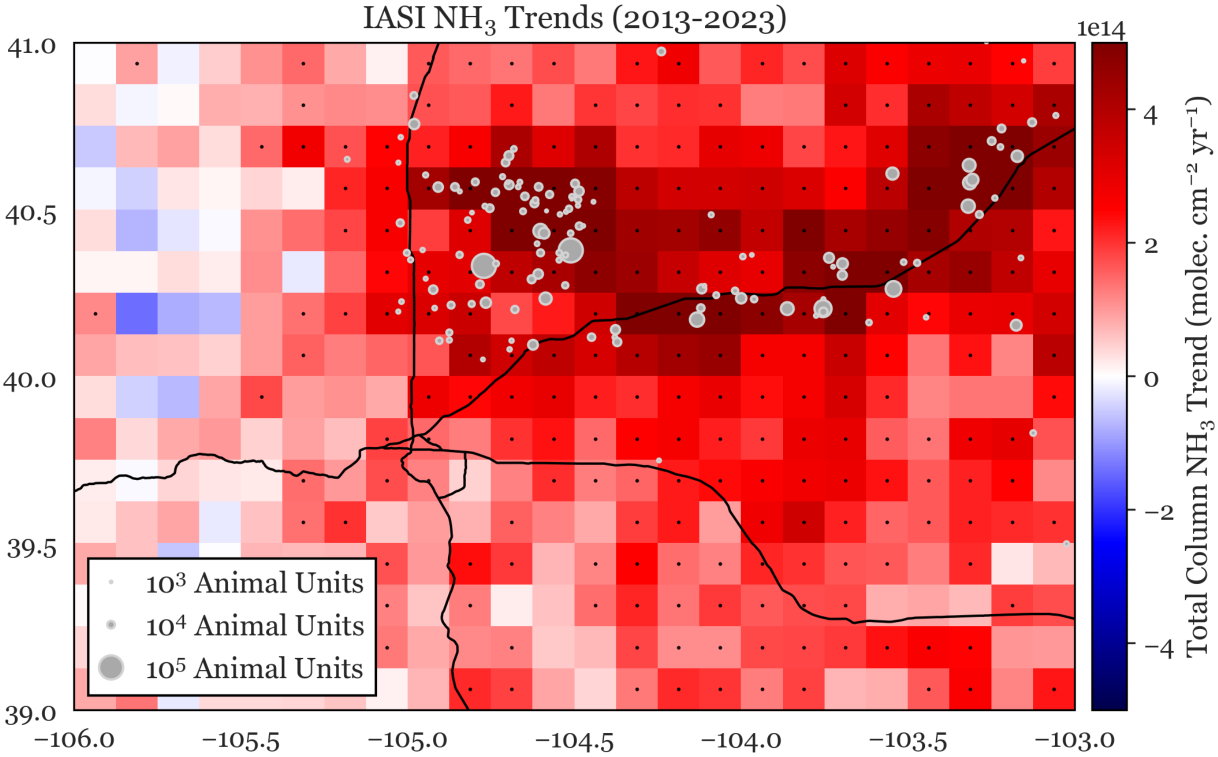

Figure 3.9: Trend analysis of total column NH_3 concentration in each IASI grid cell was conducted using the Theil-Sen estimator and Mann-Kendall test for statistical significance at the 95th percentile. The seasonal cycle was removed from each spatial mean before trend analysis. Stippling is used to indicate statistical significance. Positive (negative) values show an increasing (decreasing) trend in NH_3. Animal units are shown as the number of permitted animal capacity as of 2017, scaled by an animal unit factor relative to the species.

3.3.3 Potential causes for observed NH_3 trends

Increased emissions from CAFOs

Trend analysis was further conducted on a grid cell-by-grid cell basis to investigate the spatial distribution of increasing NH_3 in greater detail. Figure 3.9 shows the annual total column NH_3 trends from the IASI satellite retrievals, with statistical significance at the 95th percentile indicated by stippling. In the study region, there are no significant decreasing trends in NH_3. The largest increasing trends are observed to follow the spatial pattern of CAFO locations. Increasing trends are also correlated with permitted animal units within the associated grid cell ($R^2 = 0.3$).

Impacts of reducing SO_2 and NO_x emissions

One possible contributor to increasing gaseous NH_3 is a reduction in formation of fine particle ammonium sulfate and ammonium nitrate, through reduction in SO_2 and NO_x emissions (Li et al., 2016; Liu et al., 2018; Pan et al., 2024). Particle measurements of SO_4^{2-}, NO_3^-, and NH_4^+ were analyzed from the Chemical Speciation Network site in Platteville, CO (40.20939°N, -104.82405°W), located in the center of our study region (see Figure 3.1). SO_4^{2-} and NH_4^+ have statistically significant decreasing trends, while NO_3^- does not. We use the decreasing trend in SO_4^{2-} concentration to estimate the associated increase in free NH_3 by assuming that all SO_4^{2-} would be present as fully neutralized ammonium sulfate ($(NH_4)_2SO_4$). This is a reasonable assumption given the excess gas-phase NH_3 observed in our study region. Sulfate has decreased in Platteville by 3.1×10^{-10} moles m^{-3} yr^{-1} corresponding to an increase in gaseous NH_3 of 6.2 moles m^{-3} yr^{-1} or 0.015 ppb yr^{-1}. This represents an increase of approximately 0.1% per year relative to the mean summertime surface NH_3 mixing ratio from Greeley, the nearest passive network site, of 16.1 ppb. This result indicates that an increase in gaseous NH_3 resulting from SO_2 emission reductions is not a major contributor to the increasing NH_3 in the satellite observations.

Impacts of wildfire smoke

An increase in wildfire burn area in western North America could be an important contributor to increasing NH_3 (Bray et al., 2018; Corwin et al., 2022), particularly in the satellite record, which measures NH_3 throughout the lower atmosphere and not just at the surface. One example of the importance of wildfire emission of NH_3 is shown in Figure 3.10. During August 2020, substantial increases in NH_3 column concentrations are observed due to wildfire smoke from the Pine Gulch and Cameron Peak fires (Figure 3.10b) relative to levels averaged across all August measurement periods (Figure 3.10a). The Cameron Peak fire, the largest wildfire in Colorado history, was burning in the northwest corner of our study region. While clear increases in column NH_3 concentrations were detected over NE Colorado, no significant increase was observed in surface concentrations measured in the passive network, consistent with the lofting of the smoke plume as it traveled eastward.

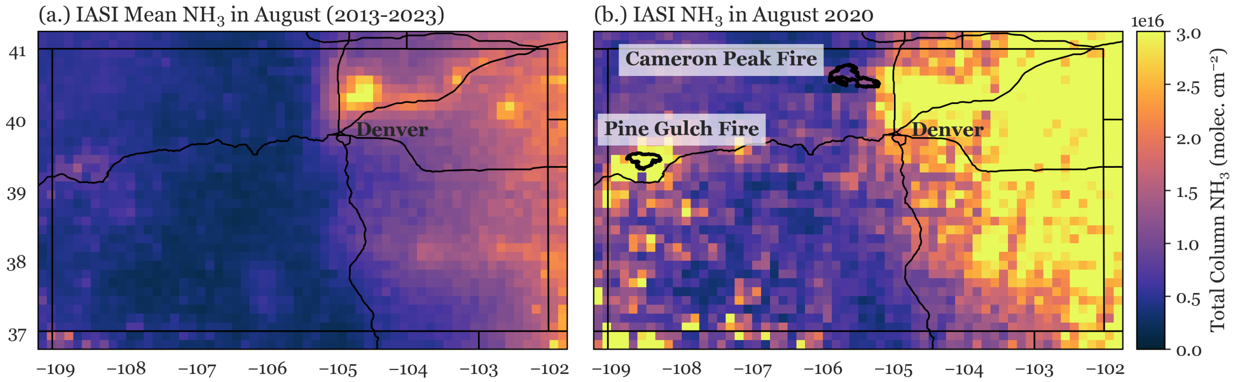

Figure 3.10: (a.) IASI 2013-2020 August mean total column NH_3 concentration for Colorado. (b.) IASI average total column NH_3 concentration for August 2020. The wildfire boundary extent of the Cameron Peak and Pine Gulch wildfires were obtained from the National Interagency Fire Center.

To consider the potential impact of increasing wildfire smoke on NH_3 concentrations in northeast Colorado, HMS smoke plumes are used to determine the frequency of wildfire smoke. In both source regions, the frequency of smoke-affected days increased by approximately 3 days per year across the study period. Given the very similar increase in wildfire smoke over the urban and agricultural zones, we conclude that the rate of NH_3 increase coming from smoke is likely no larger than the rate of increase measured over the urban region (approximately one-third the rate over the agricultural region) and could be less. Future research should quantify the impact of increasing wildfire smoke on NH_3 levels across the western US.

Impacts of changing meteorology

It is noteworthy that while we detect significant trends in satellite NH_3 column concentrations, we do not see consistent significant trends in surface concentration measurements. This difference might reflect the greater averaging (larger surface footprint and greater integrated vertical depth) in the satellite data vs. the point measurements from the surface network. Other factors, however, might also contribute to this difference. First, NH_3 from wildfire smoke is increasing over the region, sometimes in layers aloft that are captured as part of the column measured by the satellite but not observed at the surface. Second, NH_3 emissions from agricultural activities and other surface sources get mixed throughout the boundary layer. If the boundary layer has increased in

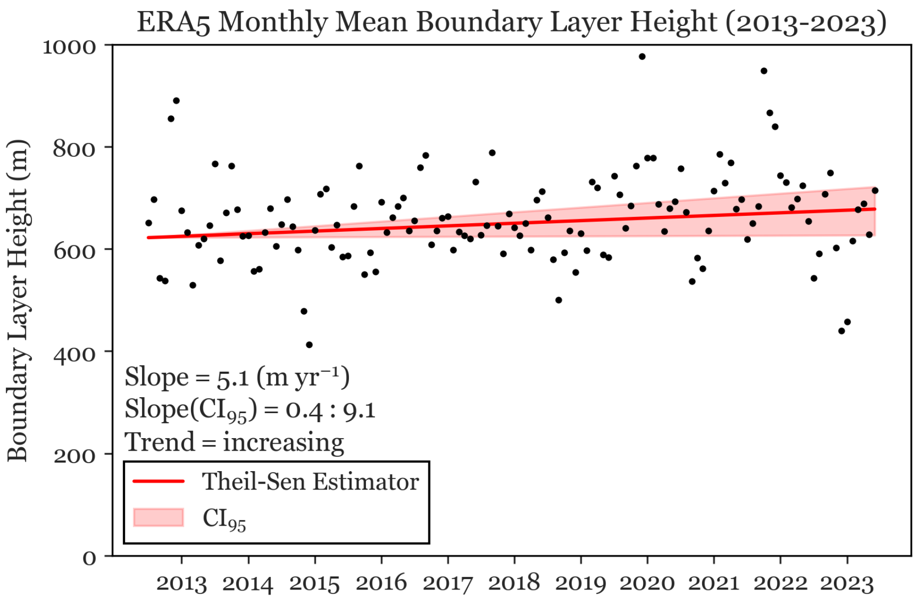

Figure 3.11: Boundary layer height from ERA5 is shown for 2013-2023 with the seasonal cycle removed. Trend analysis was conducted using the Theil-Sen estimator and Mann-Kendall test for statistical significance at the 95^{th} percentile.

depth over time, due for example to a warming climate, increased surface NH_3 emissions could yield increasing NH_3 column concentrations while surface concentrations may be increasing more slowly or not at all.

Sun et al. (2015) found that NH_3 in the atmosphere is relatively well mixed within the planetary boundary layer. Mean monthly BLH from ERA5 reanalysis was examined to assess changes over the study period (see Figure 3.11). An increasing BLH trend of 5.1 m per year is observed above the northeast Colorado plains from 2013-2023. For this analysis, only data east of Fort Collins (longitude bound of -105°W) is considered due to challenges with ERA5 data quality over regions of complex topography. This increasing boundary layer height and associated vertical dilution of NH_3 surface emissions could contribute to the difference between NH_3 trends in the satellite and surface data records.

Another significant meteorological trend in the region is in surface temperature. Analysis of regional temperature records reveals a significant, increasing trend in summertime temperature of 0.09 degrees per year. Given the sensitivity of NH_3 volatilization (e.g., from fertilized fields, feedlots, and natural soils) to temperature, it is likely that at least some of the increase in NH_3 column concentrations detected in the IASI satellite records reflects temperature-driven surface emissions.

3.4 Conclusion

We used a combination of *in situ* passive sampler NH_3 measurements and NH_3 vertical column density retrievals from IASI to assess variability and trends in NH_3 across three land use categories in the source region: agricultural, urban, and remote during the period 2013-2023. Enhancements in IASI NH_3 total column concentrations have the same spatial distribution as observed in the surface NH_3 observations. NH_3 concentrations measured in the surface monitoring network and IASI NH_3 column concentration retrievals were both well correlated with the presence and size of nearby CAFOs. The permitted animal capacity of CAFOs within 12 km of surface monitoring sites explained 78% of the variability in observed NH_3 mixing ratio. Similarly, permitted animal capacity within each IASI retrieval cell (length and width approximately 12 km) explained 50% of the variability in total column NH_3 concentrations.

Surface-level NH_3 and total column NH_3 were well correlated with each other, supporting the use of satellite NH_3 retrievals to examine NH_3 temporal and spatial variability in this region. IASI satellite retrievals exhibited an increasing NH_3 column concentration trend in both agricultural (2.6% yr^{-1}) and urban (1.7% yr^{-1}) source regions. The absolute magnitude of the trend in the agricultural region was 3 times larger than in the urban region. A more detailed analysis of NH_3 concentration increases at higher spatial resolution revealed strong similarity to the spatial distribution of large CAFOs. Decreases in ammonium sulfate and increases in wildfire smoke likely also contribute to the increase in NH_3, but they are unlikely to be of sufficient magnitude to produce the observed changes in NH_3.

A changing climate in NE Colorado has resulted in both increased temperatures and a deepening surface boundary layer. Increased surface temperatures are likely contributing to increased NH_3 evaporation from agricultural sources, including feedlots. If so, CAFO emissions of NH_3 may at least partly be increasing independently of agricultural practices or livestock numbers. Meanwhile, observed increases in boundary layer depth are likely diluting NH_3 surface concentrations via increased vertical mixing. This process can decouple trends in satellite-detected NH_3 column concentrations from surface concentration trends while also enhancing the atmospheric lifetime and long-range transport of atmospheric NH_3 by slowing surface deposition.

Chapter 4

Contributions of Wildfire Smoke and Agricultural Emissions to Changing Ammonia across the Western US

Ammonia (NH_3) emissions contribute to atmospheric particle formation and reactive nitrogen (N_r) deposition. The formation of particulate matter can be harmful to human health and increase the atmospheric lifetime of NH_3, allowing for increased deposition in remote ecosystems. Excess N_r deposition can have harmful ecosystem effects, including in the high-alpine Rocky Mountains, where ecosystems developed under nutrient-deprived conditions. A majority of atmospheric NH_3 in the US is emitted from agricultural activities, with important contributions also from wildfires. In this study, we focus on NH_3 in the US Rocky Mountain region. This region is home to: 1. ecosystems sensitive to reactive nitrogen deposition, 2. heavy agricultural development, and 3. frequent and increasing wildfires. Cross-track Infrared Sounder (CrIS) data, oversampled to high spatial resolution (2 km), are used for the warm season (March-October), when peak agricultural emissions and wildfire frequency occur, to assess contributions to changing NH_3 from these key sources over the period 2013 to 2023. We find that the largest total column NH_3 increases are associated with agricultural regions, with average trends ranging from 1.5 to 4.8% increase per year. In the Snake River Valley in Idaho, removing smoke impacts did not affect the annual total column NH_3 trend of 1.5% per year in the agricultural region. In northeast Colorado, removing thick smoke plumes from the dataset reduced the NH_3 trend from 2.7 to 2.5% per year. NH_3 increases in remote regions farther from major agricultural sources were heavily impacted by wildfire smoke, likely due to wildfires often occurring in remote regions and increased NH_3 atmospheric lifetime when lofted in smoke plumes. We assessed the spatial extent of agricultural NH_3 emission hotspots, using a contouring algorithm assessed at the full dataset 95^{th} percentile, and found that the area of agricultural hotspots is increasing by 7% per year across the Intermountain West. This spatial increase was enhanced by wildfire smoke, dropping to 6% per year when the influence of thick smoke plumes was removed.

4.1 Introduction

Ammonia (NH_3) is the primary alkaline gas in the atmosphere, playing a key role in the formation of submicron particles and the global nitrogen cycle. Primary emissions of NH_3 come from agricultural activities, industry, automobiles, and biomass burning (Behera et al., 2013; Walker et al., 2019a). Submicron particles are formed when atmospheric NH_3 is mixed with acidic species, primarily sulfuric and nitric acids, to form particle ammonium (NH_4^+) (Behera et al., 2013). In the US, an estimated 30% of fine particulate matter ($PM_{2.5}$) pollution is attributed to NH_3 emissions (Wyer et al., 2022). Across the globe, agricultural sources dominate $PM_{2.5}$ when compared with natural and other anthropogenic sources (Bauer et al., 2016). In addition to its negative health impacts, $PM_{2.5}$ formation increases the atmospheric lifetime of NH_x (NH_3 + NH_4^+), increasing transport distance and the likelihood of deposition to remote ecosystems (Aneja et al., 2001; Ianniello et al., 2011; Napari et al., 2002).

The deposition of excess N_r negatively impacts ecosystem health through eutrophication, loss of biodiversity, and soil acidification (e.g., Baron, 2006; Boot et al., 2016; Walker et al., 2019a). These deleterious effects have been observed in several high alpine ecosystems of the western U.S (Baron et al., 2000; Burns, 2003). The high-elevation ecosystems of the Rocky Mountains are especially sensitive to excess reactive nitrogen inputs because they developed under nutrient-deprived conditions. The elevation profile of the region of interest is shown in Figure 4.1a. This region is also home to several national Parks, many of which are located within 100 km of an agricultural NH_3 emissions hotspot (Pan et al., 2021).

Figure 4.1b shows National Emissions Inventory (NEI) estimates of NH_3 emissions from agriculture by county in 2020 (US EPA, 2020). The key agricultural areas to be discussed here are the San Joaquin Valley (SJV), the Snake River Valley (SRV), northeast Colorado (NE CO), and the

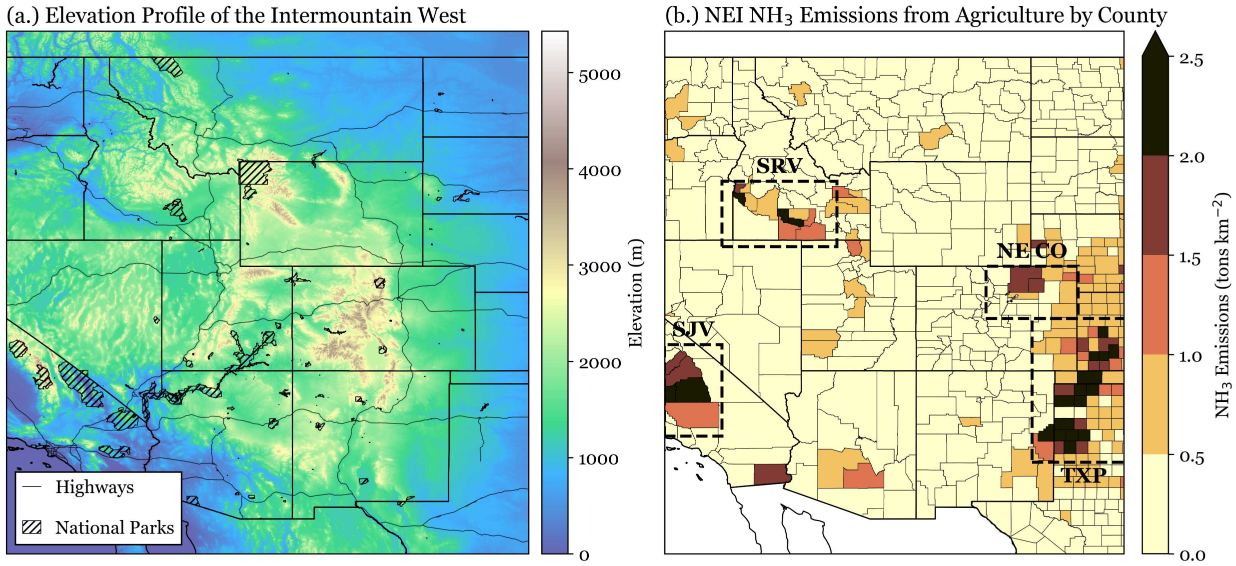
(a.) Elevation Profile of the Intermountain West

(b.) NEI NH_3 Emissions from Agriculture by County

Figure 4.1: The region of study is shown. (a.) Terrain elevation from the Global Multi-level Terrain Elevation Data 2010 (GMTED2010) is shown. (b.) The summed county emissions of NH_3 from agricultural activities from the 2020 NEI are shown. Key agricultural regions are labeled with dashed rectangles.

Texas Panhandle (TXP). In the US, agricultural activities accounted for more than 80% of NH_3 emissions in the NEI (2020). Globally, an estimated 81% of all NH_3 emissions have been attributed to agricultural activities (Wyer et al., 2022). From 1950 to 2000, estimated NH_3 emissions more than doubled, with a majority of the increase in anthropogenic emissions attributed to nitrogen fertilizer application and livestock production (Beusen et al., 2008; Bouwman et al., 1997; Lamarque et al., 2010). NH_3 emissions in Figure 4.1b illustrate the spatial pattern of estimated agricultural NH_3 emissions in the western Great Plains, Rocky Mountain, and intermountain west regions, including heavy agricultural activities in northeast Colorado, the Snake River Valley in Idaho, the San Joaquin Valley in California, and the northern Texas panhandle into Oklahoma, Kansas, and Nebraska. Northeast Colorado and the Snake River Valley in Idaho, both close to national parks (Rocky Mountain, Grand Teton, and Yellowstone) with protected visual landscapes and deposition-sensitive, high-elevation ecosystems, will be the primary focus of this work.

Wildfire smoke is also an important source of NH_3 to the atmosphere (Benedict et al., 2017; Lindaas et al., 2021; Roberts et al., 2020). Wildfires typically emit more NH_3 during low-temperature burning (Burling et al., 2010; Goode et al., 1999). After agricultural (livestock and fertilizer-related) emissions, the second largest NH_3 emission source in the US is biomass burning, predominantly attributed to wildfires (US EPA, 2020). Agricultural fires are also a source of NH_3 (Tomsche et al., 2023). In the 2020 NEI, NH_3 emissions from wildfires, agricultural fires, and prescribed burning accounted for 54%, 24%, and 22% of biomass burning emissions, respectively (US EPA, 2020). The western US experiences significant wildfire activity, the frequency of which has been increasing (Bray et al., 2018; Corwin et al., 2022; Zhuang et al., 2021). Wildfires typically occur during the warm season in the western US, with greater than 90% of wildfires occurring from May to September from 2005 to 2019 (Picotte et al., 2020). Wildfire smoke plumes inject emissions of NH_3 higher into the atmosphere, which may increase the atmospheric lifetime, increasing potential for particle formation and the distance NH_3 can travel before deposition (Lindaas et al., 2021).

Model simulations, *in situ* measurements, and satellite retrievals over the contiguous US show increasing NH_3 (e.g., Butler et al., 2016; Wang et al., 2023; Warner et al., 2016; Yu et al., 2018). These increases range from 2-12% per year. To better understand the emission sectors driving these changes, NH_3 observations and modeled smoke plumes are used to attribute increases in NH_3 to wildfire smoke and agricultural areas. Spatial and annual trends are assessed using monthly Level 3 data from the Infrared Atmospheric Sounding Interferometer (IASI) satellite and oversampled data from the Cross-Track Infrared Sounder (CrIS) satellite. For both datasets, the largest increases are observed during the 2013 to 2023 study period above agricultural regions. Modeled smoke plumes are used to remove CrIS pixels impacted by smoke, allowing for the relative trend attributed to wildfire smoke to be assessed. Lastly, the oversampled data are used to assess the spatial footprint of agricultural NH_3 emission hotspots.

4.2 Methods

4.2.1 Satellite data

This analysis uses total column NH_3 retrievals from the European Space Agency's Infrared-Atmospheric Sounding Interferometer (IASI) and the National Aeronautics and Space Administration's (NASA) Cross-Track Infrared Sounder (CrIS). Both polar-orbiting satellites use a Fourier-Transform Spectrometer to make observations. The IASI data used is a post-processed Level 3 product at a monthly temporal resolution. The CrIS data were processed using a physical oversampling method to a finer grid resolution of 2 km. A major difference between the observations from IASI and CrIS NH_3 is the overpass time, at 09:30 and 13:30 local time, respectively. NH_3 has a strong diurnal cycle, as observed in Chapter 2, and NH_3 concentrations are expected to be higher during the CrIS afternoon overpass. Key differences between the two satellite products are summarized in Table 4.1. Satellite NH_3 data were considered for the western US, including latitudes spanning from 30 to 50 degrees and longitudes spanning from -100 to -120 degrees. This region is plotted in Figure 4.1.

Table 4.1: Key differences between the IASI and CrIS satellite data used are summarized.

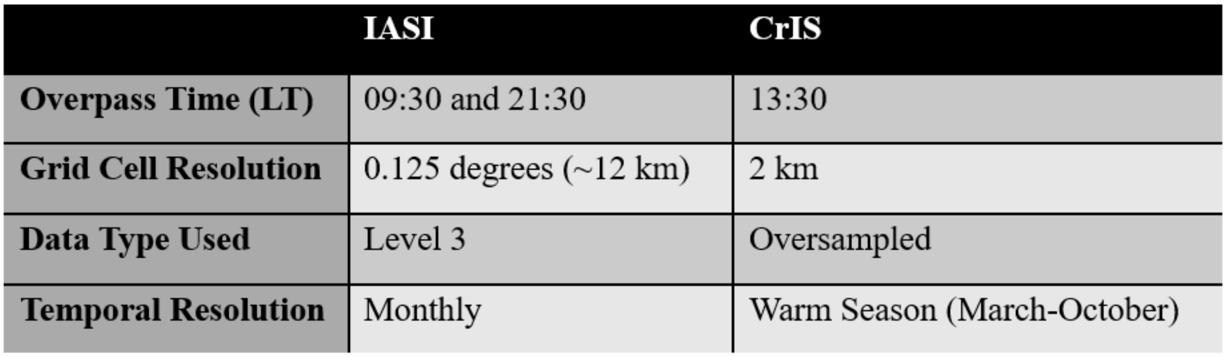

	IASI	CrIS
Overpass Time (LT)	09:30 and 21:30	13:30
Grid Cell Resolution	0.125 degrees (~12 km)	2 km
Data Type Used	Level 3	Oversampled
Temporal Resolution	Monthly	Warm Season (March-October)

Infrared-Atmospheric Sounding Interferometer (IASI)

IASI provides total column NH_3 concentrations from twice daily retrievals at 09:30 and 21:30 local time. The pixel diameter is 12 km at nadir. IASI uses a scanning Fourier transform spectrometer in the infrared band between 3.4 and 15.5 microns (Clarisse et al., 2009; Van Damme et al., 2015). IASI is located on the Meteorological Operational satellites (MetOp) operated by the European Organization for the Exploitation of Meteorological Satellites (EUMETSAT), and developed by the European Space Agency

IASI data were obtained from the Meteorological Operational (MetOp) B satellite. IASI data are also available from MetOp-A and MetOp-C, launched in 2006 and 2018, respectively. MetOp-A ended its mission in 2021. Data from MetOp-B were selected due to its temporal overlap with the CrIS data used. Data are available for download at (https://iasi.aeris-data.fr/catalog). Data span from March 8, 2013, to December 31, 2023. For this application, the level 3, Version 4 Artificial Neural Network with Reanalysis (ANNI-NH3-V4R) product was used, which offers monthly data at 0.125 by 0.125-degree grid cell resolution. For the area of interest, this is approximately a 12 km grid cell resolution. ANNI Version 4 introduced a total column averaging kernel and improved the consistency of measurements (Clarisse et al., 2023). The reanalysis version relies on ERA5 ECMWF meteorological input data, surface temperature, and cloud retrievals (Hersbach et al., 2020; Van Damme et al., 2018). Only the morning overpasses (09:30 local time) were analyzed due to their higher daytime thermal contrast (Clarisse et al., 2010). IASI retrievals are well correlated with ground-based measurements, showing good agreement for NH_3 spatial patterns (Guo et al., 2021; Wang et al., 2023).

Cross-Track Infrared Sounder (CrIS)

CrIS provides a daily retrieval at 13:30 local time. The pixel field of view (FOV) is 14 km in diameter. CrIS also uses a scanning Fourier transform spectrometer, operating in the infrared band from 3.92 to 15.38 microns. CrIS is located on Suomi National Polar-orbiting Partnership (SNPP), National Oceanic and Atmospheric Administration (NOAA) 20 (Formerly Joint Polar Satellite System-1 (JPSS-1)), and NOAA-21 (Formerly Joint Polar Satellite System-2 (JPSS-2)) satellites, launched in 2011, 2017, and 2022, respectively. Data from CrIS located on SNPP are used for this analysis, due to its longer data record (Han et al., 2013). CrIS has peak sensitivity to NH_3 below the top of the boundary layer at ~850–750 hPa (Shephard and Cady-Pereira, 2015). CrIS NH_3 retrievals are well correlated with the spatial variability of other satellite observations and *in situ* ground observations (Cady-Pereira et al., 2024; Ding et al., 2024).

The CrIS data were processed using a physical oversampling method to generate annual gridded data for the warm season. Physical oversampling describes the process by which retrieved satellite pixels are averaged over time to a grid that is significantly finer than the original pixel size. In this case, level 2 CrIS satellite pixels with 14 km diameter FOV are averaged over the warm season to generate a 2 km resolution gridded level 3 product. The warm season was defined as March to October, to capture peak NH_3 emissions and wildfire activity. NH_3 has a strong seasonal cycle, as shown in Chapter 3, with peak emissions occurring during the summer and fall in the region of interest. To understand the impact of wildfire smoke, additional oversampled CrIS data products were generated by removing pixels considered to be smoke-impacted.

Smoke plume data were taken from the Hazard Mapping System (HMS) (data available at: https://www.ospo.noaa.gov/Products/land/hms.html) operated by the NOAA National Environmental Satellite, Data, and Information Service (NESDIS). To generate the HMS dataset, analysts use a suite of satellite data products to manually outline the extent of detected smoke plumes. HMS smoke plumes are given a qualitative density flag (light, medium, or heavy). HMS smoke plumes have been used to estimate smoke exposure, assess smoke trends, and determine radiative impacts of smoke plumes (Corwin et al., 2025; Corwin et al., 2022; O'Dell et al., 2021; Zhou et al., 2021). HMS smoke plumes between 19:30 UTC and 21:30 UTC were used to determine CrIS pixels impacted by smoke. Two oversampled CrIS datasets with smoke removed were generated: 1. Smoke plumes of all qualitative density flags, and 2. Only smoke plumes flagged as medium or heavy smoke. The CrIS datasets are named as shown in Table 4.2.

To directly compare CrIS and IASI data, the CrIS data were also down-sampled to the IASI grid system. The IASI and CrIS grids do not align, requiring a weighted average of gridded CrIS cells onto the IASI grid system.

4.2.2 Monthly reanalysis meteorological data

Monthly mean meteorological data were taken from version 5 reanalysis data (ERA5) from the European Centre for Medium Range Weather Forecast (ECMWF) (Hersbach et al., 2020). The spatial resolution of this data are 0.25 degrees. Data were used from 2013 to 2023 across the region

Table 4.2: The physical oversampled datasets are described, with a summary of key features.

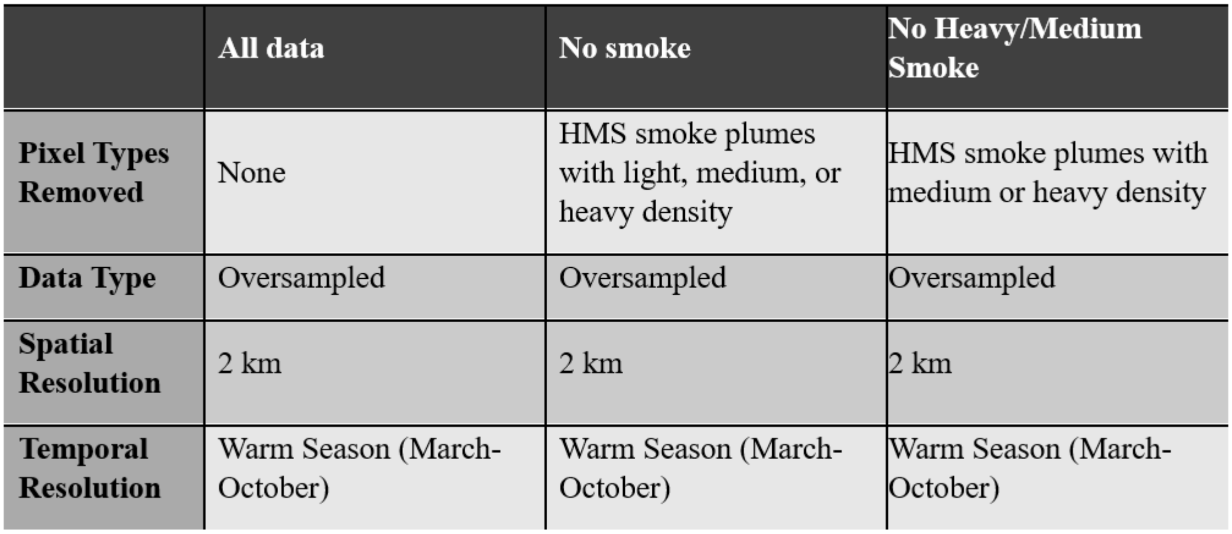

	All data	No smoke	No Heavy/Medium Smoke
Pixel Types Removed	None	HMS smoke plumes with light, medium, or heavy density	HMS smoke plumes with medium or heavy density
Data Type	Oversampled	Oversampled	Oversampled
Spatial Resolution	2 km	2 km	2 km
Temporal Resolution	Warm Season (March-October)	Warm Season (March-October)	Warm Season (March-October)

of interest (last accessed: 05/22/2025). Two-meter temperature data were analyzed for potential impact on NH_3 emissions.

4.2.3 Theil-Sen regression and statistical significance testing

Time-series trends are calculated as described in Chapter 3, using a Theil-Sen estimator (Sen, 1968). The Theil-Sen estimator is non-parametric and less sensitive to outliers than optimized least squares linear regression. The Theil-Sen estimator takes the slope between each unique pair of data points and estimates the trend as the median value. Unless otherwise noted, statistical significance is determined using a Mann-Kendall test at the 95^{th} percentile confidence level (Hussain et al., 2019).

4.2.4 Hotspot contouring method

NH_3 hotspots in the CrIS data were identified using a clustering algorithm with a binary cut-off at the 95^{th} percentile of the column distribution across all study years (2.07×10^{16} molec. cm^{-2}). This method was first proposed by Wang et al. (2021) using an oversampled IASI NH_3 dataset at 2 km resolution. Wang et al. (2021) used an annually averaged map across their entire data period (2008-2017) and generated contours using the 95^{th} percentile of column distribution (0.66×10^{16} molec. cm^{-2}). In this analysis, hotspots contours are computed for the annual warm season (March-October) CrIS oversampled maps. The 95^{th} percentile used is approximately 3 times larger than that used in Wang et al. (2021). This could be due to a variety of factors: 1. The CrIS overpass time is in the early afternoon (13:30 LT), and the IASI overpass time is in the morning (09:30 LT), 2. The data used by Wang et al. (2021) is a full-year average, and the CrIS oversampled data used here is from only the warm season months.

The contours were determined using the Hoshen-Kopelman (H-K) clustering algorithm (Hoshen and Kopelman, 1976). The H-K algorithm labels clusters based on a binary cut-off, here the 95^{th} percentile value, and connects them to neighboring cells. Contours were determined using the 4-member connected neighborhood, considering the cells above, below, left, and right of the initial labeled cell. The H-K algorithm labels all clusters above the cut-off, even single grid cell clusters. Single grid cell clusters were ignored for this analysis. The H-K algorithm was selected instead of a matching-squares algorithm because it preserves the native grid system resolution. However, preservation of the native grid system resolution means that this algorithm is very sensitive to the native grid cell resolution (Wang et al., 2021). For each computed hotspot contour, the characteristic length scale was determined as the square root of the contour area.

4.3 Results and discussion

4.3.1 Comparison of IASI and CrIS total column concentrations

The comparison of results from different satellites is a non-trivial problem. The IASI and CrIS satellite products have different overpass times, a different pixel size at nadir, and use different retrieval algorithms. Although they both use a Fourier transform spectrometer, the algorithm used to determine total column NH_3 concentrations differs significantly. Other key differences between the CrIS and IASI datasets used here are outlined in Table 4.1. To briefly investigate the relative differences between the CrIS and IASI datasets used, the warm season (March-October) mean total column NH_3 is compared for both datasets in Figure 4.2. The spatial patterns in CrIS (Figure 4.2a) and IASI (Figure 4.2b) mean total column NH_3 concentrations are broadly similar, with the largest NH_3 column concentrations occurring above agricultural areas (see Figure 4.2b). However, the CrIS NH_3 values are generally larger (note the different color bar maxima in Figure 4.2a and Figure 4.2b). Figure 4.2c shows the difference between NH_3 column concentrations from CrIS and IASI. Positive (negative) values mean that the CrIS total column NH_3 concentration is larger (smaller) than the IASI total column NH_3 concentration. CrIS NH_3 concentrations generally exceed IASI concentrations by approximately a factor of 2. The diel pattern of NH_3 emissions from agriculture is highest in the early afternoon, which corresponds to the CrIS overpass time of 13:30 LT. In contrast, the IASI overpass time is 09:30 LT, and likely precedes daily maximum NH_3 values. The difference in overpass time could explain the larger total column NH_3 values observed by CrIS. Notable exceptions occur above the Great Salt Lake in Utah and the San Joaquin Valley in California, perhaps resulting from differences in how the satellite retrieval algorithms handle changes in surface reflectivity.

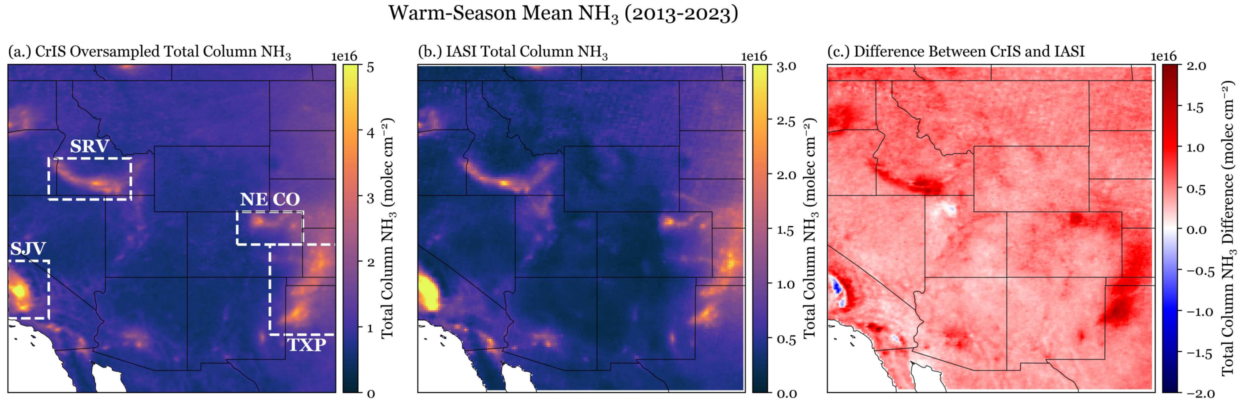

Figure 4.2: The warm season (March-October) mean total column NH_3 from 2013-2023 is plotted for (a.) the oversampled CrIS data product, and (b.) the Level 3 IASI data product. (c.) The difference between these datasets, computed on the IASI grid, is shown. Key agricultural regions are labeled with white rectangles in subplot a.

4.3.2 Agricultural hotspot contouring

The spatial footprint of elevated NH_3 concentrations has important implications for deposition and transport into sensitive ecosystems. Figure 4.3a shows annual NH_3 hotspot areas identified across the study region. The hotspots in Figure 4.3 are contoured using the 95^{th} percentile across the data record (2.07×10^{16} molec. cm^{-2}). This value is larger than the 95^{th} percentile used by Wang et al. (2021), who defined hotspot contours across the entire year. Here, they are defined for only the warm season, and the threshold is higher due to the seasonal cycle of NH_3 with greater summertime emissions.

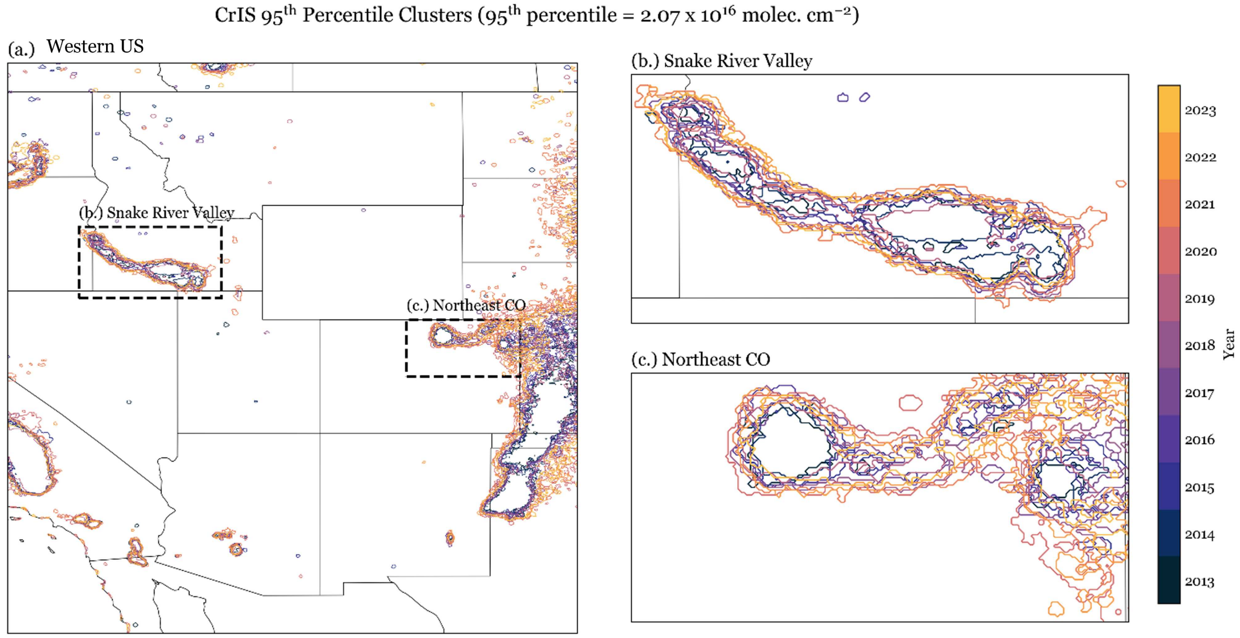

Figure 4.3: NH_3 hotspots, contoured using the H-K algorithm at the 95^{th} percentile (2.07×10^{16} molec. cm^{-2}), are shown for each year (2013-2023) for (a.) the entire region of interest, (b.) the Snake River Valley, and (c.) northeast Colorado.

Each year, hotspot contours are plotted separately for the Snake River Valley in Figure 4.4 and northeast Colorado in Figure 4.5. These annual plots are used to more clearly illustrate interannual changes in hotspot areas. The Snake River Valley and northeast CO hotspot contours are more fragmented and occupy a smaller spatial area in earlier years than in later years, revealing growth in the spatial footprint of influence from agricultural emissions over the study period.

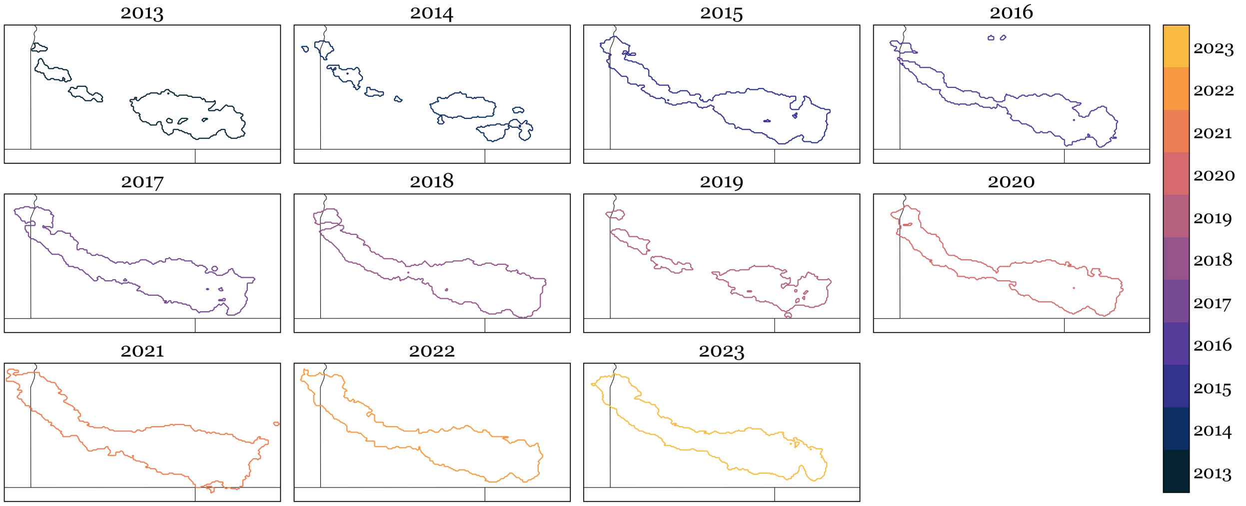

Figure 4.4: NH_3 hotspots, contoured using the H-K algorithm at the 95^{th} percentile (2.07×10^{16} molec. cm^{-2}), are shown for each year (2013-2023) in the Snake River Valley.

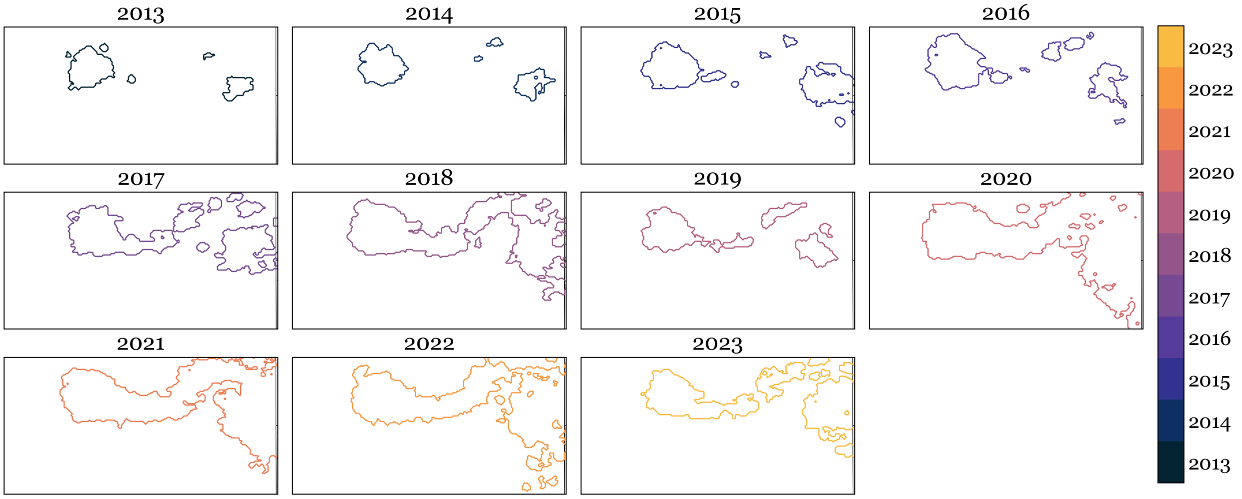

Figure 4.5: NH_3 hotspots, contoured using the H-K algorithm at the 95^{th} percentile (2.07×10^{16} molec. cm^{-2}), are shown for each year (2013-2023) in northeast Colorado.

The hotspot area in northeast Colorado is the largest in 2020 when the Cameron Peak Fire, the largest wildfire in Colorado's history, was burning approximately 50 km west of the highlighted agricultural area. A drop in hotspot area was seen in both regions in 2019 when wildfire smoke levels were low over both regions.

To quantify the increasing spatial footprint of NH_3 hotspots, their annually summed areas are plotted in Figure 4.6. Trends are assessed for the full dataset and the dataset with smoke removed. The area of agricultural hotspots is increasing by 7% yr^{-1} across the study region (Figure 4.6).

This spatial increase was enhanced by wildfire smoke, dropping to 6% yr^{-1} when the influence of thick smoke plumes (HMS medium + heavy flags) was removed. The area of agricultural NH_3 hotspots in the Snake River Valley increased by 6% yr^{-1}, falling to 5% yr^{-1} when thick smoke plumes are removed. The most rapid increase in agricultural hotspot area occurred in northeast Colorado, at 15% yr^{-1}, falling to 12% yr^{-1} when thick smoke plumes were removed.

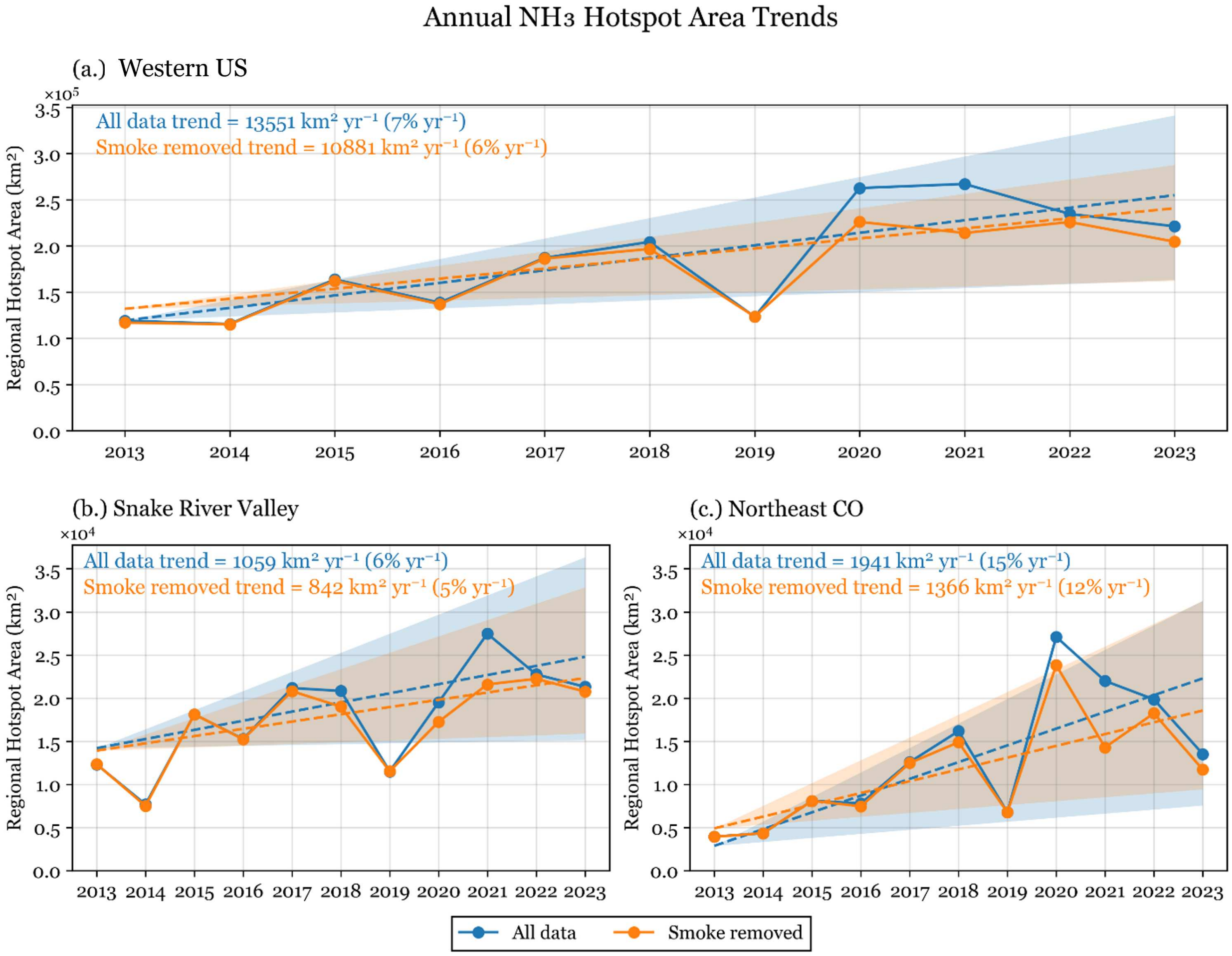

Figure 4.6: The annual summed area of NH_3 hotspots, contoured using the H-K algorithm at the 95^{th} percentile (2.07×10^{16} molec. cm^{-2}), is shown for (a.) the entire region of interest, (b.) the Snake River Valley, and (c.) northeast Colorado. Trends are assessed using a Theil-Sen regression for the full dataset and the dataset with smoke impacts removed. The 95% confidence level of the trend is shaded.

The increase in agricultural hotspot area could indicate that the spatial footprint of agricultural activities is increasing or that the emissions and/or transport of NH_3 out of static agricultural emission areas is increasing. Independent of the cause, increasing the spatial footprint of NH_3 concentrations from agriculture may increase the transport and deposition of NH_3 to sensitive ecosystems situated close to agriculture.

4.3.3 Trends in atmospheric NH_3 concentration

Total column NH_3 concentration 2013-2023 time series trends were calculated using a Theil-Sen regression on the IASI dataset. The seasonal cycle was removed from the monthly Level 3 IASI dataset by subtracting the full dataset's monthly means before trend analysis was conducted. Figure 4.7a shows the slope of the regression calculated for each IASI grid cell. The largest trends in NH_3 concentration are observed in regions of agricultural activities. However, the San Joaquin Valley in California has some of the highest NH_3 concentrations in Figure 4.2, and the calculated NH_3 trend is small compared to the other agricultural areas. The trend in NH_3 concentration from only the warm season is shown in Figure 4.7b.

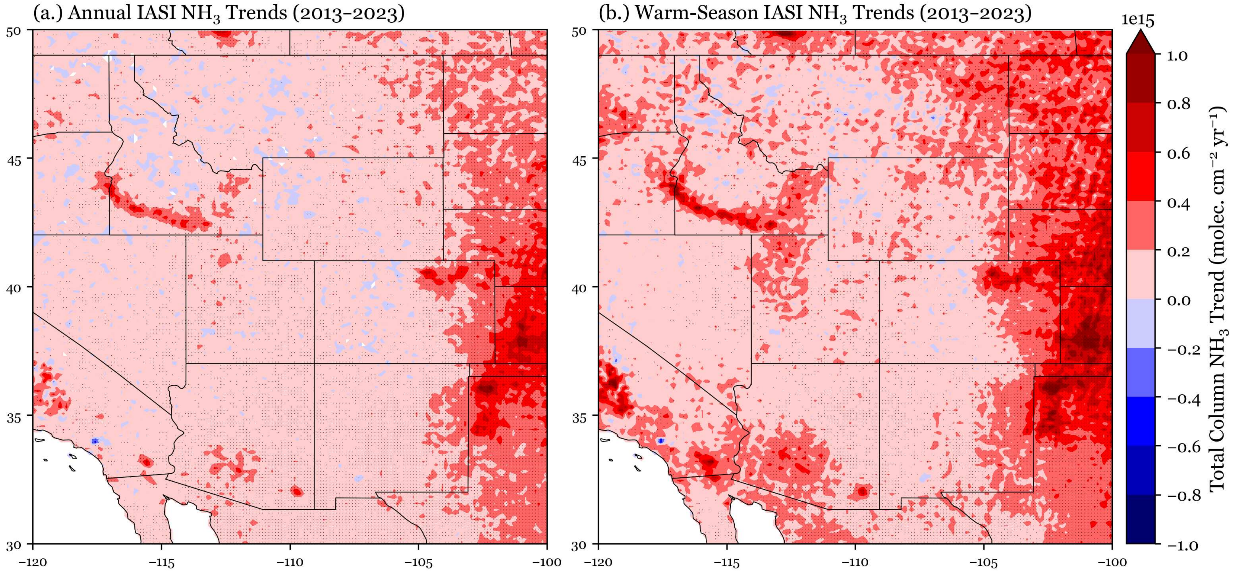

Figure 4.7: The annual trend in total column NH_3 concentration is shown. Stippling indicates statistical significance at the 95% confidence interval. (a.) A Theil-Sen regression is computed for each grid cell on the Level 3 monthly IASI dataset. The seasonal cycle was removed by subtracting the monthly mean across the data record. (b.) A Theil-Sen regression is computed for each grid cell on the warm season mean IASI total column NH_3 concentrations.

The spatial pattern of the warm season NH_3 trend is comparable to the full-year trend, with the largest increases in NH_3 occurring above regions of agricultural activity. The magnitude of the observed trends across the study region is larger when only the warm season data are considered. The warm season is also when NH_3 emissions are expected to be the largest from both agricultural and wildfire sources. There is also a region of stronger NH_3 increase during the warm season trend analysis in the north-east corner of Figure 4.7b. Considering the areas of strongest NH_3 emissions (see Figure 4.1), this region is not associated with large agricultural emissions. The increasing trend, therefore, could instead be associated with increasing NH_3 from wildfire smoke. In the warm season data, an increase in the San Joaquin Valley of California is more clearly observed.

All regions with the largest warm season mean NH_3 total column concentrations (see Figure 4.1) have strong NH_3 increases in Figure 4.7, except the San Joaquin Valley in California. One possible explanation for the difference could be more active efforts in California to control NH_3 emissions. Another could be spatial differences in surface warming trends that are expected to lead to increased NH_3 volatilization. Figure 4.8 shows the trend in 2013-2023 monthly 2-meter temperature from ERA5 reanalysis. Temperature is increasing strongly in northeast Colorado, north Texas, and in the northeast corner of the overall region of interest. These are also areas of strong NH_3 total column increases as shown in Figure 4.7. The temperature in the Snake River Valley is more spatially variable, and increases are weaker than those observed to the east. In the southern end of the San Joaquin Valley, temperatures are decreasing. The decrease in temperature could help explain the lack of an increasing NH_3 trend in the San Joaquin Valley.

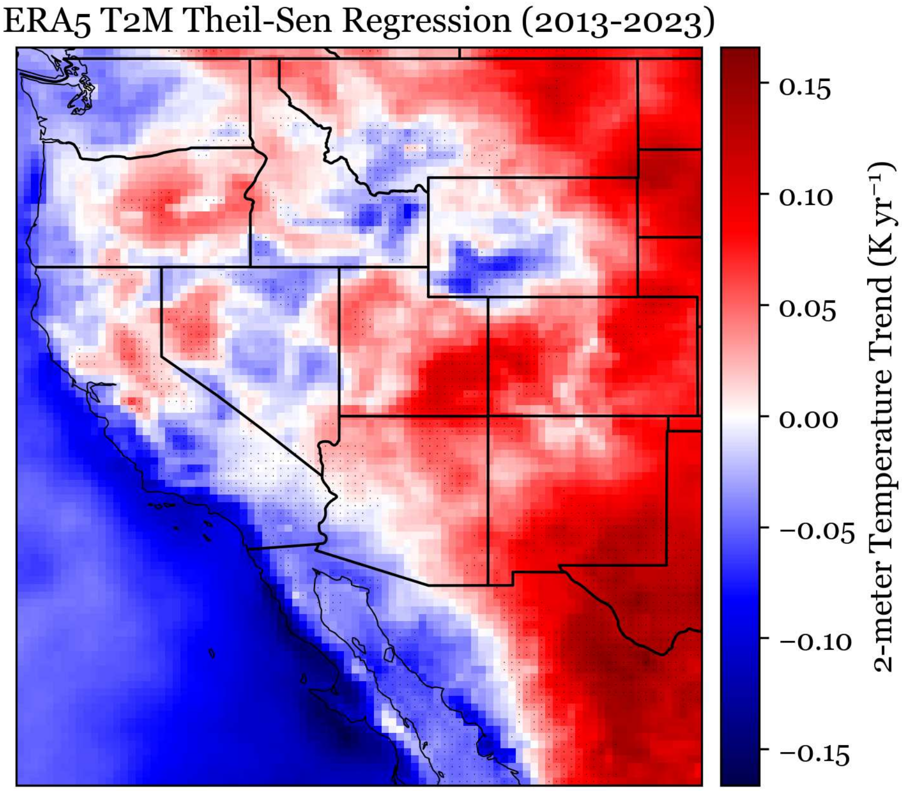

Figure 4.8: The annual trend in 2-meter temperature (T2M) from ERA5 reanalysis is shown. Stippling indicates statistical significance at the 95% confidence interval.

To further investigate the seasonal changes in NH_3, month-specific NH_3 trends were calculated for the IASI dataset. Figure 4.9 groups these trends seasonally and shows the spatial pattern of NH_3 trends for each month. NH_3 trends during the cooler months, November (Figure 4.9l), December (Figure 4.9a), January (Figure 4.9b), and February (Figure 4.9c), are typically not statistically significant and have high spatial variability. Total column NH_3 increases are the strongest in the warmer months from May (Figure 4.9f) to October (Figure 4.9k), especially above key agricultural source regions. During June (Figure 4.9g), we observe a strong increasing trend in the northeast corner of the study region. As discussed above, this region does not correspond to one of the higher agricultural NH_3 source regions per the NEI. In the monthly NH_3 trends, we observe one statistically significant instance of large ammonia decreases, in the San Joaquin Valley, during March (Figure 4.9d). NH_3 also decreased across Montana, during August (Figure 4.9i), although the trends were generally not statistically significant.

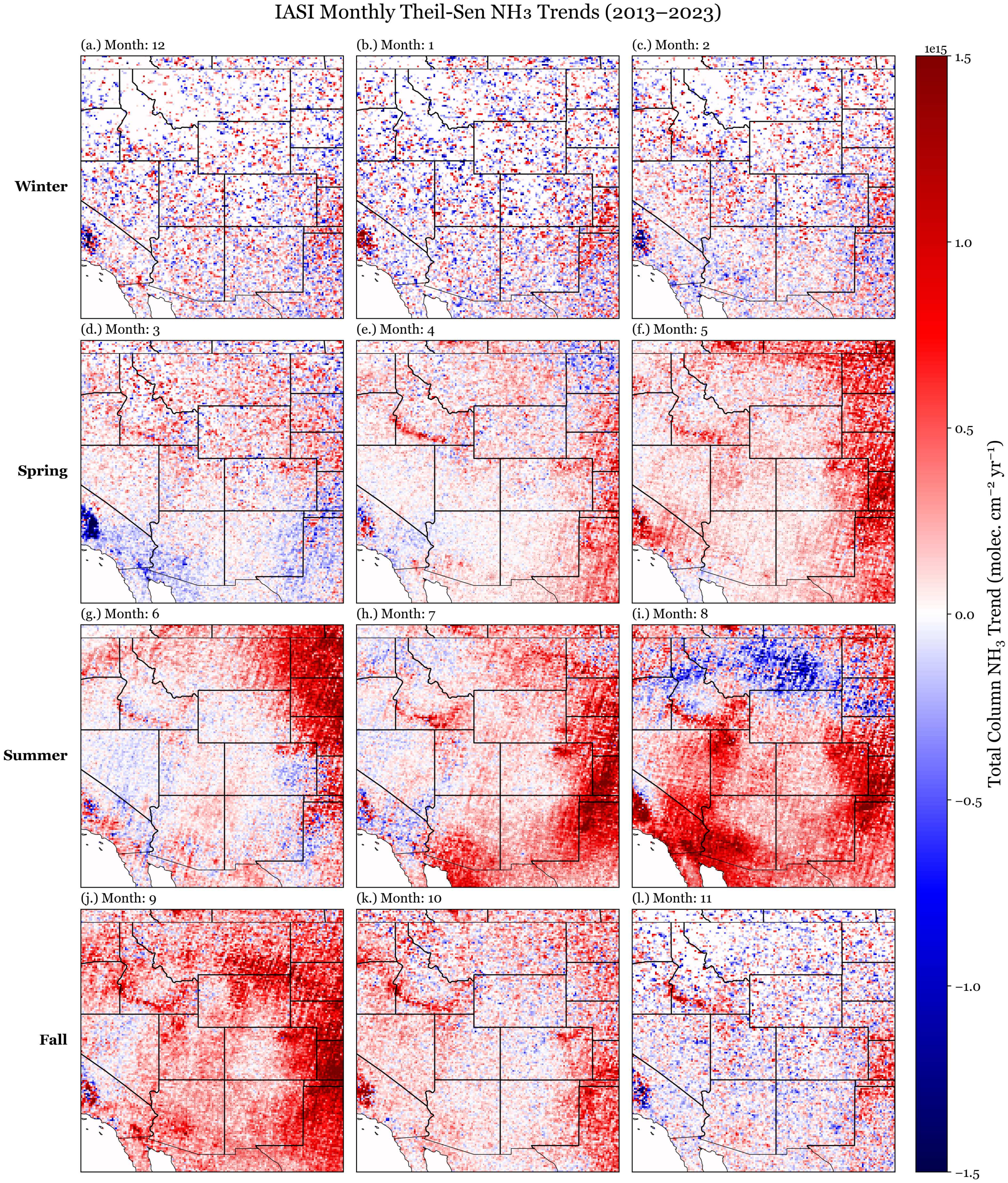

Figure 4.9: The trend in IASI total column NH_3 concentration is shown for each grid cell and each month of the year using a Theil-Sen regression. Stippling indicates statistical significance at the 95% confidence interval. Monthly trends are grouped by season.

The warm season 2013-2023 total column NH_3 trends from the CrIS data product were also assessed using a Theil-Sen regression. The total column NH_3 concentration trends for each CrIS grid cell, at 2 km resolution, are shown in Figure 4.10a. As in the IASI data, the strongest NH_3 increases are occurring in northeast Colorado, the Snake River Valley, and the Texas Panhandle. We also observe a strong NH_3 trend across the Canadian border in southern Alberta, on the edge of our region of interest. In Figure 4.10b, the same regression is applied to the CrIS data product recast to the IASI grid system. This allows for more direct comparison with the IASI NH_3 trend results (Figure 4.7b) and emphasizes large-scale features. The strongest NH_3 increases for both grid systems occur in the agricultural regions, except for California's San Joaquin Valley, which does not have a clear spatial pattern of increasing NH_3. The NH_3 increases observed in the CrIS data are generally larger magnitude, but similar percentage increases, than those observed in the IASI data (see Figure 4.7). This may reflect the difference in satellite overpass times, with larger NH_3 increases occurring during the peak NH_3 emission period observed during the afternoon CrIS overpass (13:30 LT).

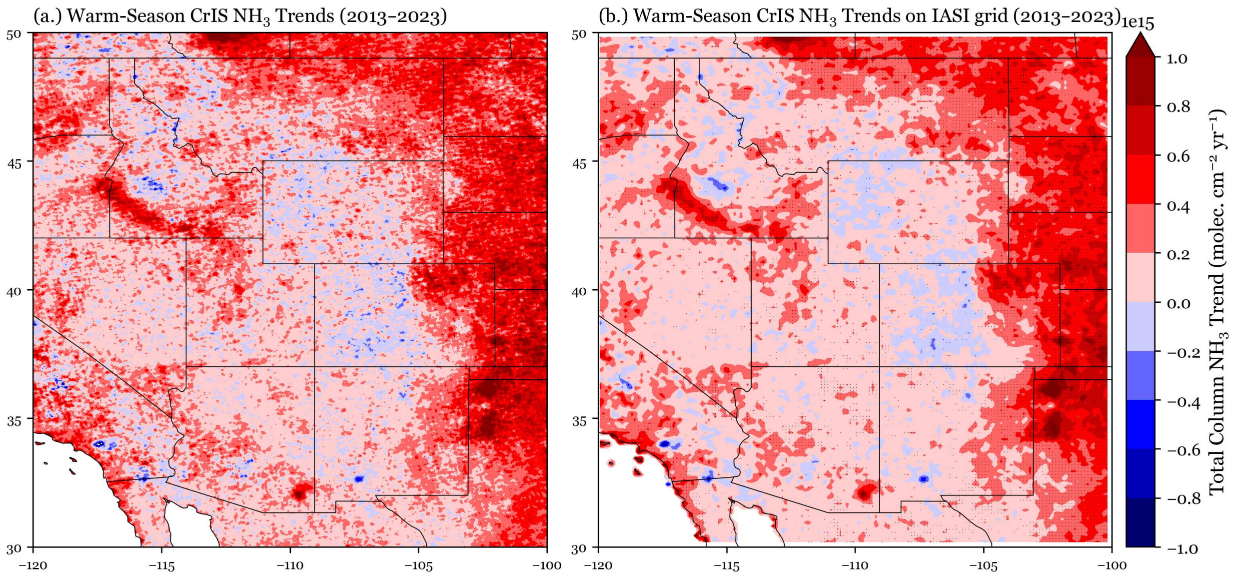

Figure 4.10: The trend in total column NH_3 concentration is shown for each grid cell using a Theil-Sen regression for (a.) the native CrIS oversampled dataset grid, and (b.) the CrIS data recast to the IASI grid. Stippling indicates statistical significance at the 95% confidence interval.

To better understand changing NH_3 in each emission hotspot, trend analysis was conducted for the spatial mean warm season NH_3 concentration within each hotspot. NH_3 hotspots were determined, as discussed above, using the Hoshen-Kopelman method and contouring at the 95^{th} percentile. Figure 4.11a shows the mean hotspot contouring area from 2013 to 2023, colored by the slope of the NH_3 column concentration trend. Within the region, statistically significant trends in mean total column NH_3 concentration are observed in the Snake River Valley, northeast Colorado, the Texas panhandle into Nebraska, and in southern Alberta, Canada, at the edge of our study region. NH_3 hotspot regions in Oregon, California, Arizona, and New Mexico do not have statistically significant trends in NH_3 column concentration. The statistically significant trends range from 3.3×10^{14} to 1.2×10^{15} molec. cm^{-2} yr^{-1}. Figure 4.11b shows the same total column NH_3 trends relative to the hotspot mean NH_3 concentration. The statistically significant trends range from 1.5 to 4.6% yr^{-1}.

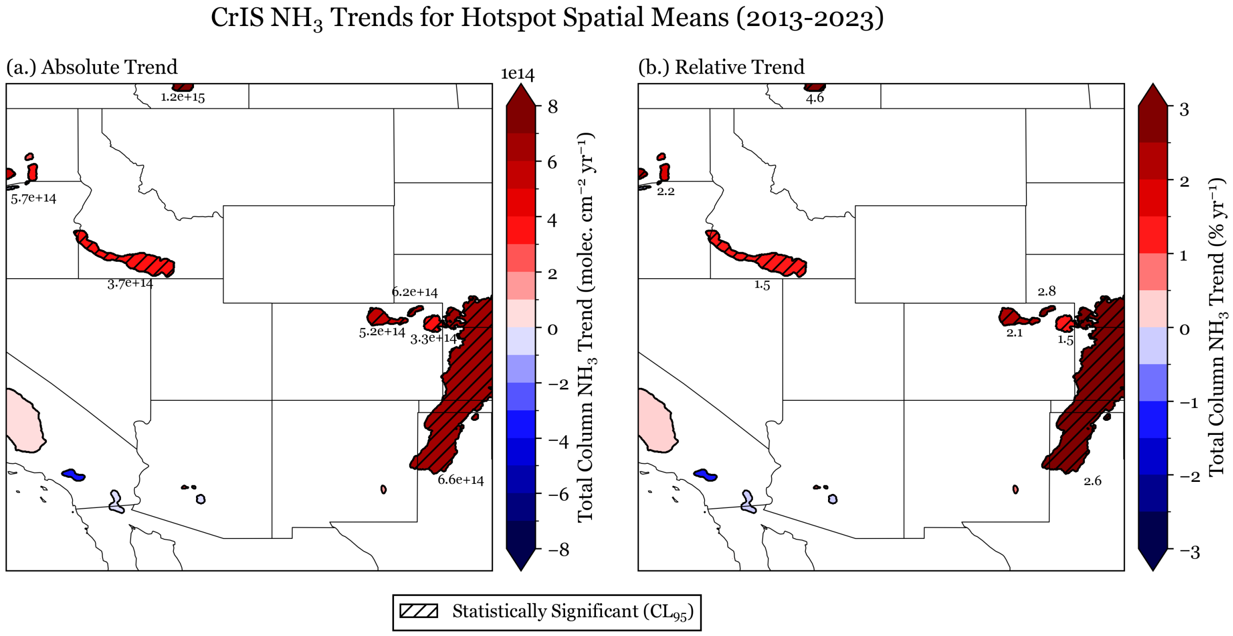
CrIS NH_3 Trends for Hotspot Spatial Means (2013-2023)

(a.) Absolute Trend

(b.) Relative Trend

Figure 4.11: The (a.) absolute and (b.) relative trend in spatial mean total column NH_3 concentration is shown for each hotspot area using a Theil-Sen regression. Hatching indicates statistical significance at the 95% confidence interval. Slope values are printed for statistically significant trend regions.

4.3.4 Contributions of wildfire smoke to increasing NH_3

Wildfire smoke is also an important source of NH_3 to the atmosphere. The frequency of wildfires and the subsequent frequency of overhead smoke have increased in the western US in recent years (Corwin et al., 2022). To assess the impact of wildfire smoke on NH_3 concentration from CrIS, pixels determined in the HMS smoke identification product to be impacted by smoke were removed to generate smoke-free oversampled data. Figure 4.12b shows the spatial pattern of total column NH_3 trends in the CrIS warm season data, when all smoke-impacted pixels have been removed. This includes HMS smoke plumes of all three qualitative flags: light, medium, and heavy. The spatial pattern is consistent with the total column NH_3 trends plotted in Figure 4.12a, although the trend values are smaller in magnitude. This difference is illustrated in Figure 4.12c. The difference between the full dataset and CrIS retrievals with smoke removed can be interpreted as the increasing 2013-2023 NH_3 trend attributed to wildfire smoke. In most areas of the study region, wildfire smoke increased the total column NH_3 concentration trend. The wildfire smoke appears to have a disproportionate influence on NH_3 concentration changes above the Snake River Valley, and the agricultural regions located on the east edge of our study region. This could indicate a removal artifact in data processing. Wildfire smoke and the highest agricultural NH_3 emission periods both occur in summer, so if too many pixels are removed from this key season, the annual means and therefore the trend effect may be dampened.

Trend analysis was also conducted on CrIS retrievals with pixels removed only during periods of HMS-identified medium and heavy smoke (see Figure 4.13). The medium and heavy HMS flags indicate that the plume was optically thicker than during light smoke. The spatial pattern does not match the agricultural hotspot areas, indicating that we are removing the impacts of smoke and not just isolating seasonal NH_3 trend impacts. The signal difference attributed to medium and heavy smoke represents an average background NH_3 contribution of between 0 and 0.2 molec. cm^{-2} yr^{-1}, which, especially in many background areas, constitutes a significant change.

Figure 4.14 shows the percent change in CrIS total column NH_3 trends when pixels impacted by heavy and medium smoke are removed. In the Snake River Valley, northeast Colorado, and the

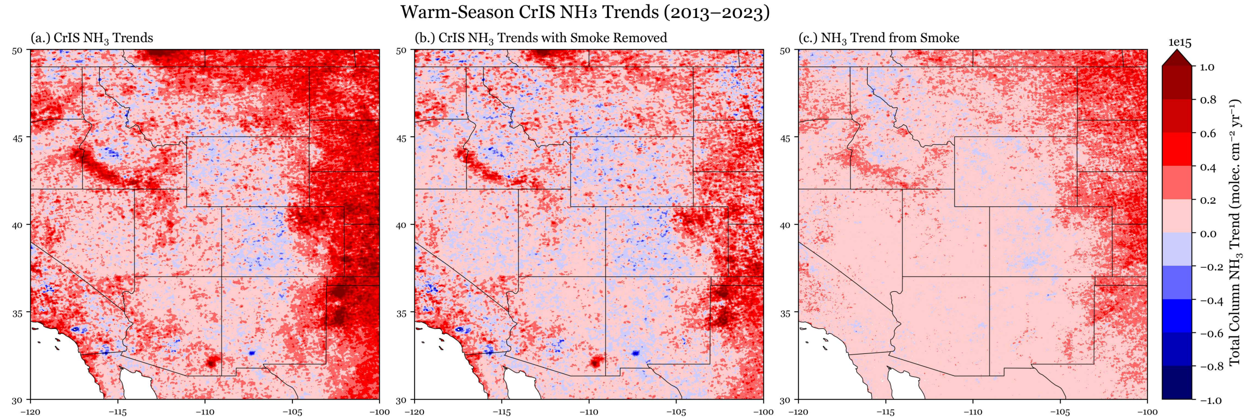

Figure 4.12: (a.) The trend in total column NH_3 concentration is shown for each grid cell using a Theil-Sen regression for the oversampled March-October 2013-2023 CrIS dataset. (b.) The trend in total column NH_3 concentration is shown for each grid cell using a Theil-Sen regression for the oversampled CrIS dataset with all smoke-impacted pixels removed. (c.) The difference between the full warm season CrIS and the smoke-free warm season CrIS total column NH_3 trends is plotted.

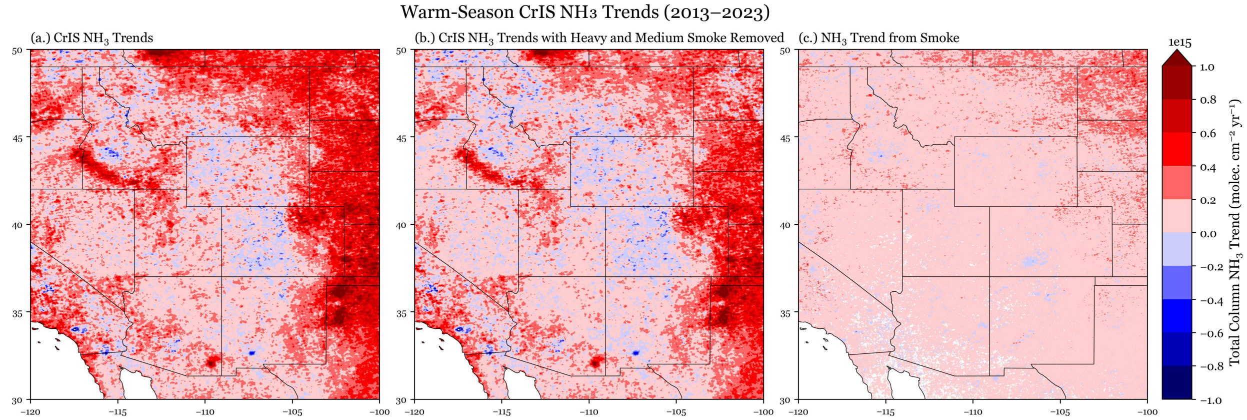

Figure 4.13: (a.) The trend in total column NH_3 concentration is shown for each grid cell using a Theil-Sen regression for the oversampled CrIS dataset. (b.) The trend in total column NH_3 concentration is shown for each grid cell using a Theil-Sen regression for the oversampled CrIS dataset with heavy and medium smoke-impacted pixels removed. (c.) The difference between the total column NH_3 trends in the full warm season CrIS and warm season CrIS with heavy and medium smoke impacts removed is plotted.

Texas panhandle, the relative difference indicates that heavy and medium smoke plumes increased the trend by less than 25%. In the remote regions, heavy and medium smoke often accounted for the entire increasing trend in NH_3, illustrating that wildfire smoke has the largest relative impact on remote regions. This is in part due to the relatively low NH_3 total column concentrations observed in these areas, but might also indicate that emissions from wildfire smoke have increased potential to impact remote ecosystems relative to changes in emissions from agriculture.

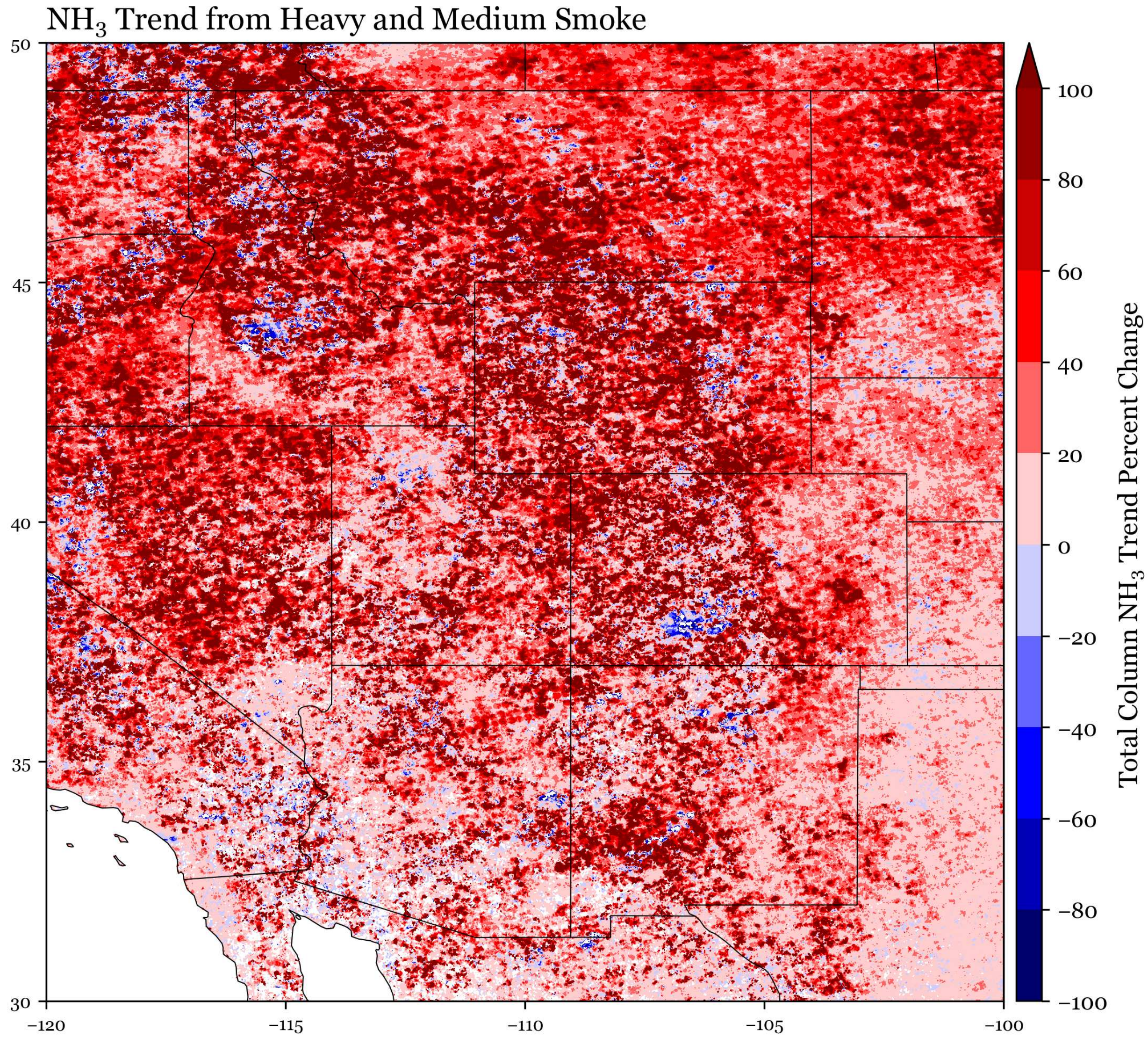

Figure 4.14: The relative difference between the total column NH_3 trends in the full warm season CrIS and warm season CrIS with heavy and medium smoke impacts removed is plotted.

Wildfire smoke generally increased the trend in total column NH_3 across agricultural and more remote regions. To better quantify the impact of wildfire smoke in agricultural regions, trends were computed for the annual spatial mean NH_3 concentrations within agricultural emission hotspot areas. Due to greater uncertainty and the potential artifact when removing light smoke plumes that can dominate peak agricultural NH_3 emission months, for the following analysis, only heavy and medium smoke plumes are considered. The mean NH_3 hotspot contours across the data record are shown in Figure 4.11. To understand regional changes across NH_3 hotspot contours, all hotspot contours within a defined region were considered together. Figure 4.15a shows the mean column concentration above all NH_3 hotspots in the western US, for each year. Column NH_3 over all hotspot regions is increasing by a mean value of 1.5% yr^{-1}. Interestingly, if the impacts of heavy and medium smoke plumes on NH_3 concentration are removed, this trend increases to 1.6% yr^{-1}. However, the confidence intervals for these two trend slopes greatly overlap, indicating that the NH_3 concentration trend within hotspots across the western US was not significantly impacted by wildfire smoke. In the Snake River Valley, the NH_3 concentration trend is not significantly impacted by wildfire smoke, with a slope of 1.5% yr^{-1} for the full dataset and dataset with smoke removed. However, the mean NH_3 concentration values across the dataset are lower by 20% when smoke is removed, suggesting that wildfire smoke in the Snake River Valley is an important source of NH_3, but has not changed significantly in recent years. Additionally, when all smoke is removed from the Snake River Valley, the trend is no longer significant due to the higher variability in observed NH_3 concentrations. Conversely, in northeast Colorado, the full 2013-2023 dataset shows an increase of 2.7% yr^{-1}, while removing smoke drops this change to 2.5% yr^{-1}, suggesting that wildfire smoke has played a role in increasing NH_3 concentrations even above agricultural emissions in northeast Colorado, but only accounts for approximately 7% of the total change.

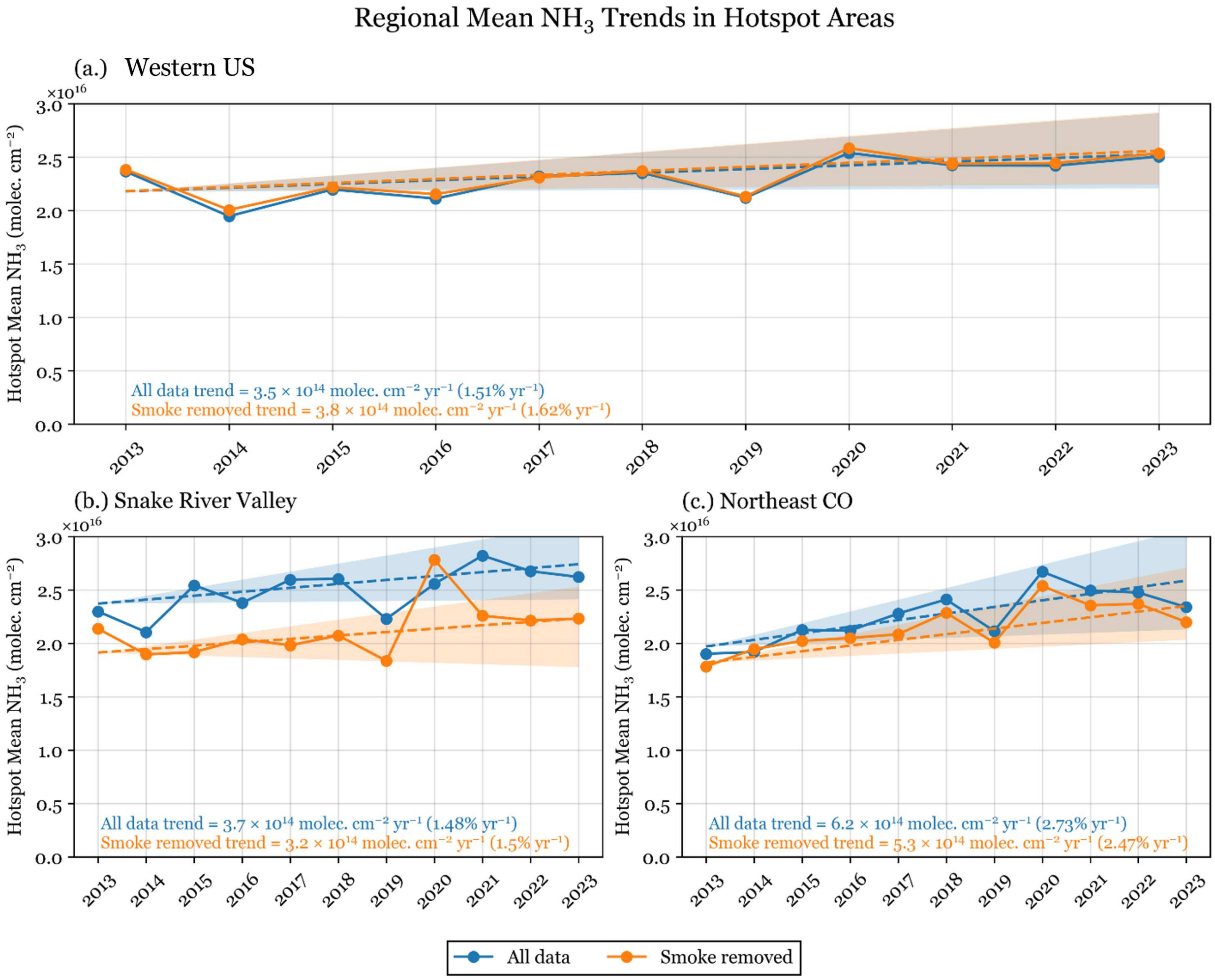

Figure 4.15: A Theil-Sen regression is applied to the spatial mean NH$_3$ total column concentration within hotspot areas contained within (a.) the western US region, (b.) the Snake River Valley, and (c.) northeast Colorado. 95% confidence intervals of the regression are shaded. All trends are statistically significant except for the smoke-removed trend in the Snake River Valley.

4.4 Conclusions

The spatial pattern of NH_3 total column concentrations in the western US is similar between IASI and CrIS satellite observations, with the highest values over regions of heavy agricultural development, including the San Joaquin Valley, Snake River Valley, northeast Colorado, and Texas Panhandle. We assessed changes to the spatial extent of agriculture NH_3 hotspots to understand how the area of impact from agricultural emissions may be changing. The area of agricultural hotspots is increasing by approximately 7% per year across the western US study region. A small portion of that change was attributed to enhanced wildfire smoke, with increasing agricultural hotspot areas falling to 6% per year when the impact of thick smoke plumes was removed. The fastest growing hotspot area was observed in northeast Colorado, at 15% per year, dropping to 12% per year when the impact of thick smoke plumes was removed. Although wildfire smoke contributed modestly to the increasing spatial extent of NH_3 hotspots, other factors appear to be dominating this trend. These could include growing NH_3 emissions from agricultural sources, an enhanced atmospheric lifetime of NH_3 (e.g., due to decreasing SO_2 and NO_x emissions over the study period that can decrease NH_3 uptake into aerosol particles), or an increasing spatial footprint of agricultural activities. Regardless, increasing the size of high NH_3 regions can enhance the likelihood of NH_3 transport to adjoining regions containing ecosystems that are sensitive to increased nitrogen deposition, including Rocky Mountain National Park in Colorado.

Annual warm season (March-October) trends were assessed across 2013-2023 for both IASI and CrIS data. The largest NH_3 increasing trends also occurred in regions of heavy agriculture. The seasonality of NH_3 column concentration trends was assessed using monthly IASI NH_3 data, revealing larger monthly increases in the warmer months of the year. Statistically significant trends across NH_3 agricultural hotspot regions ranged from 1.5 to 4.8% increase per year. Across the western US study region, removing smoke impacts did not affect the interannual NH_3 trend in agricultural regions. However, wildfire smoke impacts dominated NH_3 trends in many remote areas. NH_3 increased by 1.5% per year across the study region and in the Snake River Valley. In northeast CO, removing thick smoke plumes reduced the NH_3 increase from 2.7 to 2.5% per year, suggesting that increased agricultural emissions dominate increasing NH_3 concentrations. Northeast CO is experiencing the greatest increase in temperature, compared with other agricultural regions in the study area. Temperature-driven increases in ammonia volatilization (e.g., hotter temperatures on pen surfaces in animal feeding operations and hotter soil temperatures in fertilized fields) likely contribute to the observed NH_3 increases over agricultural source regions. Future research should examine changing agricultural practices and agricultural output along with a warming climate to assess factor contributions to observed NH_3 increases.

Chapter 5

Novel Quantification of Phosphate Wet Deposition by Flow Injection Analysis

Phosphorus is an essential nutrient for ecosystems. Its bioavailable form, phosphate (PO_4^{3-}), can enter ecosystems through wet and dry atmospheric deposition, where it may disrupt nutrient balances and negatively affect ecosystem health. Despite its ecological importance, PO_4^{3-} deposition remains understudied, and the United States lacks a national monitoring network for wet phosphorus deposition. Although flow injection analysis (FIA) is a well-established technique for determining phosphate concentrations in surface waters, it has not yet been routinely applied to quantify PO_4^{3-} in US precipitation. Low concentration values are a challenge in quantifying PO_4^{3-} in precipitation. The FIA instrument used here achieves sensitivity at low concentrations using a long flow path for absorbance to enhance sensitivity. A linear response was observed for a 7-point calibration from 0.5 to 20 μg P L^{-1}. Replicate standard analyses had a pooled relative standard deviation of 0.7%. The minimum detection limit was 0.09 μg P L^{-1}. PO_4^{3-} concentration in precipitation samples was measured at three sites in the US: 1. Rocky Mountain National Park (RMNP), 2. Mammoth Cave National Park (MACA), and 3. Fort Collins, CO (FTCW). In RMNP, snow samples were collected in distinct snow layers from a spring snowpack at two sites. Phosphate concentration ranged from 0.45 to 37.5 μg P L^{-1}. The highest PO_4^{3-} concentration was found in the lowest layer of sampling site one and could reflect P leaching from the soil, which has been observed in snow that has experienced freeze/thaw cycles. At FTCW and in MACA, individual daily precipitation events were sampled. At MACA, phosphate concentrations during winter ranged from below MDL to 8.74 μg P L^{-1}. Daily precipitation in Fort Collins, CO, during spring and summer had concentrations ranging from 1.71 to 18.7 μg P L^{-1}. PO_4^{3-} at FTCW was well correlated with calcium (R^2 = 0.86), suggesting mineral dust aerosol may be a dominant source of measured P wet deposition in these samples. Comparing results across different sampling locations, the highest median P wet deposition concentration was found in Fort Collins, CO, at 6.36 μg P L^{-1}. The lowest median P wet deposition concentration occurred at Mammoth Cave National Park, at 0.72 μg P L^{-1}.

5.1 Introduction

Phosphorus is a key nutrient for terrestrial, inland freshwater, and marine ecosystems (Mackey and Paytan, 2009; Ruttenberg, 2003). Alongside carbon (C) and nitrogen (N), phosphorus (P) plays a crucial role in global biogeochemical cycling. In contrast to N and C, P predominantly exists in the particle phase in the atmosphere and does not have a gas phase species under atmospheric conditions (Ruttenberg, 2003).

The major sources of P to the atmosphere are thought to be marine aerosols (Mahowald et al., 2008), wildfires (Bauters et al., 2021), primary biogenic aerosols (Bigio and Angert, 2018), mineral aerosols (Mahowald et al., 2008; Ruttenberg, 2003), and industrial activities (Tipping et al., 2014). Mahowald et al. (2008) reported that mineral aerosols were the dominant source of global atmospheric phosphorus, at 82%. A more recent modeling study also concluded that 80% of atmospheric P emissions were from mineral sources (Myriokefalitakis et al., 2016).

Phosphorus deposition is commonly categorized into total phosphorus (TP) and bioavailable phosphorus. The bioavailable fraction can be readily taken up by living organisms. Ionic phosphate, or orthophosphate (PO_4^{3-}), is generally considered the most bioavailable form of P. Kanakidou et al. (2018) found that 35-45% of TP from dry deposition was from organic P species. In the Himalayas, Diao et al. (2024) found that while mineral dust was the dominant source of TP dry deposition (77% annually), bioavailable P deposition was strongly influenced by biomass burning.

Nutrient limitation, most often associated with N and/or P availability, provides an important constraint on ecosystem productivity (Vitousek et al., 2010). P limitation constrains C cycling by ecosystems and is linked to the N cycle through biogeochemical interactions (Wang et al., 2020). Excess nutrient inputs have well-documented negative impacts on ecosystem health (e.g., Baron et al., 2000; Smith et al., 1999). Burpee et al. (2022) found that P limitation impacted the sensitivity of freshwater lakes to excess N inputs. Atmospheric deposition of reactive N (N_r) and the associated ecosystem impacts are a major research focus worldwide (e.g., Driscoll et al., 2024; Walker et al., 2020). Excess reactive nitrogen deposition has well-documented adverse effects on ecosystem health, including lake eutrophication, soil acidification, and decreased biodiversity (Baron, 2006; Bobbink, 1991; Boot et al., 2016; Holtgrieve et al., 2011; Pan et al., 2021; Zhan et al., 2017). To understand the potential impacts of N_r on ecosystems, critical loads have been developed for distinct ecosystems to determine the level of N_r deposition associated with significant harmful effects. Recent research indicates that ecosystem inputs of P also lead to harmful ecosystem effects; however, significant work is needed to understand where that P comes from and at what level it is harmful (Brahney et al., 2015; Lynam et al., 2023; Tipping et al., 2014). Dry deposition of P was found to be a major source of nutrients to high-elevation lakes in the Sierra Nevada (Vicars et al., 2010). The efficiency of particle scavenging by precipitation suggests that wet deposition of soluble P species may also contribute to nutrient deposition.

In the US, the National Trends Network (NTN), a national network of wet deposition sampling, was established in 1978 by the National Atmospheric Deposition Program (NADP) to quantify acid rainfall and nutrient deposition. Precipitation samples across the US are analyzed for acidity (pH), calcium (Ca_2^+), magnesium (Mg_2^+), sodium (Na^+), potassium (K^+), sulfate (SO_4^{2-}), nitrate (NO_3^-), chloride (Cl^-), and ammonium (NH_4^+) (NADP, 2022). The NTN has been used to assess spatial and temporal trends in wet deposition of reactive N (N_r) and determine N_r inputs for sensitive ecosystems (e.g., Driscoll et al., 2003; Walker et al., 2019). Notably, the quantification of PO_4^{3-} has not been included in the network analysis of these precipitation samples.

Despite its global importance, there are relatively few studies examining P deposition, and no national network of P wet deposition measurements across the US. One challenge in measuring P wet deposition is the need for a low instrument detection limit. PO_4^{3-} can be measured by ion chromatography; however, sample concentrations are often below the instrument's detection limit. Here, we use a flow injection analysis technique that measures PO_4^{3-} by absorbance, after reagents react with it to form a blue complex. FIA is a well-established method for determining

PO_4^{3-} concentration in surface water (e.g., Lyddy-Meaney et al., 2002). However, it has not been previously used to routinely measure PO_4^{3-} in US wet deposition networks, samples from which likely have lower concentrations than observed in surface waters.

To fill this research gap, the "Sampler for Nitrogen and Phosphorus in Total" (SNiPiT) project was designed, in collaboration with NADP, the National Park Service, US EPA, and the US Forest Service, to collect precipitation samples for P analysis alongside NTN samplers. The SNiPiT samplers are pre-loaded with sulfuric acid to stop microbial activity in collected precipitation and preserve the sample for later analysis. They are attached to the exterior of NTN sampling buckets and covered by the NTN sampler lid to permit wet-only sampling. Before deploying the SNiPiT samplers and investigating the sampling collection methods, we collected precipitation samples at three sites to determine a range of expected P wet deposition concentrations and test flow injection analysis as an analytical method. We also examined potential impacts on sample analysis resulting from acidification. Daily precipitation samples were collected in Fort Collins, CO, and Mammoth Cave National Park in Kentucky. Snowpack samples were collected at two site locations in Rocky Mountain National Park.

5.2 Methods

5.2.1 Wet deposition sampling

Wet deposition samples were collected in three locations: Mammoth Cave National Park (MACA), Rocky Mountain National Park (RMNP), and Fort Collins, CO (FTCW). The sampling locations are summarized in Table 5.1. Samples of different layers of accumulated snowpack were collected in the spring in RMNP. Snowpack samples were collected in each identified snow layer using clean polyethylene bottles. Daily precipitation samples were collected at MACA and FTCW. Precipitation events were sampled in MACA and FTCW using National Consolidation (NCON) National Trends Network (NTN) sampling systems. The samples are collected in a high-density polyethylene (HDPE) bucket lined with a Low-Density Polyethylene (LDPE) sampling bag (NADP, 2021). The NCON samplers are equipped with a motor-driven lid that opens during periods of precipitation. An infra-red sensor detects water droplets falling next to the precipitation sampling bucket. The lid opens when at least 1 droplet per minute is detected and closes after a minute when no droplets are sensed (NADP, 2022). The pH of all samples was measured in triplicate using a VWR sympHony (H10P) handheld pH probe.

Table 5.1: Wet deposition sampling parameters, site elevation, and number of periods or snowpack layers sampled are given for each of the sampling locations. The two snow pit locations are labeled S1 (S2) for snow pit 1 (2) located near Nymph Lake (on the Flattop Mountain trail).

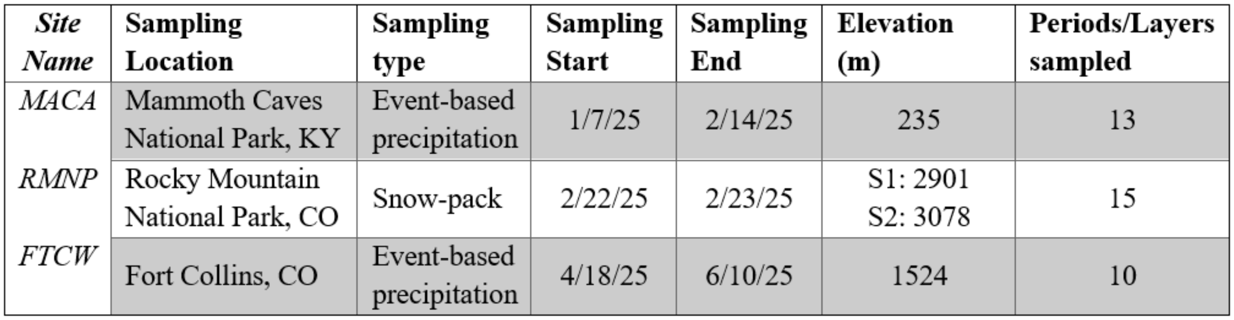

Site Name	**Sampling Location**	**Sampling type**	**Sampling Start**	**Sampling End**	**Elevation (m)**	**Periods/Layers sampled**
MACA	Mammoth Caves National Park, KY	Event-based precipitation	1/7/25	2/14/25	235	13
RMNP	Rocky Mountain National Park, CO	Snow-pack	2/22/25	2/23/25	S1: 2901 S2: 3078	15
FTCW	Fort Collins, CO	Event-based precipitation	4/18/25	6/10/25	1524	10

5.2.2 Rocky Mountain National Park, CO

In RMNP, samples were collected at different levels within the accumulated snowpack at two different sites on 2025/02/22 and 2025/02/23. During February in RMNP, daytime temperatures typically reach -2°C and overnight lows are typically -10.6°C. Precipitation is primarily snowfall, with a deep snowpack developing over the preceding winter months at higher elevations. The snow layers for sample collection were determined qualitatively based on visible differences in snow crystal transformations by Prof. David Lerach, a meteorology professor at the University of Northern Colorado, an avalanche forecaster, and a Diamond Peaks Ski Patrol member. CSU PhD student, Chloe Boehm, collected the snowpack samples. Clean polyethylene bottles were used for sample collection. A sampling bottle was used to scrape the surface-level snow to avoid contamination. Additional clean bottles were used to collect samples from each layer. The samples were kept frozen until analysis. The samples were allowed to fully thaw before analysis. For this collection method, the blank value obtained from adding deionized water to a sample bottle was equivalent to deionized water itself (0.01 μg P L^{-1}). For each snow pit, a temperature profile was generated by measuring temperature at 10 cm increments through the snowpack. Snowpack hardness was qualitatively assessed using a hand hardness test (Kinar and Pomeroy, 2015). The hand hardness test determines the snowpack hardness based on the resistance of snow layers to penetration with implements easily available to avalanche forecasters. The hand hardness test categories are described in Table 5.2. Each layer is assigned a hardness based on the largest implement that can penetrate 5 cm into the snow. Physical properties of the snowpack can be influenced by many factors, including temperature gradients within the snowpack, liquid water content, snow density, snow crystal size and shape, wind, solar radiation, and additional precipitation (Kinar and Pomeroy, 2015).

Table 5.2: The assessment categories of the hand hardness test are described, and their shortened labels are given.

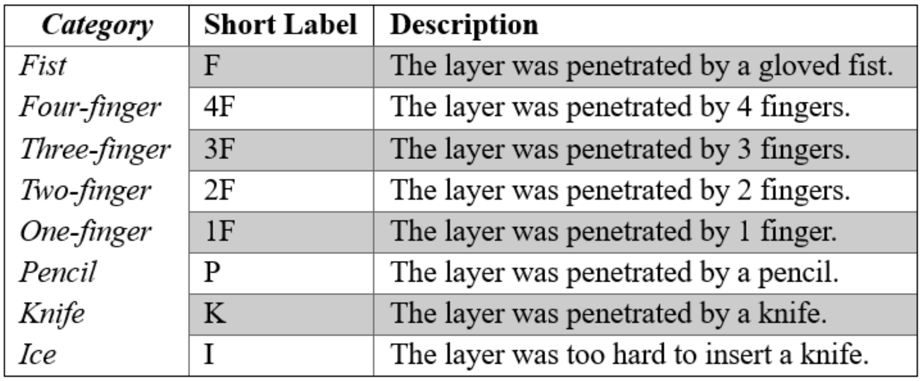

Category	**Short Label**	**Description**
Fist	F	The layer was penetrated by a gloved fist.
Four-finger	4F	The layer was penetrated by 4 fingers.
Three-finger	3F	The layer was penetrated by 3 fingers.
Two-finger	2F	The layer was penetrated by 2 fingers.
One-finger	1F	The layer was penetrated by 1 finger.
Pencil	P	The layer was penetrated by a pencil.
Knife	K	The layer was penetrated by a knife.
Ice	I	The layer was too hard to insert a knife.

The first snow pit was dug at 10:58 MST on February 22, 2025, near Nymph Lake in RMNP (40.3120°N, -105.6508°W). The site altitude was 2901 m. The snow pit was located on the northwest aspect, and the total snow depth was 142 cm. Seven snow samples were collected. This site was located 1 km from the parking area and approximately 10 m away from the Nymph Lake hiking trail, a popular winter hiking destination. The layer profile and sampling heights are shown in Table 5.3.

The second snow pit was dug at 11:15 MST on February 23, 2025, near Flattop Mountain in RMNP (40.3146°N, -105.6548°W). The site altitude was 3078 m. The total snow depth was 195

Table 5.3: The snowpack layer profile from sampling on 02/22/2025 near Nymph Lake is shown for all sampled snow layers. Hand hardness was assessed according to the hand hardness test.

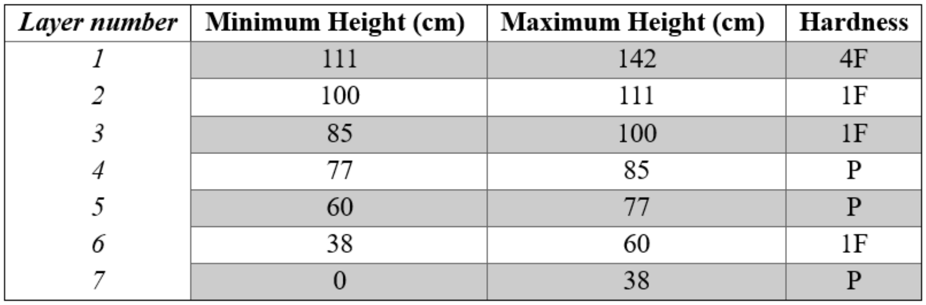

Layer number	**Minimum Height (cm)**	**Maximum Height (cm)**	**Hardness**
1	111	142	4F
2	100	111	1F
3	85	100	1F
4	77	85	P
5	60	77	P
6	38	60	1F
7	0	38	P

cm. Eight snow samples were collected. This site was 1.5 km from the parking area. The snow sampling was conducted approximately 10 m off the Flattop Mountain trail, which is not a popular winter hiking route. The layer profile and sampling heights are shown in Table 5.4.

Table 5.4: The snowpack layer profile from sampling on 02/23/2025 on the Flattop Mountain trail is shown for all sampled snow layers. Hand hardness was assessed according to the hand hardness test.

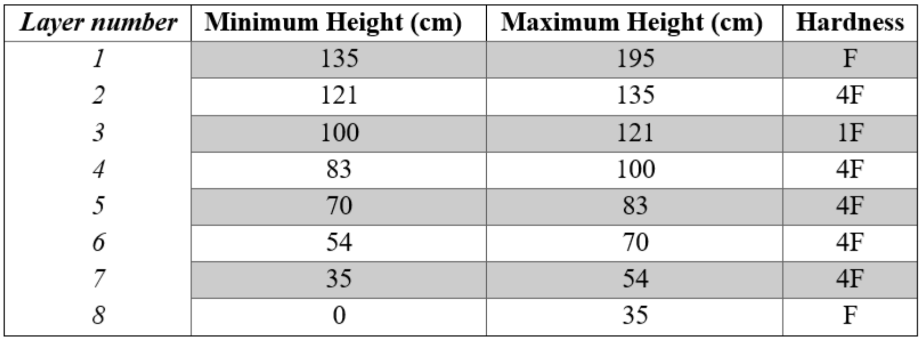

Layer number	**Minimum Height (cm)**	**Maximum Height (cm)**	**Hardness**
1	135	195	F
2	121	135	4F
3	100	121	1F
4	83	100	4F
5	70	83	4F
6	54	70	4F
7	35	54	4F
8	0	35	F

5.2.3 Mammoth Cave National Park, KY

Precipitation sampling at Mammoth Cave was conducted at the Interagency Monitoring of Protected Visual Environments (IMPROVE) network site near Houchin Meadows (37.1317667°N, -86.147856°W). The site elevation is 235 meters. Sampling at MACA was conducted from January 7, 2025, to February 14, 2025, by CSU researchers Amy Sullivan, Jihee Ban, and Taehyun Park. A sample was collected on each day with precipitation. During the study period, 13 samples were collected. During January and February, daytime temperatures typically reach around 7°C, while nighttime lows average about 1.5°C. The average total precipitation for January and February is 212 mm and includes a mix of rain and snow.

The precipitation collected was weighed at the end of each sampling period. During the study period, 2 samples had a precipitation mass that exceeded the scale limits. The samples were kept frozen and mailed to Colorado State University at a weekly frequency. The samples were stored frozen until ready for analysis. Before analysis, the samples were allowed to melt fully.

5.2.4 Fort Collins, CO

Precipitation sampling at FTCW was conducted in a wide grass field at Christman airfield (40.592309°N, -105.141528°W). The site elevation is approximately 1524 m. Sampling began on April 18, 2025, and concluded on June 16, 2025. From April to June, temperatures in Fort Collins at the Christman airfield ranged from -3.2°C to 32.4°C (CoAgMet). For this campaign, all FTCW precipitation events were rain. Duplicate samples were collected using side-by-side NCON samplers (~5 m apart) on each day with precipitation. During the sampling period, 10 precipitation events were sampled. Samples were analyzed the day after collection and then stored frozen to preserve the sample. To assess sample stability, frozen samples were compared to refrigerated samples at 1- and 2-week intervals.

The automatic opening and closure system on the NCON collection system should prevent dry deposition to the sample bag outside of precipitation periods. However, during sampling at FTCW, three samples collected were visibly contaminated: two with dirt and debris, and one with bird droppings. These samples were removed from the estimation of P wet deposition, sample stability analysis, and assessment of duplicate sampling precision. One of the samples was visibly yellow and visually striking when compared to its duplicate sample; an image of this sample pair can be found in Appendix B.

5.2.5 PO_4^{3-} flow injection analysis

All precipitation samples were analyzed for PO_4^{3-} using a Skalar SAN++ classic series automated wet chemistry analyzer. The instrument uses flow injection analysis (FIA), where a small sample volume (~1 mL) is injected into a continuous reagent stream. PO_4^{3-} in the sample reacts with the reagents to form antimony-phospho-molybdate complex, which is blue and can subsequently be measured by single-wavelength photometric analysis. This method requires two reagents: 1. An acidified complex of ammonium heptamolybdate and potassium antimony(III) oxide tartrate, and 2. Dilute ascorbic acid. The tubing where reactions occur is heated to 40°C. This method quantifies only dissolved PO_4^{3-} in the collected samples. Other forms of phosphorus, which could contribute to total phosphorus deposition, are not considered. Sample concentrations are reported in this work as μg P L^{-1}. The corresponding mass of PO_4^{3-} would be approximately three times larger.

PO_4^{3-} in samples reacts with ammonium heptamolybdate and potassium antimony(III) oxide tartrate in an acidic medium to form an antimony-phospho-molybdate complex. The resulting antimony-phospho-molybdate complex is yellow, which is then reduced by ascorbic acid and becomes blue. The absorbance of the resulting complex can then be measured with high sensitivity at 880 nm. The analysis took advantage of a long-path flow cell option in the Skalar analyzer (flow path for absorbance measurements was 50 cm) to enhance sensitivity.

This method is based on the benchtop method developed by Boltz and Mellon (1948). The Skalar SAN++ automates most of the spectrophotometric method described by Boltz and Mellon (1948), including flow controls on all reagents, an autosampler, calibration curve calculation, and an algorithm to assess the baseline drift during analysis of a sequence of samples. The SAN++ system uses peak height for sample concentration determination. During our analysis, we found an influence of sample carryover from previous samples on the response of subsequent samples. This was especially evident in low-concentration samples and standards. To avoid influence from previous samples, the time between samples or sample wash time was increased from 50 seconds to 300 seconds. This length of time eliminated carryover between samples. The sample injection time was 50 seconds.

Calibration standards and samples were run in triplicate to assess instrument precision and increase measurement confidence. Analysis was done using a 7-standard calibration curve with concentrations of: 0.5, 1, 4, 8, 12, 16, and 20 μg P L^{-1}. Calibration standards were made using potassium dihydrogen PO$_4^{3-}$. Instrument response to standards, particularly low concentration standards, was greatly reduced after 24 hours. This artifact was mitigated by diluting standards daily from a 100 mg P L^{-1} stock solution. No interference was found when standards were made with high levels of ammonium, nitrate, or other dissolved ions commonly found in precipitation samples (SO$_4^{2-}$, Cl$^-$, K$^+$). The zero point was determined by deionized water (Thermo Scientific, resistivity of 18 MΩ cm). The calibration curve response was linear across this standard range. If the calibration curve variance explained (R^2) was less than 0.998, calibration runs were repeated until a robust calibration curve was achieved. A replicate standard and a blank were analyzed after every 10 samples. A replicate of the highest standard (20 μg P L^{-1}) was analyzed at the end of every set of samples to assess and correct for instrument response drift across the sampling run. If the difference between the drift sample and the earlier standard exceeded 10%, the sampling run was removed for quality control, and the samples were re-analyzed. Figure 5.1 is an example of the calibration curve used, where standard concentration (μg P L^{-1}) is plotted against instrument response. The variance explained for this calibration curve is 0.998. The pooled relative standard deviation (RSD) of replicate standard analyses is 0.7%.

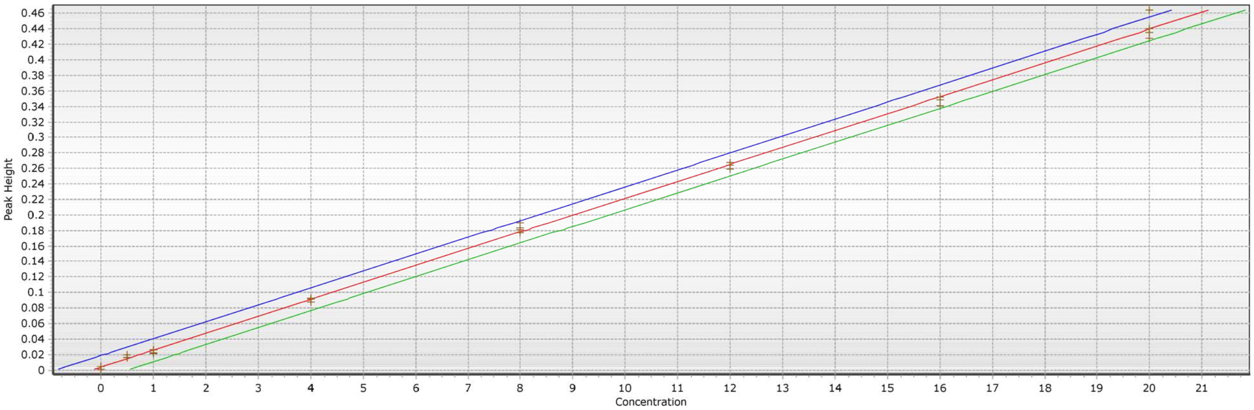

Figure 5.1: An example calibration curve is shown for FIA standards ranging from 0.5 to 20 μg P L^{-1}. Each standard was analyzed in triplicate. The best linear fit ($y = 0.0218x + 0.0038$) is red. The upper (lower) fit at the 95% confidence level is blue (green). Concentration has units of μg P L^{-1}. Peak height is reported as absorbance units (AU).

A few samples exceeded the 20 μg P L^{-1} standard. These samples were measured using a 9-standard calibration curve, which included the original standards and two higher standards: 50 and 100 μg P L^{-1}. At these higher standard values, the instrument response was no longer linear. Due to this, the calibration curve, including higher values, was fit with a second-order polynomial (see Figure 5.2). The variance explained for the example calibration curve shown in Figure 5.2 is 0.999, and pooled RSD from replicate standard analyses is 0.97%.

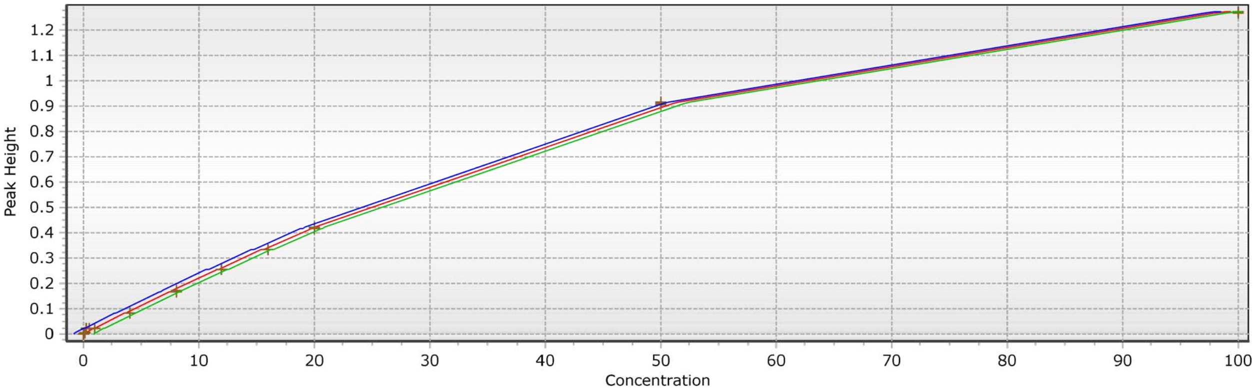

Figure 5.2: An example calibration curve is shown for FIA standards ranging from 0.5 to 100 μg P L^{-1}. Each standard was analyzed in triplicate. The best second-order fit is red. The upper (lower) fit at the 95% confidence level is blue (green). Concentration has units of μg P L^{-1}. Peak height is reported as absorbance units (AU).

The published instrument measurement range is 0.1 to 20 μg P L^{-1}. The minimum detection limit (MDL) was determined using the mean value measured for water blanks and a t-test of the instrument precision at the lowest calibration standard (0.5 μg P L^{-1}). The MDL is calculated as shown in (5.1), where $\overline{x}$ is the mean blank value, t-value (t) is assessed at the 99th percentile, and σ is the standard deviation of the lowest calibration standard replicates.

$$MDL = \overline{x} \pm t_{(n-1,99\%)}\sigma \tag{5.1}$$

The MDL was calculated using 12 replicate measurements for the blank mean and the lowest calibration standard. Using the 12 replicates for blank and calibration standards, (5.1) gives

0.01±0.08 μg P L^{-1}. Considering the largest value as our true MDL, this method has an MDL of 0.09 μg P L^{-1}. This agrees well with the published instrument range of 0.1 to 20 μg P L^{-1}.

All samples analyzed were blank corrected. The mean blank value for snowpack sampling was 0.01 μg P L^{-1} (n = 12). The mean blank value for NCON wet deposition collection in NADP bags, in FTCW and MACA, was 0.29 μg P L^{-1} (n = 6). After blank correction, only one sample from MACA was below the detection limit. All samples from RMNP and FTCW were above the detection limit.

5.2.6 Ion chromatography

All samples were analyzed for major cations and anions using Ion Chromatography. Cations and anions were analyzed on Dionex DX-500 ion chromatographs, which have isocratic pumps, self-regenerating anion or cation suppressors, and conductivity detectors. The injection volume was 50 μL, and the analysis time was 17 minutes. The IC system was used to quantify sodium (Na^+), ammonium (NH_4^+), potassium (K^+), magnesium (Mg^{2+}), and calcium (Ca^{2+}). This system uses a Dionex IonPac CS12A (3x120 mm) analytical column. The eluent was 20 mM methanesulfonic acid with a flow rate of 0.5 mL min^{-1}. An anion IC system was used to quantify chloride (Cl^-), nitrite (NO_2^-), nitrate (NO_3^-), PO_4^{3-}, and sulfate (SO_4^{2-}). This system uses an IonPac AS14A (4x150 mm) analytical column. The eluents were 1 mM sodium bicarbonate and 8 mM sodium bicarbonate at a flow rate of 1 mL min^{-1}. All ions were quantified using an 8-standard calibration curve. A standard replicate and blank sample were analyzed after every 10 samples. The limit of detection for all ions is 0.2 μg L^{-1}.

5.3 Results and discussion

5.3.1 Snowpack sampling in Rocky Mountain National Park, CO

PO_4^{3-} was measured through the snowpack in RMNP at two site locations. The first site elevation was 2901 m. The snowpack was 142 cm deep. Seven snowpack samples were taken from the established snow layers; the distribution of PO_4^{3-} concentration is shown Figure 5.3a. All samples were well above the minimum detection limit (0.09 μg P L^{-1}). PO_4^{3-} concentration ranged from 1.14 to 37.5 μg P L^{-1}. The maximum concentration occurred in the snowpack layer closest to the ground. Excluding the layer closest to the ground, the next highest PO_4^{3-} concentration was 3.90 μg P L^{-1}. In Figure 5.3b, most of the hand hardness test results give an associated layer hardness of 1-finger and pencil, indicating a firm snowpack. This may indicate a snowpack that has undergone significant physical and metamorphic changes. If the snowpack has undergone cycles of freezing and thawing, the vertical distribution of PO_4^{3-} could be influenced. This could include the leaching of PO_4^{3-} from the ground into the snowpack (Wipf et al., 2015), which could also help to explain the elevated concentration in our lowest layer. Temperature was the highest in the ground layer and generally decreased moving towards the snow surface (see Figure 5.3c).

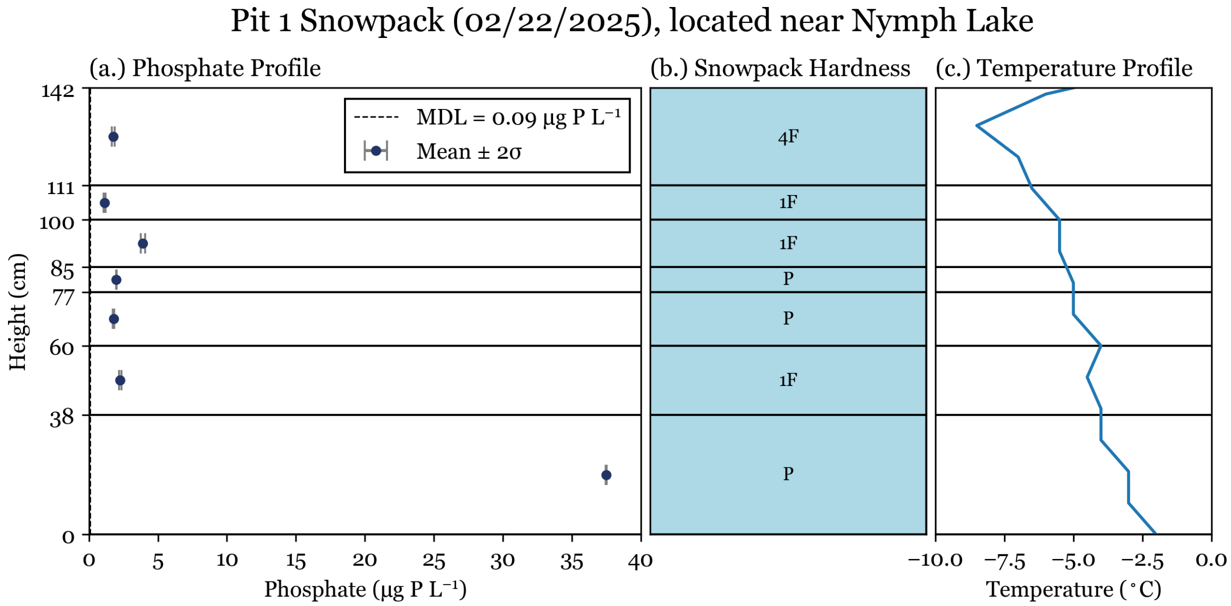

Figure 5.3: Snow pit 1, located near Nymph Lake, was sampled on February 22, 2025. 7 snow samples were collected. Snowpack profile results are shown for (a.) PO_4^{3-} concentration, (b.) snowpack hardness determined by the hand hardness test, and (c.) temperature. Error bars for PO_4^{3-} measurements are given as 2 times the standard deviation of sample replicates (n = 3).

The second snowpack sampling site was at 3078 m elevation. 500 m away from site one and 177 m higher. The snowpack at site 2 was 195 cm deep, 53 cm deeper than the snowpack at site 1, perhaps reflecting increased snowfall with elevation or differing slope aspects. While the two sites are close to each other, the complex topography of RMNP can lead to high spatial variability in precipitation. Additionally, wind can redistribute fallen snow, leading to high variability in snow accumulation across different land surface types and slope aspects.

At the second sampling site, the PO_4^{3-} concentration ranged from 0.45 to 8.22 μg P L^{-1} (Figure 5.4a). The snowpack at sampling site 2 was less firm than sampling site 1, with most layers having a fist or 4-finger hardness by the hand hardness test (see Figure 5.4b). This indicates that the snowpack has undergone fewer physical and metamorphic transformations than the snowpack at sampling site 1. The temperature profile of sampling site 2, shown in Figure 5.4c, is more variable than the profile observed at sampling site 1. Sampling site 2 also has a less pronounced temperature gradient, although the difference could be due in part to temperature differences on the two sampling days.

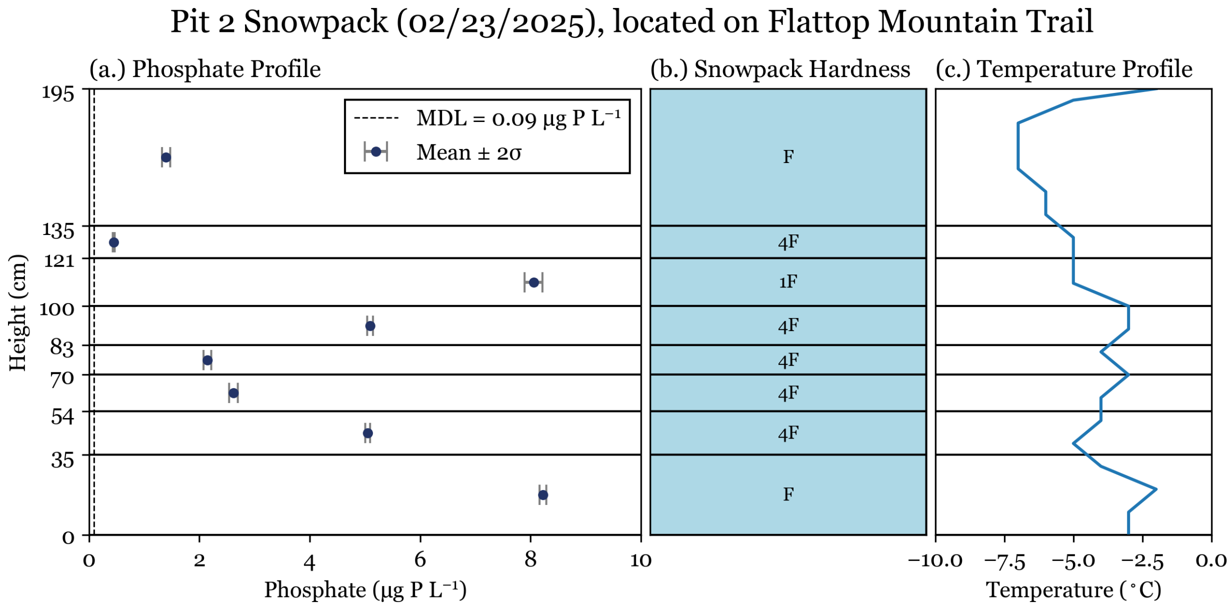

Figure 5.4: Snow pit 2, located on the Flattop Mountain Trail, was sampled on February 23, 2025. 8 snow samples were collected. Snowpack profile results are shown for (a.) PO_4^{3-} concentration, (b.) snowpack hardness determined by the hand hardness test, and (c.) temperature. Error bars for PO_4^{3-} measurements are given as 2 times the standard deviation of sample replicates (n = 3).

Overall, there is a larger range of PO_4^{3-} concentrations observed in snow pit 1. However, if the largest value from sampling site 1 (layer closest to the ground) is excluded, sampling site 2 has a larger range of PO_4^{3-} concentration. The snowpack observed at sampling site 2 was deeper and may have undergone less transformation since the precipitation fell. This could be due to its higher elevation, differences in exposure to solar radiation, or other factors.

Figure 5.5 shows the relationship between measured PO_4^{3-} concentration and ion species measured using ion chromatography. The plots are arranged in order by the strength of correlation. The snowpack PO_4^{3-} concentrations are most strongly correlated with potassium ($R^2 = 0.9$). Potassium is an abundant nutrient in soil, which could indicate local dust deposition or nutrient leaching into the snowpack from the surface. Notably, K^+ is highest in the sample, which may also have PO_4^{3-} leaching from the soil. PO_4^{3-} is also well correlated with Cl^-, NH_4^+, and Na^+.

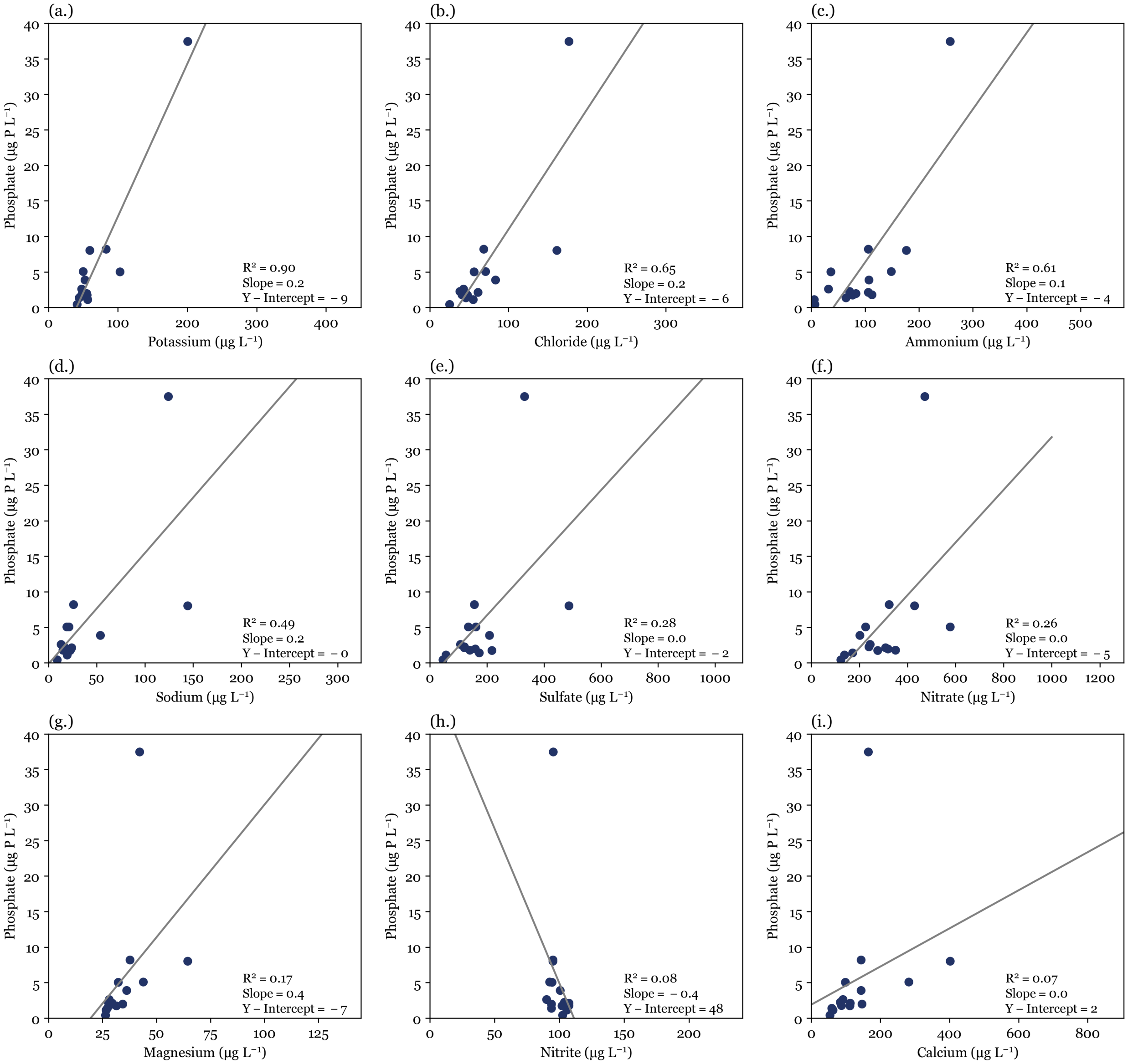

Figure 5.5: Correlations between PO_4^{3-} concentration and ionic concentration are shown for (a.) Ca_2^+, (b.) NO_2^-, (c.) Mg_2^+, (d.) NO_3^-, (e.) Cl^-, (f.) Na^+, (g.) K^+, (h.) SO_4^{2-}, and (i.) NH_4^+. The optimized least squares linear regression is displayed in grey for each plot, and the fit details are listed in the lower right corner.

5.3.2 PO_4^{3-} wet deposition sampling in Mammoth Cave National Park, KY

Wet deposition at MACA was collected for each daily precipitation event between January 7, 2025, and February 14, 2025. During that period, 13 precipitation samples were collected and subsequently analyzed for PO_4^{3-} wet deposition. Figure 5.6 shows the measured PO_4^{3-} concentration from all collected samples at MACA. The sample collected on February 9, 2025, was below the instrument detection limit. PO_4^{3-} concentrations above the detection limit ranged from 0.21 to 8.74 μg P L^{-1}. The highest PO_4^{3-} concentration precipitation events occurred in the second half of the sampling. The sample collected on January 18, 2025, was snow. All other samples were either rain or mixed precipitation. The liquid water collected for each precipitation event was highly variable, ranging from 113 mL to 1.6 L. Two periods, 2025/01/08 and 2025/01/23, are missing data for precipitation amount. The first sample precipitation amount was recorded improperly. The second sample with a missing precipitation amount, 2025/01/23, exceeded the scale limits used to measure precipitation mass and was therefore greater than 1.6 L. Precipitation amount only explained 12% of the variance in PO_4^{3-} wet deposition concentration ($R^2 = 0.12$) for this data set.

Wet deposition samples from MACA were analyzed for relationships between PO_4^{3-} and other ions (Figure 5.7). At MACA, PO_4^{3-} is not well correlated with any measure ion species. This may reflect differing source contributions driving concentrations of PO_4^{3-} vs. other ion species. The highest PO_4^{3-} concentration has a low corresponding concentration of all other ion species. This sample in particular may have a different source of PO_4^{3-} than the other samples collected.

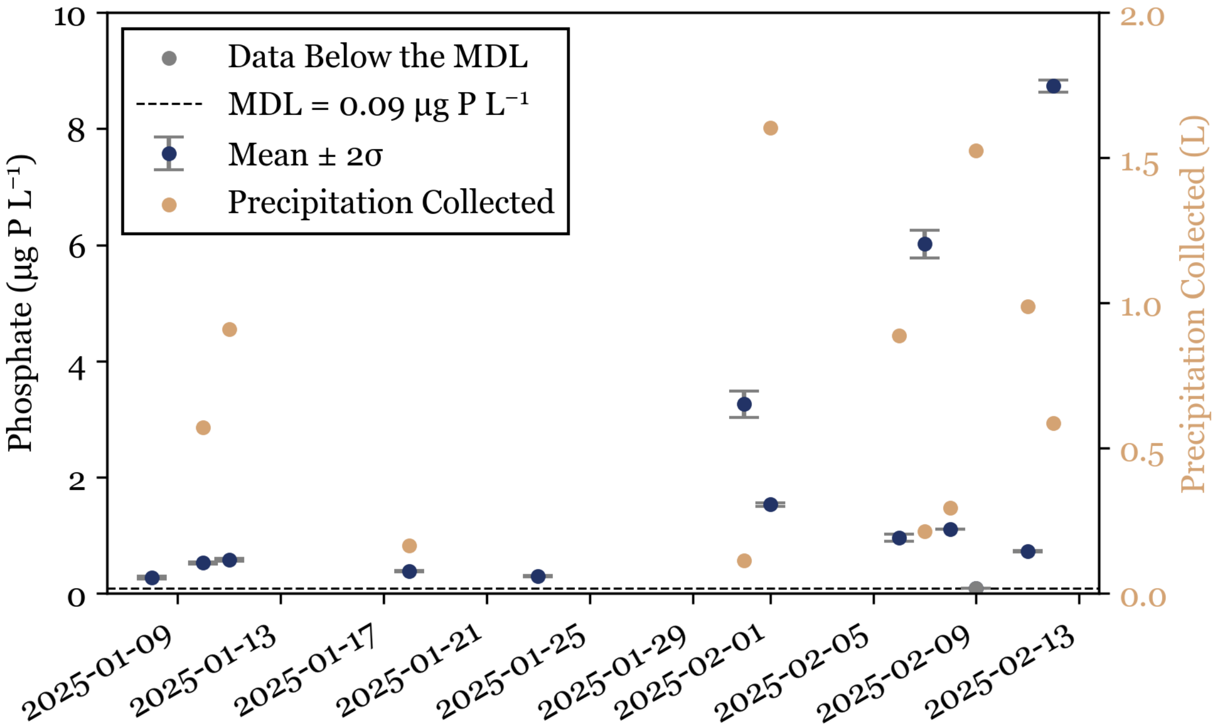

Figure 5.6: PO_4^{3-} wet deposition collected in Mammoth Cave National Park (MACA). Error bars for PO_4^{3-} measurements are given as 2 times the standard deviation of sample replicates (n = 3). Total precipitation collected for each sample is given on the right-hand axis. PO_4^{3-} measurements below the MDL are grey.

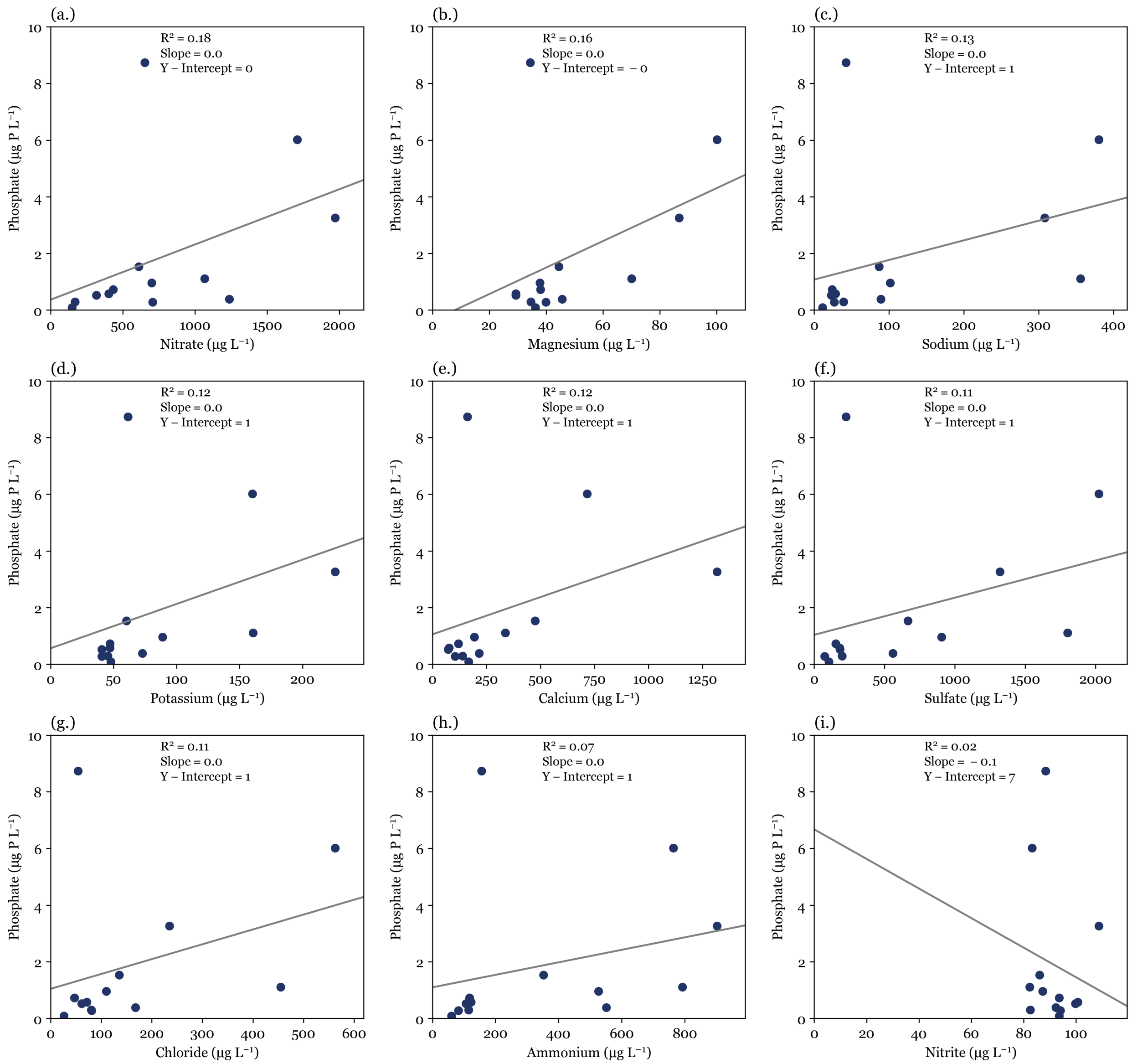

Figure 5.7: Correlations between PO_4^{3-} concentration and ionic concentration are shown for (a.) Ca_2^+, (b.) NO_2^-, (c.) Mg_2^+, (d.) NO_3^-, (e.) Cl^-, (f.) Na^+, (g.) K^+, (h.) SO_4^{2-}, and (i.) NH_4^+. The optimized least squares linear regression is displayed in grey for each plot, and the fit details are listed in the lower right corner.

5.3.3 PO_4^{3-} wet deposition sampling in Fort Collins, CO

Wet deposition samples were collected during precipitation events in Fort Collins, CO (FTCW) beginning on April 18, 2025, and finishing on June 10, 2025. During this time, 10 precipitation events were sampled. FTCW samples were collected in duplicate. The mean value for each precipitation event is shown in Figure 5.8. All precipitation collected was rainfall. The volume of precipitation collected was highly variable, ranging from 72 mL to 1.7 L. Only 7% of the variability in PO_4^{3-} concentration was explained by precipitation amount ($R^2 = 0.07$). PO_4^{3-} wet deposition concentrations ranged from 1.71 to 18.7 μg P L^{-1} excluding three samples eliminated due to obvious contamination with soil or bird feces (see earlier discussion).

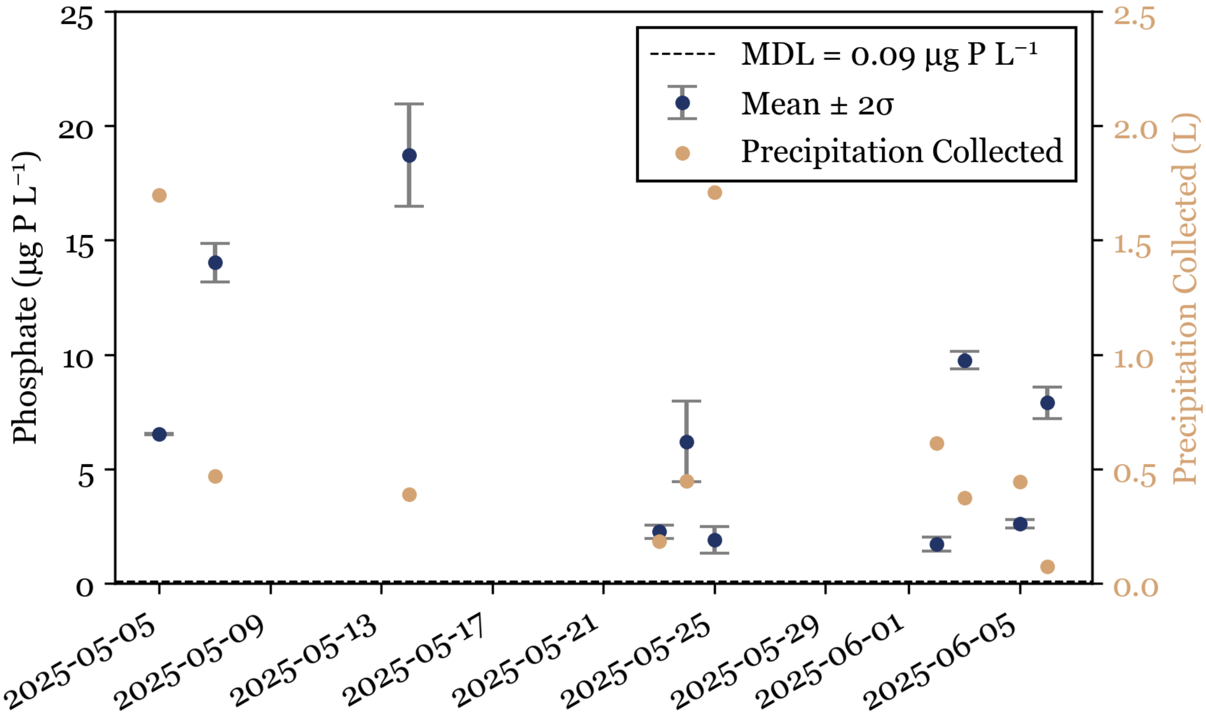

Figure 5.8: PO_4^{3-} wet deposition collected at FTCW. Error bars for PO_4^{3-} measurements are given as 2 times the standard deviation of sample replicates (n = 3) and collocated samples where available. Total precipitation collected for each sample is given on the right-hand axis.

The error bars in Figure 5.8 were generated using 2 times the standard deviation of duplicate measurements, including sample replicates on the instrument. The pooled relative standard deviation across all sampling periods was 7%. These errors are larger than those reported for PO_4^{3-} concentrations in RMNP or MACA. Despite that, no measurements are below the instrument detection limit.

Figure 5.9 compares wet deposition PO_4^{3-} concentration and ion species concentration collected at FTCW. PO_4^{3-} wet deposition is well correlated with Ca_2^+ ($R^2 = 0.86$), see Figure 5.9a.

The plots in Fig. 9 are ordered by the variance explained by each linear fit. The next best correlation is NO_2^- (R^2 = 0.46), followed closely by Mg_2^+ (Figure 5.9c), through SO_4^{2-} (Figure 5.9h), which explains between 30 and 15 percent of the variance in PO_4^{3-} concentration. Ammonium is not correlated with PO_4^{3-} in the wet deposition samples (Figure 5.9i). The strength of correlation between Ca_2^+ and PO_4^{3-} indicates that they may share a source in wet deposition.

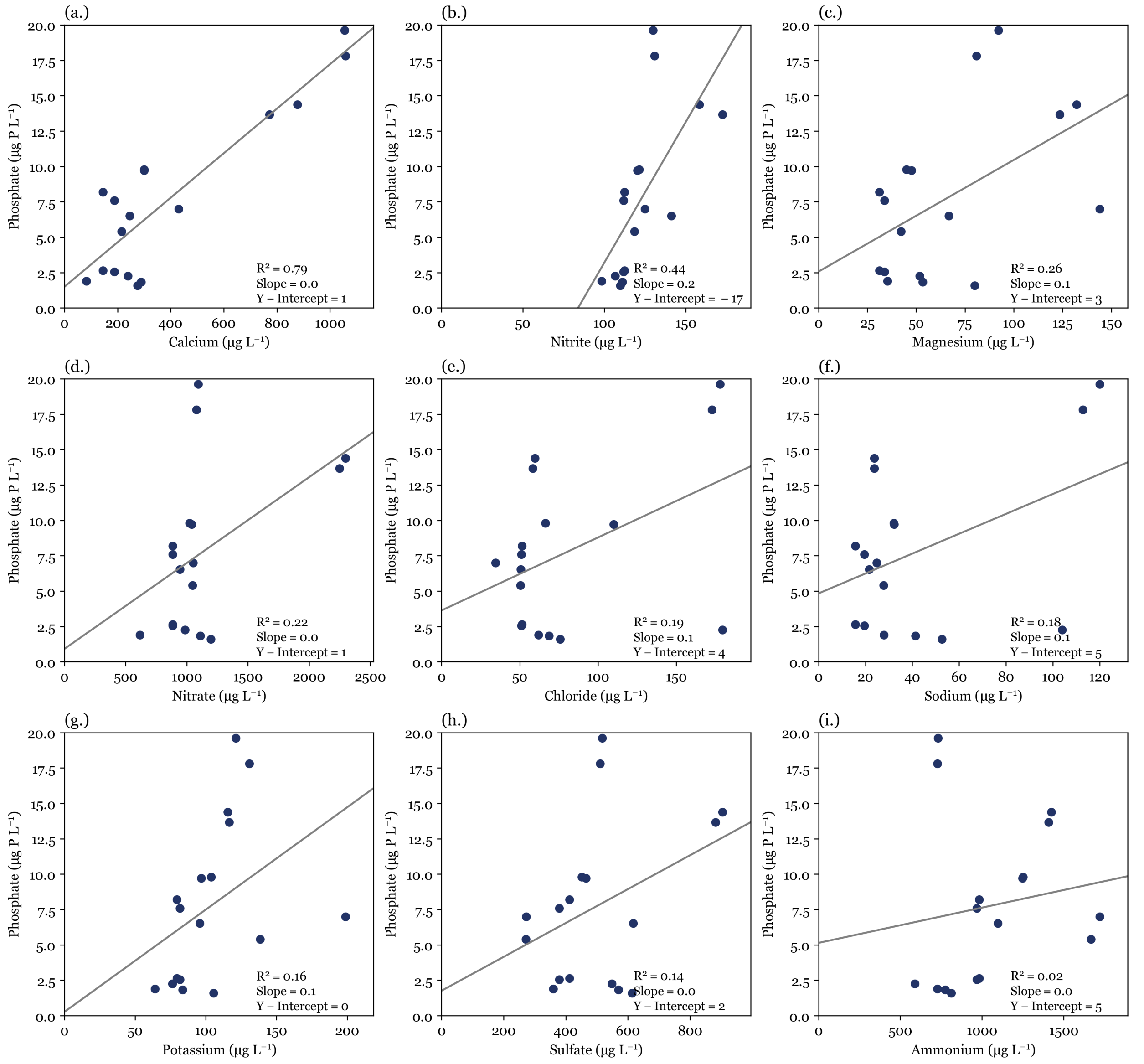

Figure 5.9: Correlations between PO_4^{3-} concentration and ionic concentration are shown for (a.) Ca_2^+, (b.) NO_2^-, (c.) Mg_2^+, (d.) NO_3^-, (e.) Cl^-, (f.) Na^+, (g.) K^+, (h.) SO_4^{2-}, and (i.) NH_4^+. The optimized least squares linear regression is displayed in grey for each plot, and the fit details are listed in the lower right corner.

Sea spray aerosol (Su et al., 2023), wildfires (Yokelson et al., 2009), and mineral dust (Sequeira, 1993) are the dominant sources of Ca_2^+ aerosol, with mineral dust likely most important at the FTCW location for the measured period. Mahowald et al. (2008) used Ca_2^+ and other elements prevalent in the Earth's crust (iron, aluminum, and silicon) to identify P deposition correlated with mineral dust. During the period of sampling at FTCW, there were no wildfires within Colorado or the neighboring states. Brahney et al. (2013) found that Ca_2^+ wet deposition is increasing in the western US and attributed this increase to soil aerosol and dust emissions. The lack of a strong correlation between Cl^- and PO_4^{3-} indicates that sea spray aerosol is an unlikely source of PO_4^{3-}, not surprising given the large distance from the ocean.

During precipitation sampling at FTCW, 3 samples were visibly contaminated by dirt and debris. In the most extreme case, the collected precipitation was yellow. Photos of the contaminated samples can be found in Appendix B. Figure 5.10 displays all PO_4^{3-} concentration data from each NCON sampler, referred to as samplers 1 and 2. The three contaminated samples are marked with grey shading on the collection date and occurred on: 2025/05/05, 2025/23/05, and 2025/25/05. The mean difference between co-located samples for these three days was 62.9 μg P L^{-1}. The mean difference between co-located samples for all other days was 0.7 μg P L^{-1}.

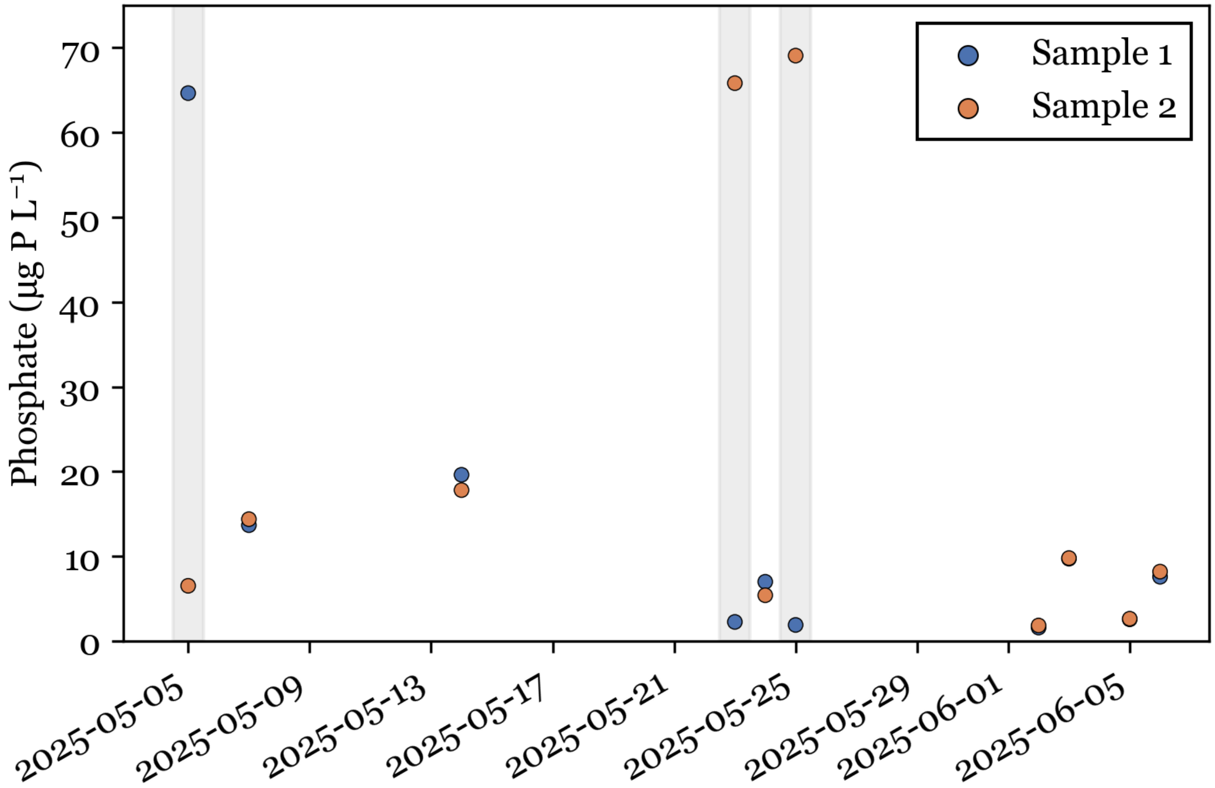

Figure 5.10: Duplicate PO_4^{3-} wet deposition samples collected in Fort Collins, CO (FTCW). Samples are given as the instrument replicate means (n = 3). The dates with a sample tagged as contaminated have been shaded grey.

The ion composition of the contaminated samples is compared with the distribution of ion composition for the uncontaminated samples in Figure 5.11. The contaminated samples on 2025/05/05 and 2025/05/25 have similar ion concentrations for all species except Na^+. The contaminated sample on 2025/05/23 is elevated compared to the other two samples for all species besides NO_3^-. The contaminated sample on 2025/05/23 also has an ion concentration outside of the range of the uncontaminated samples for all species besides NO_3^-. This sample was a distinct color (yellow) compared to its corresponding duplicate sample (see Appendix B). The other samples (2025/05/05 and 2025/05/25) had elevated concentrations of Mg_2^+, Cl^-, K^+, and SO_4^{2-}. The lack of elevated Ca_2^+ indicates that the source of this contamination is likely not soil, contradicting the visual observation of debris in contaminated samples.

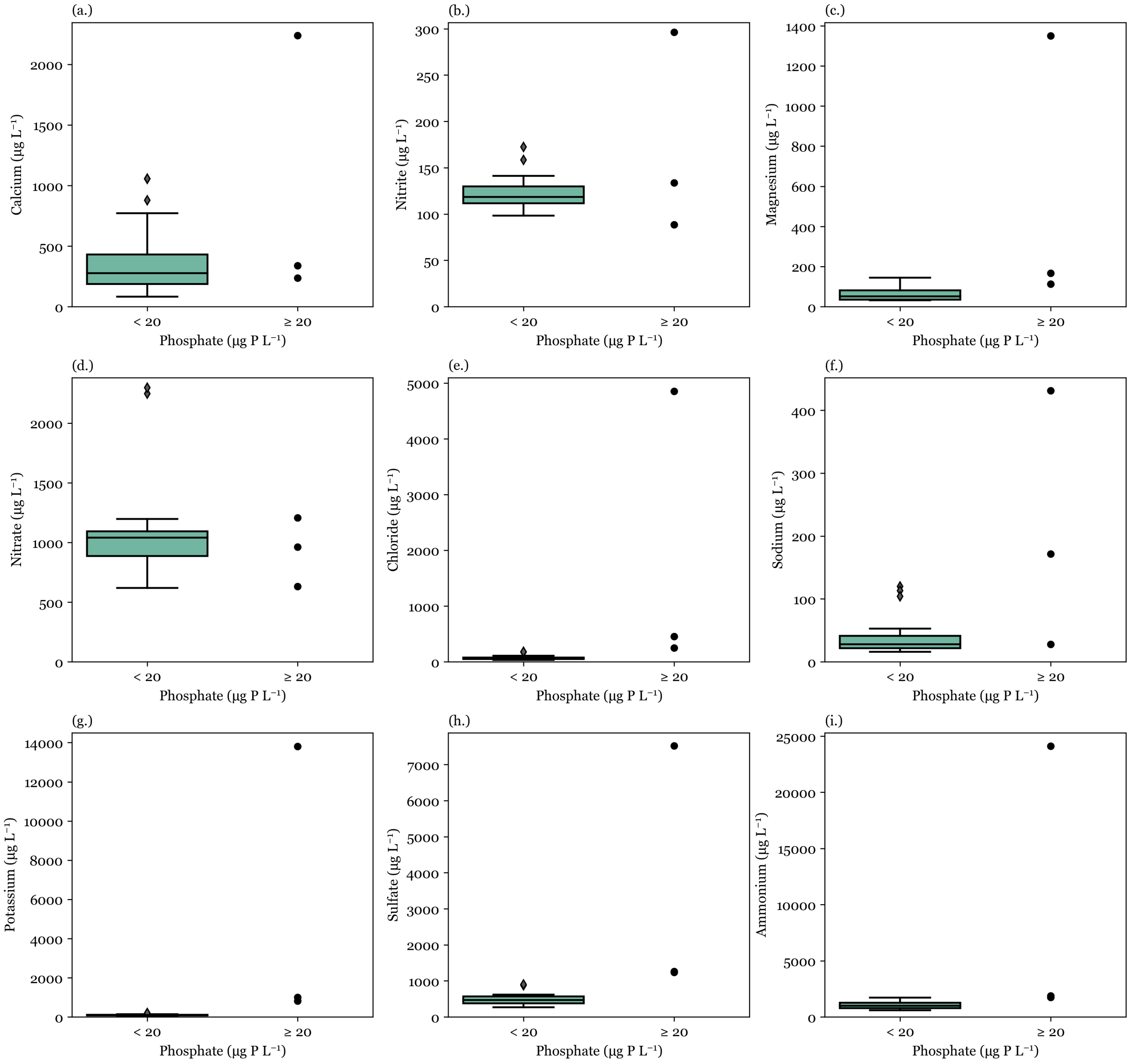

Figure 5.11: PO_4^{3-} concentrations are compared to ionic concentrations for (a.) Ca_2^+, (b.) NO_2^-, (c.) Mg_2^+, (d.) NO_3^-, (e.) Cl^-, (f.) Na^+, (g.) K^+, (h.) SO_4^{2-}, and (i.) NH_4^+. Data are sorted into two categories: 1. $[PO_4^{3-}] < 20\ \mu g\ P\ L^{-1}$ and 2. $[PO_4^{3-}] \geq 20\ \mu g\ P\ L^{-1}$. The plotting parameters are as follows: 1. A boxplot of values, where the median is a flat line, box extent shows the interquartile range (IQR), whiskers are 1.5 times the IQR, and outliers are diamonds, and 2. A point for each value.

5.3.4 Inter-site comparison of PO_4^{3-} wet deposition

To probe the variability between site location and precipitation type, the PO_4^{3-} wet deposition results are compared across all study locations (see Figure 5.12). Only one measurement, from MACA, was below our instrument detection limit; the value is included here as MDL/2. The largest range and median PO_4^{3-} concentrations were observed in FTCW. The largest value reported, 37.5 μg P L^{-1}, occurred in the lowest layer of snow sampling at RMNP S1. The lowest median value occurred at MACA, 0.72 μg P L^{-1}. These differences could be due to regional, precipitation type, seasonal, or specific event sampling differences. Excluding the lowest layer sampled at RMNP S1, PO_4^{3-} quantified in wet deposition ranged from 0.21 to 18.7 μg P L^{-1}.

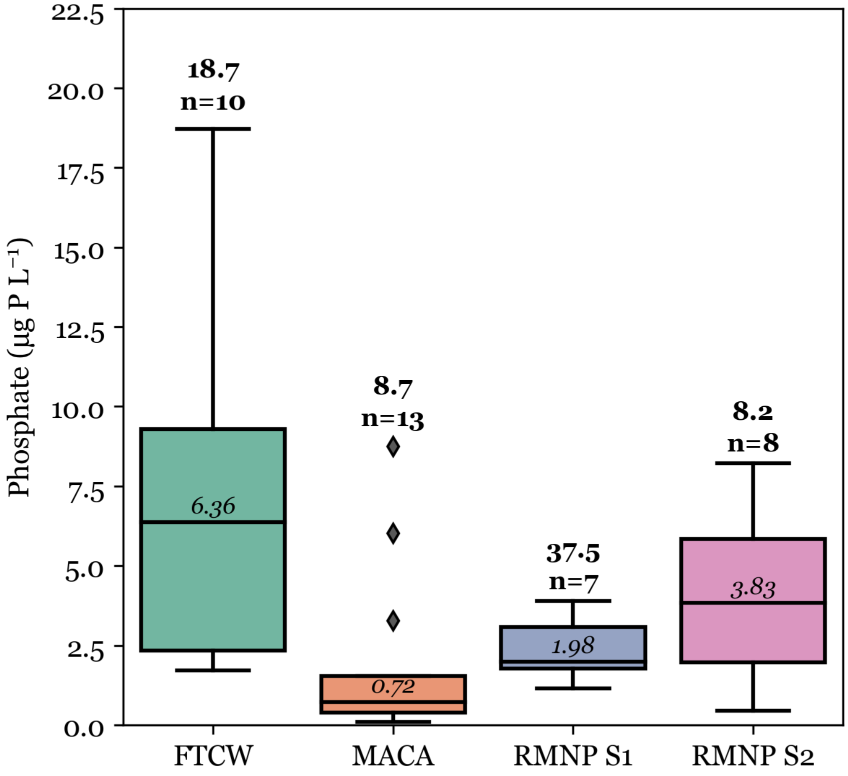

Figure 5.12: PO_4^{3-} data from all sites are shown. The two snow pit sites in RMNP are shown separately. S1 (S2) is the site located at Nymph Lake (on the Flattop Mountain trail). The median is a flat line, the box extent shows the IQR, the whiskers are 1.5 times the IQR, and outliers are diamonds. The number of samples and maximum value are listed above each box. The median value is given above the median line. The median and maximum are listed with units of μg P L^{-1}.

5.3.5 Sample stability and acidification effects on instrument response

Samples collected in Fort Collins were used to assess the stability of PO_4^{3-} concentration in wet deposition. Each sample was analyzed the day after collection and then divided into frozen and refrigerated samples. The frozen samples were used as a control in subsequent measurements. The samples were analyzed again after 1 and 2 weeks of storage. After one week of storage in a refrigerator, sample concentration decreased by an average of 13%. Following an additional week of refrigerated storage, sample concentration was, on average, 16% lower than the original. Samples that had been stored frozen differed from the original concentration by less than 5% after 1 and 2 weeks of storage.

A new class of proposed samplers will be pre-treated with sulfuric acid to prevent microbial activity. Lowering the pH of wet deposition samples may alter the instrument response. Three standards (1, 8, and 20 μg P L^{-1}) from the typical calibration curve were used to assess the effect of acidification on measured PO_4^{3-} concentration (see Figure 5.13). Standards were acidified using 1M H_2SO_4, and the resulting pH was volume corrected. The highest standard, 20 μg P L^{-1}, differed from the initial standard concentration by <5% for all acidification steps. The middle standard, 8 μg P L^{-1}, differed from the initial standard by <5% when the pH was >1.2, but instrument response increased rapidly below 1.2. At the lowest pH tested, 0.83, the response was 25% larger than the initial concentration. The lowest concentration tested, 1 μg P L^{-1}, had the largest percent difference as would be expected. The response when standards were acidified to pHs >1.2 was within 15% of the initial standard response. At a pH of 0.83, the lowest standard instrument response increased by >300%. The minimum pH of wet deposition samples from pre-treated samplers is expected to be ~1.2; however, this will depend on the initial pH of the rainfall. Before the installation of pre-treated samplers, these effects and options to mitigate this response should be assessed.

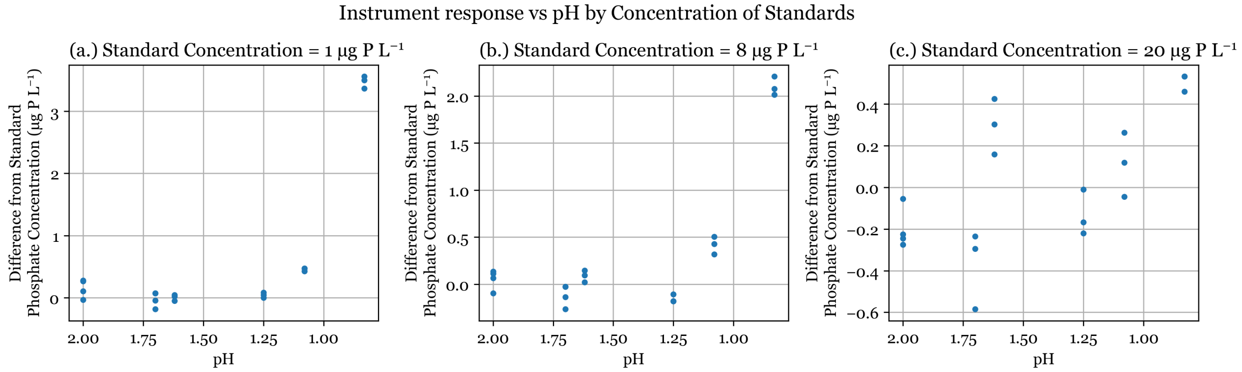

Figure 5.13: The effects of pH on measured standard concentration are assessed for (a.) Standard 3: 1 μg P L^{-1}, (b.) Standard 5: 8 μg P L^{-1}, and (c.) Standard 7: 20 μg P L^{-1}.

5.4 Summary

PO_4^{3-} concentration was measured using flow injection analysis in snowpack layers at Rocky Mountain National Park and daily precipitation samples collected at Fort Collins, CO, and Mammoth Cave National Park. Snowpack sample concentrations from Rocky Mountain National Park ranged from 0.45 to 37.5 μg P L^{-1}. The highest PO_4^{3-} concentration was found in the lowest layer of snow pit 1. This elevated level could result from P leaching from the soil, which has been observed in snow that has experienced freeze/thaw cycles (Wipf et al., 2015). Increased hardness at lower layers indicated that this snowpack had undergone more physical and metamorphic changes than snow pit 2. The second snow pit had a maximum P concentration of 8.22 μg P L^{-1}, also in the layer closest to the ground. Active precipitation events at Mammoth Cave National Park during winter ranged from 0.21 to 8.74 μg P L^{-1}. One precipitation sample at MACA was below the instrument detection limit. Daily precipitation concentrations in Fort Collins, CO, during spring and summer ranged from 1.71 to 18.7 μg P L^{-1}.

The ion composition of precipitation was also analyzed in collected samples. Most notably, PO_4^{3-} was well correlated with calcium at Fort Collins, indicating mineral dust aerosol could be a dominant source of measured P wet deposition at that location and time spring/summer time period. MACA samples did not reveal an overall strong correlation between concentrations of PO_4^{3-} and Ca_2^+, suggesting they might reflect a more variable mix of PO_4^{3-} source contributions. Precipitation events in Fort Collins, CO, were quantified with duplicate, co-located samplers. Three of the duplicate samples were flagged for dirt and debris. These samples differed from their co-located pair by 62.9 μg P L^{-1}. The mean difference between all other co-located samples was 0.7 μg P L^{-1}. The contaminated samples had a different relative ion composition, indicating a different source of P. These unexpectedly large differences indicate a further need for co-located PO_4^{3-} monitoring to better constrain measurement uncertainties.

Comparing results across different sampling locations, the highest median P wet deposition concentration was found in Fort Collins, CO, at 6.36 μg P L^{-1}. The lowest median P wet deposition concentration occurred at Mammoth Cave National Park, at 0.72 μg P L^{-1}.

5.5 Future research

The results presented here demonstrate that P wet deposition can be quantified using the described flow injection analysis method and provide insight into the range of expected concentrations. Future research should evaluate the spatial and seasonal variability in P wet deposition, including additional sites with various potential sources and seasonal changes.

Samples for this study were collected following National Trends Network standard procedures. Future collection of P wet deposition is planned using alternative samplers, known as SNiPiT samplers. A key difference is that SNiPiT samples are pre-treated with acid to prevent microbial activity. In our analysis of sample stability, concentration decreased by greater than 10% after a week of refrigeration. The NADP NTN network collects samples weekly, which could lead to lower PO_4^{3-} observations. One proposed solution is to add sulfuric acid to the collection bottle to stop biological activity. Sample pH began to affect measured PO_4^{3-} concentration as early as pH 1.2. Future assessment of the observed pH with the acid treatment should include acidification effects, stability of acidified samples, and probe the acid amount needed to prevent microbial activity.

To assess this new sampling method and improve understanding of P wet deposition, we will collect weekly and event-based samples in Fort Collins, CO, over three months. This work has been delayed at present due to unsatisfactory blank levels identified in PVC SNiPiT samplers provided by the NADP program office. Once blank issues are resolved, field samples will be duplicated, using both the standard NTN method and SNiPiT samplers. The data will help evaluate sample stability, compare collection techniques, and determine the precision of SNIPIT samplers. The goal of this campaign is to gather insights into P wet deposition data collection and support the potential implementation of P wet deposition measurements across the NTN Network.

Chapter 6

Conclusions and Recommendations for Future Work

This work investigated the current and potential deposition of nutrients to remote ecosystems. Excess reactive nitrogen deposition has well-documented negative effects on ecosystem health and has been heavily researched in recent years. Although there are many measurements of reactive nitrogen wet deposition, dry deposition processes, especially of NH_3, are seldom characterized experimentally and poorly parameterized in models. NH_3 dry deposition was simulated using a bidirectional exchange model, with a variety of measured and modeled inputs to investigate model sensitivity to input data characteristics, including time resolution, and improve understanding of how to best treat bidirectional exchange of NH_3 in chemical transport models. Relative contributions of reduced inorganic nitrogen (NH_x = NH_3 + NH_4^+) to total reactive nitrogen deposition are growing due to increased NH_3 emissions along with decreasing NO_x emissions.

Increasing NH_3 emissions are also of interest because of the key role NH_3 plays in submicron particle formation. Slow dry deposition rates of these particles mean that NH_x can be transported farther from source regions, leading to increased haze and human health impacts. Trends in atmospheric NH_3 concentrations and contributions from different emission sectors, including agriculture and wildfires, were evaluated: first using *in situ* and satellite observations in northeast Colorado, a complex NH_3 source region, and then more broadly across the western US using satellite data.

Deposition of reactive phosphorus, including PO_4^{3-}, is an emerging concern for ecosystem health. PO_4^{3-} wet deposition has not been routinely monitored, in part due to measurement difficulties. In this work, a high-sensitivity measurement technique was evaluated for PO_4^{3-} wet deposition, and pilot results are reported from wet deposition at three sites.

6.1 Conclusions

Sensitivity of Simulated Ammonia Fluxes in Rocky Mountain National Park to Measurement Time Resolution and Meteorological Inputs

Rocky Mountain National Park has experienced well-documented negative ecosystem impacts from excess reactive nitrogen deposition (Baron, 2006; Boot et al., 2016). In recent years, reduced nitrogen species have dominated total N deposition in Rocky Mountain National Park (Benedict et al., 2013; Benedict et al., 2018). Dry deposition of NH_3 has large uncertainties (Walker et al., 2019b). A year of NH_3 fluxes was simulated using a bidirectional NH_3 flux model to estimate emission and deposition to a forest ecosystem on the east side of Rocky Mountain National Park.

NH_3 bidirectional exchange is highly variable in both sign and magnitude. High time-resolution NH_3 concentrations and micrometeorological data are needed to support accurate flux estimates. Cost and complexity limit the availability of high time-resolution NH_3 measurements. Low-cost two-week passive NH_3 measurements offer an appealing alternative and are already implemented in the NADP AMoN network. Bidirectional RMNP NH_3 fluxes were biased low, however, when biweekly NH_3 concentration data were substituted for high time-resolution measurements. This low bias was correctable by either (1) applying a constant correction factor or (2) interpolating biweekly data to 30-minute frequency using a mean diel NH_3 concentration pattern.

Local micrometeorology is also costly to measure. At Rocky Mountain National Park, the use of reanalysis data for flux simulations resulted in a factor of two increase to annual net NH_3 deposition. Again, this bias could be addressed using a simple correction factor, but this factor likely differs across land surface types and different regions. Further, the ERA5 reanalysis data set used here has 25 km grid cells, which can encompass a variety of surface types and parameters.

Ammonia in Northeast Colorado is Increasing, Rising Most Quickly in Regions Close to Confined Animal Feeding Operations

Emissions of NH_3 near Rocky Mountain National Park come predominantly from nearby agricultural development, urban sources, and wildfire smoke. Ground-based NH_3 measurements and

IASI satellite retrievals were used to assess the spatial and temporal variability of NH_3 concentrations in NE Colorado, an important source region. NH_3 had a strong seasonal cycle and spatial gradient in both datasets.

The permitted animal capacity of CAFOs within 12 km of surface monitoring sites (IASI grid cells) explained 78% (50%) of the variability in summertime mean NH_3 mixing ratios. This indicates the importance of agricultural emissions in governing variability in NH_3 concentrations across the region. Excluding a site within 1 km of the largest CAFO in Colorado, surface-level and satellite total column NH_3 retrievals were well correlated ($R^2 = 0.42$). IASI satellite retrievals of total column NH_3 concentration revealed a strong increasing NH_3 trend in both agricultural (2.6% yr^{-1}) and urban (1.7% yr^{-1}) source regions during the 2013-2023 study period.

Various factors were considered as possible contributors to increasing NH_3 in the region. Decreased particle formation, expected from decreased SO_2 emissions, explained less than 5% of the observed NH_3 increases. A clear wildfire smoke signal was observed by IASI over NE Colorado, especially during the Cameron Peak Fire in 2020. The frequency of wildfire smoke plumes over the region was found to be increasing by approximately 3 days per year. Smoke increases were similar above agricultural and urban source regions, suggesting that contributions from wildfire smoke cannot account for observed NH_3 concentration increases over the agricultural source region. When NH_3 column concentration trends were computed at IASI grid cell resolution, the magnitude of the trend revealed a spatial pattern similar to the spatial distribution of CAFOs, suggesting that changes in agricultural emissions are an important factor.

These results indicate that NH_3 concentration increases over NE Colorado are associated with agricultural regions. Increasing NH_3 could be attributed to changes in agricultural practices, output, or changing climatology. In NE Colorado, climate change has increased temperatures, which could contribute to increased NH_3 emissions, even given the same agricultural activity.

Contributions of Wildfire Smoke and Agricultural Emissions to Changing Ammonia across the Western US

The western US is home to agricultural developments, frequent wildfire smoke, and high-alpine ecosystems, sensitive to excess reactive nitrogen inputs. Changes to NH_3 concentrations and the spatial footprint of NH_3 hotspot areas were assessed across the region using IASI and CrIS satellite NH_3 data. Warm season NH_3 total column concentrations had a similar spatial pattern between IASI and CrIS satellite retrievals, although CrIS total column concentrations were typically higher. Monthly IASI data were used to assess the seasonality of increasing NH_3 concentrations, with the largest increase observed during the warm season. CrIS oversampled data were generated for the warm season across the years 2013-2023, and is expected to capture the largest inter-annual trends.

The CrIS oversampled dataset was used to determine NH_3 hotspot regions across the western US. Key locations included: NE Colorado and a zone from the Texas panhandle north to western Nebraska (important beef production regions), along with the Snake River Valley of Idaho and the San Joaquin Valley of California (important dairy and crop production regions). The largest increasing NH_3 concentration trends occurred above agricultural hotspot regions, ranging from 1.5 to 4.8% per year. In northeast Colorado, removing thick smoke plumes reduced the total column NH_3 trend in hotspot regions from 2.7 to 2.5% per year. In the Snake River Valley, the NH_3 trend (1.5% yr^{-1}) did not change when wildfire smoke was removed. Wildfire smoke had a larger relative impact on NH_3 trends in remote regions, where concentrations of NH_3 are typically low, and in some regions, where smoke is more frequent.

The spatial footprint of agricultural hotspots across the western US was found to be increasing by an average of 7% per year, falling to 6% per year when thick wildfire smoke is removed. Northeast Colorado had the largest increase in NH_3 hotspot area (15% yr^{-1}) and the largest impact from thick smoke (falling to 12% yr^{-1} when thick smoke was removed). Growth of NH_3 hotspot areas could indicate an increasing rate of agricultural NH_3 emissions in these regions, an increasing footprint of agricultural activities in a region, and/or an increasing atmospheric lifetime of NH_3. Larger footprints can increase the likelihood of NH_3 transport to nearby sensitive ecosystems and increase the potential of particle formation through NH_3 interactions with NO_x plumes from other sources.

Novel Quantification of Phosphate Wet Deposition Using Flow Injection Analysis

Excess phosphorus deposition to remote ecosystems is an emerging concern for ecosystem health (e.g., Brahney et al., 2015; Burpee et al., 2022; Tipping et al., 2014; Vitousek et al., 2010). Phosphate has not been previously quantified in US national networks due to uncertainty regarding appropriate sampling methods and difficulty measuring low phosphate concentrations expected in wet deposition, especially at remote locations. A flow injection analysis method was tested and implemented to quantify phosphate concentrations in wet deposition samples from three sites: (1) daily precipitation collections in Fort Collins, Colorado, (2) daily precipitation collections in Mammoth Cave National Park, Kentucky, and (3) two sets of snowpack samples from Rocky Mountain National Park.

Flow injection analysis, previously used for surface water measurements of phosphate, relies on a color-changing reaction measured by visible absorption. The limit of detection for this method, as implemented in our laboratory, using a long-path absorbance detector cell, is 0.09 μg P L^{-1}. Blank tests of NADP wet deposition sampling bags revealed concentration levels of 0.3 μg P L^{-1}. In daily precipitation samples, phosphate ranged from 0.21 to 18.7 μg P L^{-1}, with one additional sample falling below the detection limit. The highest median P precipitation concentration was observed in Fort Collins at 6.4 μg P L^{-1}. A strong correlation between phosphate and calcium concentrations suggested mineral dust as an important source of P wet deposition. The lowest median P precipitation concentration was measured at Mammoth Cave (0.7 μg P L^{-1}). Snowpack sample concentrations ranged from 0.45 to 37.5 μg P L^{-1}, with the highest level potentially associated with P leaching from soil. Additional measurements in a variety of locations are necessary to understand the range in phosphate concentration across regions and seasons.

6.2 Recommendations for future work

- Modeling NH_3 fluxes is highly uncertain. We establish that a correction factor or the diel pattern may be used to correct the bias introduced by using biweekly passive NH_3 measurements for flux simulations. However, this will likely vary across regions and land surface types, meaning that studies at additional locations are needed before these approaches can be implemented more broadly.

- We found that substituting reanalysis meteorology for *in situ* micrometeorology introduced large biases into NH_3 fluxes in RMNP. This was possible to correct, but it may vary in different regions. The impacts from land surface type, complex topography, and regional changes should be assessed before large-scale use of reanalysis meteorology for modeling NH_3 fluxes.

- The impacts of biweekly NH_3 concentration data and reanalysis meteorology should also be assessed for the other NH_3 bidirectional flux models (Pleim et al., 2013; Zhang et al., 2010). Although these models are similar, it will be important to assess the relative impacts on simulated fluxes from each model.

- More *in situ* measurements should be made to reconcile surface and total column measurements. These measurements should specifically target areas near heavy agricultural development. The AMoN passive NH_3 measurements are typically placed greater than 12 km from heavy agricultural development and thus miss the largest concentrations.

- The spatial footprint of high NH_3 concentration agricultural hotspots from CrIS oversampled data revealed an increasing trend that could indicate greater NH_3 emissions, increased spatial area of agriculture, or increased NH_3 lifetime. It would be helpful to quantify the relative contribution from each of these potential causes. Additionally, the impact on sensitive ecosystems from increasing hotspot areas and changing transport out of agricultural NH_3 hotspots should be assessed.

- Single facility emitters can be identified using CrIS oversampled data in addition to using regional agricultural hotspot areas. Identifying source emitters through the data record could indicate if the spatial footprint of agricultural activities is changing in the identified hotspot areas. This would help unpack the impacts of agricultural emissions on changing NH_3 hotspot areas.

- CrIS satellite retrievals could also be used to identify hot moments, or periods of large emissions, in addition to hot spot areas. The physical oversampling could be applied to different time periods associated with changes to emissions, such as cold snaps, the spring thaw, upslope transport, or fertilizer application. This would allow for the identification of emissions from varied sources.

- These results demonstrate that flow injection analysis can be used to quantify P wet deposition. Future collection of P wet deposition, using SNiPiT samplers, is proposed to quantify P wet deposition across the NADP National Trends Network. However, the samplers provided have unsatisfactory blank levels. A variety of cleaning procedures, including soaking in deionized water, cleaning with hydrogen peroxide, and repeated wash procedures, were tested. However, these did not sufficiently reduce the blank values. Before deployment in the field, other materials will need to be robustly tested to determine the blank values.

Bibliography

Allegrini, I., F. De Santis, V. Di Palo, A. Febo, C. Perrino, M. Possanzini, and A. Liberti (1987), Annular denuder method for sampling reactive gases and aerosols in the atmosphere, Science of The Total Environment, 67(1), 1-16, doi:https://doi.org/10.1016/0048-9697(87)90062-3.

Allegrini, I., A. Febo, C. Perrino, and P. Masia (1994), Measurement of Atmospheric Nitric Acid in Gas Phase and Nitrate in Particulate Matter using Annular Denuders, International Journal of Environmental Analytical Chemistry, 54(3), 183-201, doi:10.1080/03067319408034088.

Aneja, V. P., P. A. Roelle, G. C. Murray, J. Southerland, J. W. Erisman, D. Fowler, W. A. H. Asman, and N. Patni (2001), Atmospheric nitrogen compounds II: emissions, transport, transformation, deposition and assessment, Atmospheric Environment, 35(11), 1903-1911, doi:https://doi.org/10.1016/S1352-2310(00)00543-4.

Baron, J. S., H. M. Rueth, A. M. Wolfe, K. R. Nydick, E. J. Allstott, J. T. Minear, and B. Moraska (2000), Ecosystem Responses to Nitrogen Deposition in the Colorado Front Range, Ecosystems, 3(4), 352-368, doi:10.1007/s100210000032.

Baron, J. S. (2006), Hindcasting Nitrogen Deposition To Determine An Ecological Critical Load, Ecological Applications, 16(2), 433-439, doi:https://doi.org/10.1890/1051-0761(2006)016[0433:HNDTDA]2.0.CO;2.

Bauer, S. E., K. Tsigaridis, and R. Miller (2016), Significant atmospheric aerosol pollution caused by world food cultivation, Geophysical Research Letters, 43(10), 5394-5400, doi:https://doi.org/10.1002/2016GL068354.

Bauters, M., et al. (2021), Fire-derived phosphorus fertilization of African tropical forests, Nature Communications, 12(1), 5129, doi:10.1038/s41467-021-25428-3.

Beem, K. B., et al. (2010), Deposition of reactive nitrogen during the Rocky Mountain Airborne Nitrogen and Sulfur (RoMANS) study, Environmental Pollution, 158(3), 862-872, doi:https://doi.org/10.1016/j.envpol.2009.09.023.

Beer, R., et al. (2008), First satellite observations of lower tropospheric ammonia and methanol, Geophysical Research Letters, 35(9), doi:https://doi.org/10.1029/2008GL033642.

Behera, S. N., M. Sharma, V. P. Aneja, and R. Balasubramanian (2013), Ammonia in the atmosphere: a review on emission sources, atmospheric chemistry and deposition on terrestrial bodies, Environmental Science and Pollution Research, 20(11), 8092-8131, doi:10.1007/s11356-013-2051-9.

Benedict, K. B., C. M. Carrico, S. M. Kreidenweis, B. Schichtel, W. C. Malm, and J. L. Collett (2013a), A seasonal nitrogen deposition budget for Rocky Mountain National Park, Ecological Applications, 23(5), 1156-1169.

Benedict, K. B., D. Day, F. M. Schwandner, S. M. Kreidenweis, B. Schichtel, W. C. Malm, and J. L. Collett (2013b), Observations of atmospheric reactive nitrogen species in Rocky Mountain National Park and across northern Colorado, Atmospheric Environment, 64, 66-76, doi:https://doi.org/10.1016/j.atmosenv.2012.08.066.

Benedict, K. B., A. J. Prenni, C. M. Carrico, A. P. Sullivan, B. A. Schichtel, and J. L. Collett (2017), Enhanced concentrations of reactive nitrogen species in wildfire smoke, Atmospheric Environment, 148, 8-15, doi:https://doi.org/10.1016/j.atmosenv.2016.10.030.

Benedict, K. B., A. J. Prenni, A. P. Sullivan, A. R. Evanoski-Cole, E. V. Fischer, S. Callahan, B. C. Sive, Y. Zhou, B. A. Schichtel, and J. L. Collett, Jr. (2018), Impact of Front Range sources on reactive nitrogen concentrations and deposition in Rocky Mountain National Park, doi:https://doi.org/10.7717/peerj.4759.

Beusen, A. H. W., A. F. Bouwman, P. S. C. Heuberger, G. Van Drecht, and K. W. Van Der Hoek (2008), Bottom-up uncertainty estimates of global ammonia emissions from global agricultural production systems, Atmospheric Environment, 42(24), 6067-6077, doi:https://doi.org/10.1016/j.atmosenv.2008.03.044.

Bigio, L., and A. Angert (2018), Isotopic signature of atmospheric phosphate in airborne tree pollen, Atmospheric Environment, 194, 1-6, doi:https://doi.org/10.1016/j.atmosenv.2018.09.020.

Bobbink, R. (1991), Effects of Nutrient Enrichment in Dutch Chalk Grassland, Journal of Applied Ecology, 28(1), 28-41, doi:10.2307/2404111.

Boltz, D. F., and M. G. Mellon (1948), Spectrophotometric Determination of Phosphorus as Molybdiphosphoric Acid, Analytical Chemistry, 20(8), 749-751, doi:10.1021/ac60020a021.

Boot, C. M., E. K. Hall, K. Denef, and J. S. Baron (2016), Long-term reactive nitrogen loading alters soil carbon and microbial community properties in a subalpine forest ecosystem, Soil Biology and Biochemistry, 92, 211-220, doi:https://doi.org/10.1016/j.soilbio.2015.10.002.

Bowker, G.E., Schwede, D.B., Lear, G.G. et al. Quality Assurance Decisions with Air Models: A Case Study of Imputation of Missing Input Data Using EPA's Multi-layer Model. Water Air Soil Pollut 222, 391–402 (2011). https://doi.org/10.1007/s11270-011-0832-7

Bouwman, A. F., D. S. Lee, W. A. H. Asman, F. J. Dentener, K. W. Van Der Hoek, and J. G. J. Olivier (1997), A global high-resolution emission inventory for ammonia, Global Biogeochemical Cycles, 11(4), 561-587, doi:https://doi.org/10.1029/97GB02266.

Brahney, J., A. P. Ballantyne, C. Sievers, and J. C. Neff (2013), Increasing Ca2+ deposition in the western US: The role of mineral aerosols, Aeolian Research, 10, 77-87, doi:https://doi.org/10.1016/j.aeolia.2013.04.003.

Brahney, J., N. Mahowald, D. S. Ward, A. P. Ballantyne, and J. C. Neff (2015), Is atmospheric phosphorus pollution altering global alpine Lake stoichiometry?, Global Biogeochemical Cycles, 29(9), 1369-1383, doi:https://doi.org/10.1002/2015GB005137.

Bray, C. D., W. Battye, V. P. Aneja, D. Q. Tong, P. Lee, and Y. Tang (2018), Ammonia emissions from biomass burning in the continental United States, Atmospheric Environment, 187, 50-61, doi:https://doi.org/10.1016/j.atmosenv.2018.05.052.

Burling, I. R., et al. (2010), Laboratory measurements of trace gas emissions from biomass burning of fuel types from the southeastern and southwestern United States, Atmos. Chem. Phys., 10(22), 11115-11130, doi:10.5194/acp-10-11115-2010.

Burns, D. A. (2003), Atmospheric nitrogen deposition in the Rocky Mountains of Colorado and southern Wyoming—a review and new analysis of past study results, Atmospheric Environment, 37(7), 921-932, doi:https://doi.org/10.1016/S1352-2310(02)00993-7.

Burpee, B. T., et al. (2022), Identifying factors that affect mountain lake sensitivity to atmospheric nitrogen deposition across multiple scales, Water Research, 209, 117883, doi:https://doi.org/10.1016/j.watres.2021.117883.

Butler, T., F. Vermeylen, C. M. Lehmann, G. E. Likens, and M. Puchalski (2016), Increasing ammonia concentration trends in large regions of the USA derived from the NADP/AMoN network, Atmospheric Environment, 146, 132-140, doi:https://doi.org/10.1016/j.atmosenv.2016.06.033.

Cady-Pereira, K. E., et al. (2024), Validation of MUSES NH_3 observations from AIRS and CrIS against aircraft measurements from DISCOVER-AQ and a surface network in the Magic Valley, Atmos. Meas. Tech., 17(1), 15-36, doi:10.5194/amt-17-15-2024.

Cheng, J., K. Hu, J. Shen, L. Jia, R. Niu, and Z. Yang (2022), Simulation Analysis of Ammonia Leakage and Dispersion in a Large-Scale Refrigeration System, Fluid Dynamics and Materials Processing, 18(4), 1049-1066, doi:https://doi.org/10.32604/fdmp.2022.019007.

Clarisse, L., C. Clerbaux, F. Dentener, D. Hurtmans, and P.-F. Coheur (2009), Global ammonia distribution derived from infrared satellite observations, Nature Geoscience, 2(7), 479-483, doi:10.1038/ngeo551.

Clarisse, L., M. W. Shephard, F. Dentener, D. Hurtmans, K. Cady-Pereira, F. Karagulian, M. Van Damme, C. Clerbaux, and P.-F. Coheur (2010), Satellite monitoring of ammonia: A case study of the San Joaquin Valley, Journal of Geophysical Research: Atmospheres, 115(D13), doi:https://doi.org/10.1029/2009JD013291.

Clarisse, L., B. Franco, M. Van Damme, T. Di Gioacchino, J. Hadji-Lazaro, S. Whitburn, L. Noppen, D. Hurtmans, C. Clerbaux, and P. Coheur (2023), The IASI NH_3 version 4 product: averaging kernels and improved consistency, Atmos. Meas. Tech., 16(21), 5009-5028, doi:10.5194/amt-16-5009-2023.

Clark, C. M., and D. Tilman (2008), Loss of plant species after chronic low-level nitrogen deposition to prairie grasslands, Nature, 451(7179), 712-715, doi:10.1038/nature06503.

Colorado Agricultural Meteorological Network (CoAgMet). FCC01 Christman Field 5-minute Temperature Data. Colorado Climate Center, Colorado State University. Accessed June 18, 2025. Available at: https://coagmet.colostate.edu/

Colorado Department of Public Health and Environment (CDPHE), Air Pollution Control Divison (2007), Nitrogen Deposition Reduction Plan. Colorado Department of Public Health and Environment. available at: https://www.colorado.gov/pacific/cdphe/rocky-mountain-national-park-nitrogen- reduction-plan

Corwin, K. A., C. A. Corr, J. Burkhardt, and E. V. Fischer (2022), Smoke-Driven Changes in Photosynthetically Active Radiation During the US Agricultural Growing Season, Journal of Geophysical Research: Atmospheres, 127(23), e2022JD037446, doi:https://doi.org/10.1029/2022JD037446.

Corwin, K. A., J. Burkhardt, C. A. Corr, P. W. Stackhouse, A. Munshi, and E. V. Fischer (2025), Solar energy resource availability under extreme and historical wildfire smoke conditions, Nature Communications, 16(1), 245, doi:10.1038/s41467-024-54163-8.

Coughlin, J. G., C. M. Clark, L. H. Pardo, R. D. Sabo, and J. D. Ash (2023), Sensitive tree species remain at risk despite improved air quality benefits to US forests, Nature Sustainability, 6(12), 1607-1619, doi:10.1038/s41893-023-01203-8.

Day, D. E., X. Chen, K. A. Gebhart, C. M. Carrico, F. M. Schwandner, K. B. Benedict, B. A. Schichtel, and J. L. Collett (2012), Spatial and temporal variability of ammonia and other inorganic aerosol species, Atmospheric Environment, 61, 490-498, doi:https://doi.org/10.1016/j.atmosenv.2012.06.045.

de Oliveira Carneiro, L., S. F. de Vasconcelos, G. W. de Farias Neto, R. P. Brito, and K. D. Brito (2021), Improving H2S removal in the coke oven gas purification process, Separation and Purification Technology, 257, 117862, doi:https://doi.org/10.1016/j.seppur.2020.117862.

Diao, X., et al. (2024), Attributing Atmospheric Phosphorus in the Himalayas: Biomass Burning vs Mineral Dust, Environmental Science& Technology, 58(1), 459-467, doi:10.1021/acs.est.3c07670.

Ding, J., R. van der A, H. Eskes, E. Dammers, M. Shephard, R. Wichink Kruit, M. Guevara, and L. Tarrason (2024), Ammonia emission estimates using CrIS satellite observations over Europe, Atmos. Chem. Phys., 24(18), 10583-10599, doi:10.5194/acp-24-10583-2024.

Driscoll, C., et al. (2003), Nitrogen Pollution in the Northeastern United States: Sources, Effects, and Management Options, BioScience, 53(4), 357-374, doi:10.1641/0006-3568(2003)053[0357:NPITNU]2.0.CO;2.

Driscoll, C., J. B. Milford, D. K. Henze, and M. D. Bell (2024), Atmospheric reduced nitrogen: Sources, transformations, effects, and management, Journal of the Air & Waste Management Association, 74(6), 362-415, doi:10.1080/10962247.2024.2342765.

Ellis, R. A., D. J. Jacob, M. P. Sulprizio, L. Zhang, C. D. Holmes, B. A. Schichtel, T. Blett, E. Porter, L. H. Pardo, and J. A. Lynch (2013), Present and future nitrogen deposition to national parks in the United States: critical load exceedances, Atmos. Chem. Phys., 13(17), 9083-9095, doi:10.5194/acp-13-9083-2013.

Fitz, D. (2021), U.S. Environmental Protection Agency. Evaluation of Diffusion Denuder Coatings for Removing Acid Gases from Ambient Air. Office of Air Quality Planning and Standards, Emissions, Monitoring, and Analysis Division, Research Triangle Park, NC. June 2020. https://www.epa.gov/sites/default/files/2020-06/documents/denudr.pdf

Galloway, J. N., A. R. Townsend, J. W. Erisman, M. Bekunda, Z. Cai, J. R. Freney, L. A. Martinelli, S. P. Seitzinger, and M. A. Sutton (2008), Transformation of the Nitrogen Cycle: Recent Trends, Questions, and Potential Solutions, Science, 320(5878), 889-892, doi:10.1126/science.1136674.

Gao, Y., Y. Jia, G. Yu, N. He, L. Zhang, B. Zhu, and Y. Wang (2019), Anthropogenic reactive nitrogen deposition and associated nutrient limitation effect on gross primary productivity in inland water of China, Journal of Cleaner Production, 208, 530-540, doi:https://doi.org/10.1016/j.jclepro.2018.10.137.

Gebhart, K. A., B. A. Schichtel, W. C. Malm, M. G. Barna, M. A. Rodriguez, and J. L. Collett (2011), Back-trajectory-based source apportionment of airborne sulfur and nitrogen concentrations at Rocky Mountain National Park, Colorado, USA, Atmospheric Environment, 45(3), 621-633, doi:https://doi.org/10.1016/j.atmosenv.2010.10.035.

Goode, J. G., R. J. Yokelson, R. A. Susott, and D. E. Ward (1999), Trace gas emissions from laboratory biomass fires measured by open-path Fourier transform infrared spectroscopy: Fires in grass and surface fuels, Journal of Geophysical Research: Atmospheres, 104(D17), 21237-21245, doi:https://doi.org/10.1029/1999JD900360.

Guo, X., et al. (2021), Validation of IASI Satellite Ammonia Observations at the Pixel Scale Using *in situ* Vertical Profiles, Journal of Geophysical Research: Atmospheres, 126(9), e2020JD033475, doi:https://doi.org/10.1029/2020JD033475.

Han, Y., et al. (2013), Suomi NPP CrIS measurements, sensor data record algorithm, calibration and validation activities, and record data quality, Journal of Geophysical Research: Atmospheres, 118(22), 12,734-712,748, doi:https://doi.org/10.1002/2013JD020344.

Hendriks, C., R. Kranenburg, J. J. P. Kuenen, B. Van den Bril, V. Verguts, and M. Schaap (2016), Ammonia emission time profiles based on manure transport data improve ammonia modelling across north western Europe, Atmospheric Environment, 131, 83-96, doi:https://doi.org/10.1016/j.atmosenv.2016.01.043.

Hersbach, H., et al. (2020), The ERA5 global reanalysis, Quarterly Journal of the Royal Meteorological Society, 146(730), 1999-2049, doi:https://doi.org/10.1002/qj.3803.

Hicks, B. B., D. D. Baldocchi, T. P. Meyers, R. P. Hosker, and D. R. Matt (1987), A preliminary multiple resistance routine for deriving dry deposition velocities from measured quantities, Water, Air, and Soil Pollution, 36(3), 311-330, doi:10.1007/BF00229675.

Hill, J., et al. (2019), Air-quality-related health damages of maize, Nature Sustainability, 2(5), 397-403, doi:10.1038/s41893-019-0261-y.

Hogrefe, C., Bash, J. O., Pleim, J. E., Schwede, D. B., Gilliam, R. C., Foley, K. M., Appel, K. W., and R. Mathur (2023), An analysis of CMAQ gas-phase dry deposition over North America through grid-scale and land-use-specific diagnostics in the context of AQMEII4, Atmos. Chem. Phys., 23, 8119–8147, https://doi.org/10.5194/acp-23-8119-2023.

Holtgrieve, G. W., et al. (2011), A Coherent Signature of Anthropogenic Nitrogen Deposition to Remote Watersheds of the Northern Hemisphere, Science, 334(6062), 1545-1548, doi:10.1126/science.1212267.

Hoshen, J., and R. Kopelman (1976), Percolation and cluster distribution. I. Cluster multiple labeling technique and critical concentration algorithm, Physical Review B, 14(8), 3438-3445, doi:10.1103/PhysRevB.14.3438.

Hu, C., Griffis, T. J., Frie, A., Baker, J. M., Wood, J. D., Millet, D. B., et al. (2021), A multi-year constraint on ammonia emissions and deposition within the US Corn Belt. Geophysical Research Letters, 48, e2020GL090865. https://doi.org/10.1029/2020GL090865

Hussain et al., (2019). pyMannKendall: a python package for non parametric Mann Kendall family of trend tests.. Journal of Open Source Software, 4(39), 1556. https://doi.org/10.21105/joss.01556

Ianniello, A., F. Spataro, G. Esposito, I. Allegrini, M. Hu, and T. Zhu (2011), Chemical characteristics of inorganic ammonium salts in PM_{2.5} in the atmosphere of Beijing (China), Atmos. Chem. Phys., 11(21), 10803-10822, doi:10.5194/acp-11-10803-2011.

IPCC, 2022: Climate Change 2022: Impacts, Adaptation, and Vulnerability. Contribution of Working Group II to the Sixth Assessment Report of the Intergovernmental Panel on Climate Change [H.-O. Pörtner, D.C. Roberts, M. Tignor, E.S. Poloczanska, K. Mintenbeck, A. Alegría, M. Craig, S. Langsdorf, S. Löschke, V. Möller, A. Okem, B. Rama (eds.)]. Cambridge University Press. Cambridge University Press, Cambridge, UK and New York, NY, USA, 3056 pp., doi:10.1017/9781009325844.

Juncosa Calahorrano, J. F., I. B. Pollack, A. P. Sullivan, J. R. Roscioli, D. R. Caulton, M. E. McCabe, E. Li, J. R. Pierce, and E. V. Fischer (2023), Summertime Airborne Measurements of Ammonia Emissions From Cattle Feedlots and Dairies in Northeastern Colorado, Journal of Geophysical Research: Atmospheres, 128(23), e2023JD039043, doi:https://doi.org/10.1029/2023JD039043.

Juncosa Calahorrano, J. F., et al. (2024), Anatomy of Summertime Upslope Events in Northeastern Colorado: Ammonia (NH_3) Transport to the Rocky Mountains, Environmental Science& Technology, 58(38), 16922-16930, doi:10.1021/acs.est.3c10902.

Kanakidou, M., S. Myriokefalitakis, N. Daskalakis, G. Fanourgakis, A. Nenes, A. R. Baker, K. Tsigaridis, and N. Mihalopoulos (2016), Past, Present, and Future Atmospheric Nitrogen Deposition, Journal of the Atmospheric Sciences, 73(5), 2039-2047, doi:https://doi.org/10.1175/JAS-D-15-0278.1.

Kanakidou, M., S. Myriokefalitakis, and K. Tsigaridis (2018), Aerosols in atmospheric chemistry and biogeochemical cycles of nutrients, Environmental Research Letters, 13(6), 063004, doi:10.1088/1748-9326/aabcdb.

Kang, S., G. Kim, J. Roh, and E. C. Jeon (2022), Ammonia Emissions from NPK Fertilizer Production Plants: Emission Characteristics and Emission Factor Estimation, Int J Environ Res Public Health, 19(11), doi:10.3390/ijerph19116703.

Kinar, N. J., and J. W. Pomeroy (2015), Measurement of the physical properties of the snowpack, Reviews of Geophysics, 53(2), 481-544, doi:https://doi.org/10.1002/2015RG000481.

Kong, B., N. Liu, L. Fan, L. Lin, L. Yang, H. Chen, Y. Wang, Y. Zhang, and Y. Xu (2022), Evaluation of surface meteorology parameters and heat fluxes from CFSR and ERA5 over the Pacific Arctic Region, Quarterly Journal of the Royal Meteorological Society, 148(747), 2973-2990, doi:https://doi.org/10.1002/qj.4346.

Korb, J. E., and T. A. Ranker (2001), Changes in stand composition and structure between 1981 and 1996 in four Front Range plant communities in Colorado, Plant Ecology, 157(1), 1-11, doi:10.1023/A:1013772220131.

LaCount, M. D., R. A. Haeuber, T. R. Macy, and B. A. Murray (2021), Reducing power sector emissions under the 1990 Clean Air Act Amendments: A retrospective on 30 years of program development and implementation, Atmospheric Environment, 245, 118012, doi:https://doi.org/10.1016/j.atmosenv.2020.118012.

Lamarque, J. F., et al. (2010), Historical (1850–2000) gridded anthropogenic and biomass burning emissions of reactive gases and aerosols: methodology and application, Atmos. Chem. Phys., 10(15), 7017-7039, doi:10.5194/acp-10-7017-2010.

Lee, T., S. M. Kreidenweis, and J. L. Collett (2004), Aerosol Ion Characteristics During the Big Bend Regional Aerosol and Visibility Observational Study, Journal of the Air& Waste Management Association, 54(5), 585-592, doi:10.1080/10473289.2004.10470927.

Li, Y., B. A. Schichtel, J. T. Walker, D. B. Schwede, X. Chen, C. M. B. Lehmann, M. A. Puchalski, D. A. Gay, and J. L. Collett (2016), Increasing importance of deposition of reduced nitrogen in the United States, Proceedings of the National Academy of Sciences, 113(21), 5874-5879, doi:10.1073/pnas.1525736113.

Li, Y., et al. (2017), Temporal and spatial variability of ammonia in urban and agricultural regions of northern Colorado, United States, Atmos. Chem. Phys., 17(10), 6197-6213, doi:10.5194/acp-17-6197-2017.

Lindaas, J., et al. (2021), Emissions of Reactive Nitrogen From Western U.S. Wildfires During Summer 2018, Journal of Geophysical Research: Atmospheres, 126(2), e2020JD032657, doi:https://doi.org/10.1029/2020JD032657.

Liu, M., et al. (2018), Rapid SO2 emission reductions significantly increase tropospheric ammonia concentrations over the North China Plain, Atmos. Chem. Phys., 18(24), 17933-17943, doi:10.5194/acp-18-17933-2018.

Lyddy-Meaney, A. J., P. S. Ellis, P. J. Worsfold, E. C. V. Butler, and I. D. McKelvie (2002), A compact flow injection analysis system for surface mapping of phosphate in marine waters, Talanta, 58(6), 1043-1053, doi:https://doi.org/10.1016/S0039-9140(02)00428-9.

Lynam, M. M., et al. (2023), Atmospheric dry and wet deposition of total phosphorus to the Great Lakes, Atmospheric Environment, 313, 120049, doi:https://doi.org/10.1016/j.atmosenv.2023.120049.

Mackey, K. R. M., and A. Paytan (2009), Phosphorus Cycle, in Encyclopedia of Microbiology (Third Edition), edited by M. Schaechter, pp. 322-334, Academic Press, Oxford, doi:https://doi.org/10.1016/B978-012373944-5.00056-0.

Mahowald, N., et al. (2008), Global distribution of atmospheric phosphorus sources, concentrations and deposition rates, and anthropogenic impacts, Global Biogeochemical Cycles, 22(4), doi:https://doi.org/10.1029/2008GB003240.

Massad, R. S., E. Nemitz, and M. A. Sutton (2010), Review and parameterisation of bi-directional ammonia exchange between vegetation and the atmosphere, Atmos. Chem. Phys., 10(21), 10359-10386, doi:10.5194/acp-10-10359-2010.

Mayer, J., M. Mayer, L. Haimberger, and C. Liu (2022), Comparison of Surface Energy Fluxes from Global to Local Scale, Journal of Climate, 35(14), 4551-4569, doi:https://doi.org/10.1175/JCLI-D-21-0598.1.

Meyers, T. P., Finkelstein, P., Clarke, J., Ellestad, T. G., & Sims, P. F. (1998). A multilayer model for inferring dry deposition using standard meteorological measurements. Journal of Geophysical Research, 103(D17), 22645–22661.

Montes, F., C. A. Rotz, and H. Chaoui (2009). Process Modeling of Ammonia Volatilization from Ammonium Solution and Manure Surfaces: A Review with Recommended Models. Transactions of the ASABE, 52(5), 1707-1720, doi:https://doi.org/10.13031/2013.29133.

Myriokefalitakis, S., A. Nenes, A. R. Baker, N. Mihalopoulos, and M. Kanakidou (2016), Bioavailable atmospheric phosphorous supply to the global ocean: a 3-D global modeling study, Biogeosciences, 13(24), 6519-6543, doi:10.5194/bg-13-6519-2016.

Naimie, L. E., A. P. Sullivan, K. B. Benedict, A. J. Prenni, B. C. Sive, B. A. Schichtel, E. V. Fischer, I. Pollack, and J. Collett (2022), $PM_{2.5}$ in Carlsbad Caverns National Park: Composition, sources, and visibility impacts, Journal of the Air& Waste Management Association, 72(11), 1201-1218, doi:10.1080/10962247.2022.2081634.

Napari, I., M. Noppel, H. Vehkamäki, and M. Kulmala (2002), Parametrization of ternary nucleation rates for H2SO4-NH_3-H2O vapors, Journal of Geophysical Research: Atmospheres, 107(D19), AAC 6-1-AAC 6-6, doi:https://doi.org/10.1029/2002JD002132.

National Atmospheric Deposition Program (NRSP-3). 2022. NADP Program Office, Wisconsin State Laboratory of Hygiene, 465 Henry Mall, Madison, WI 53706.

NEON (National Ecological Observatory Network). Site management and event reporting (DP1.10111.001), RELEASE-2023. https://doi.org/10.48443/9p2t-hj77. Dataset accessed from https://data.neonscience.org/data-products/DP1.10111.001/RELEASE-2024 on September 05, 2023.

Nemitz, E., C. Milford, and M. A. Sutton (2001), A two-layer canopy compensation point model for describing bi-directional biosphere-atmosphere exchange of ammonia, Quarterly Journal of the Royal Meteorological Society, 127(573), 815-833, doi:https://doi.org/10.1002/qj.49712757306.

O'Dell, K. A.-O., K. Bilsback, B. A.-O. Ford, S. E. Martenies, S. A.-O. Magzamen, E. A.-O. Fischer, and J. A.-O. X. Pierce (2021), Estimated Mortality and Morbidity Attributable to Smoke Plumes in the United States: Not Just a Western US Problem, GeoHealth(2471-1403 (Electronic)), doi:https://doi.org/10.1029/2021GH000457.

Pan, D., et al. (2021), Ammonia Dry Deposition in an Alpine Ecosystem Traced to Agricultural Emission Hotpots, Environmental Science& Technology, 55(12), 7776-7785, doi:10.1021/acs.est.0c05749.

Pan, D., et al. (2024), Regime shift in secondary inorganic aerosol formation and nitrogen deposition in the rural United States, Nature Geoscience, 17(7), 617-623, doi:10.1038/s41561-024-01455-9.

Pan, Y., et al. (2020), Systematic low bias of passive samplers in characterizing nitrogen isotopic composition of atmospheric ammonia, Atmospheric Research, 243, 105018, doi:https://doi.org/10.1016/j.atmosres.2020.105018.

Picotte, J. J., K. Bhattarai, D. Howard, J. Lecker, J. Epting, B. Quayle, N. Benson, and K. Nelson (2020), Changes to the Monitoring Trends in Burn Severity program mapping production procedures and data products, Fire Ecology, 16(1), 16, doi:10.1186/s42408-020-00076-y.

Pinder, R. W., J. T. Walker, J. O. Bash, K. E. Cady-Pereira, D. K. Henze, M. Luo, G. B. Osterman, and M. W. Shephard (2011), Quantifying spatial and seasonal variability in atmospheric ammonia with *in situ* and space-based observations, Geophysical Research Letters, 38(4), doi:https://doi.org/10.1029/2010GL046146.

Pleim, J. E., J. O. Bash, J. T. Walker, and E. J. Cooter (2013), Development and evaluation of an ammonia bidirectional flux parameterization for air quality models, Journal of Geophysical Research: Atmospheres, 118(9), 3794-3806, doi:https://doi.org/10.1002/jgrd.50262.

Puchalski, M. A., M. E. Sather, J. T. Walker, C. M. B. Lehmann, D. A. Gay, J. Mathew, and W. P. Robarge (2011), Passive ammonia monitoring in the United States: Comparing three different sampling devices, Journal of Environmental Monitoring, 13(11), 3156-3167, doi:10.1039/C1EM10553A.

Puchalski, M. A., C. M. Rogers, R. Baumgardner, K. P. Mishoe, G. Price, M. J. Smith, N. Watkins, and C. M. Lehmann (2015), A statistical comparison of active and passive ammonia measurements collected at Clean Air Status and Trends Network (CASTNET) sites, Environmental science : processes & impacts., 17(2), 358-369, doi:10.1039/c4em00531g.

Roberts, J. M., et al. (2020), The nitrogen budget of laboratory-simulated western US wildfires during the FIREX 2016 Fire Lab study, Atmos. Chem. Phys., 20(14), 8807-8826, doi:10.5194/acp-20-8807-2020.

Ruttenberg, K. C. (2003), 8.13 - The Global Phosphorus Cycle, in Treatise on Geochemistry, edited by H. D. Holland and K. K. Turekian, pp. 585-643, Pergamon, Oxford, doi:https://doi.org/10.1016/B0-08-043751-6/08153-6.

Schiferl, L. D., et al. (2016), Interannual variability of ammonia concentrations over the United States: sources and implications, Atmos. Chem. Phys., 16(18), 12305-12328, doi:10.5194/acp-16-12305-2016.

Schrader, F., M. Schaap, U. Zöll, R. Kranenburg, and C. Brümmer (2018), The hidden cost of using low-resolution concentration data in the estimation of NH_3 dry deposition fluxes, Scientific Reports, 8(1), 969, doi:10.1038/s41598-017-18021-6.

Schwede, D. B., and G. G. Lear (2014), A novel hybrid approach for estimating total deposition in the United States, Atmospheric Environment, 92, 207-220, doi:https://doi.org/10.1016/j.atmosenv.2014.04.008.

Sen, P. K. (1968), Estimates of the Regression Coefficient Based on Kendall's Tau, Journal of the American Statistical Association, 63(324), 1379-1389, doi:10.1080/01621459.1968.10480934.

Sequeira, R. (1993), On the large-scale impact of arid dust on precipitation chemistry of the continental northern hemisphere, Atmospheric Environment. Part A. General Topics, 27(10), 1553-1565, doi:https://doi.org/10.1016/0960-1686(93)90155-R.

Shen, J., D. Chen, M. Bai, J. Sun, T. Coates, S. K. Lam, and Y. Li (2016), Ammonia deposition in the neighbourhood of an intensive cattle feedlot in Victoria, Australia, Scientific Reports, 6(1), 32793, doi:10.1038/srep32793.

Shephard, M. W., and K. E. Cady-Pereira (2015), Cross-track Infrared Sounder (CrIS) satellite observations of tropospheric ammonia, Atmos. Meas. Tech., 8(3), 1323-1336, doi:10.5194/amt-8-1323-2015.

Smith, V. H., G. D. Tilman, and J. C. Nekola (1999), Eutrophication: impacts of excess nutrient inputs on freshwater, marine, and terrestrial ecosystems, Environmental Pollution, 100(1), 179-196, doi:https://doi.org/10.1016/S0269-7491(99)00091-3.

Solomon, P. A., D. Crumpler, J. B. Flanagan, R. K. M. Jayanty, E. E. Rickman, and C. E. McDade (2014), U.S. National $PM_{2.5}$ Chemical Speciation Monitoring Networks—CSN and IMPROVE: Description of networks, Journal of the Air& Waste Management Association, 64(12), 1410-1438, doi:10.1080/10962247.2014.956904.

Someya, Y., R. Imasu, K. Shiomi, and N. Saitoh (2020), Atmospheric ammonia retrieval from the TANSO-FTS/GOSAT thermal infrared sounder, Atmos. Meas. Tech., 13(1), 309-321, doi:10.5194/amt-13-309-2020.

Stratton, J., J. Ham, and T. Borch (2018), Ammonia Emissions from Subalpine Forest and Mountain Grassland Soils in Rocky Mountain National Park, Journal of Environmental Quality, 47(4), 778-785, doi:https://doi.org/10.2134/jeq2018.01.0023.

Stull, R. B. (1988), An Introduction to Boundary Layer Meteorology; Kluwer Academic, Dordrecht, doi: https://doi.org/10.1007/978-94-009-3027-8.

Su, B., et al. (2023), Enrichment of calcium in sea spray aerosol: insights from bulk measurements and individual particle analysis during the R/V Xuelong cruise in the summertime in Ross Sea, Antarctica, Atmos. Chem. Phys., 23(18), 10697-10711, doi:10.5194/acp-23-10697-2023.

Sun, K., et al. (2015), Validation of TES ammonia observations at the single pixel scale in the San Joaquin Valley during DISCOVER-AQ, Journal of Geophysical Research: Atmospheres, 120(10), 5140-5154, doi:https://doi.org/10.1002/2014JD022846.

Sutton, M. A., et al. (2013), Towards a climate-dependent paradigm of ammonia emission and deposition, Philosophical Transactions of the Royal Society B: Biological Sciences, 368(1621), 20130166, doi:10.1098/rstb.2013.0166.

Sutton, M. A., J. K. Schjørring, G. P. Wyers, J. H. Duyzer, P. Ineson, D. S. Powlson, D. Fowler, D. S. Jenkinson, J. L. Monteith, and M. H. Unsworth (1995), Plant—atmosphere exchange of ammonia, Philosophical Transactions of the Royal Society of London. Series A: Physical and Engineering Sciences, 351(1696), 261-278, doi:doi:10.1098/rsta.1995.0033.

Tanner, E., N. Buchmann, and W. Eugster (2022), Agricultural ammonia dry deposition and total nitrogen deposition to a Swiss mire, Agriculture, Ecosystems& Environment, 336, 108009, doi:https://doi.org/10.1016/j.agee.2022.108009.

Thom, A. S. (1975), Momentum, mass and heat exchange of plant communities. Vol.1, Edited by J.L. Monteith, London.

Tipping, E., et al. (2014), Atmospheric deposition of phosphorus to land and freshwater, Environmental Science: Processes& Impacts, 16(7), 1608-1617, doi:10.1039/C3EM00641G.

Tomsche, L., et al. (2023), Measurement report: Emission factors of NH_3 and NHx for wildfires and agricultural fires in the United States, Atmos. Chem. Phys., 23(4), 2331-2343, doi:10.5194/acp-23-2331-2023.

U.S. EPA, 2020 National Emissions Inventory (NEI) Data, available at [U.S. Environmental Protection Agency (.gov) https://www.epa.gov/air-emissions-inventories/2020-national-emissions-inventory-nei-data] (accessed 05/25/2025).

U.S. EPA Clean Air Markets Division (2024a), Clean Air Status and Trends Network (CASTNET), [Weekly Dry Deposition], Available at www.epa.gov/castnet, Date accessed: [02 20, 2024]

U.S. EPA Clean Air Markets Division (2024b), Clean Air Status and Trends Network (CASTNET), [Weekly Filter Pack], Available at www.epa.gov/castnet, Date accessed: [02 20, 2024]

Van Damme, M., et al. (2015), Towards validation of ammonia (NH₃) measurements from the IASI satellite, Atmos. Meas. Tech., 8(3), 1575-1591, doi:10.5194/amt-8-1575-2015.

Van Damme, M., L. Clarisse, S. Whitburn, J. Hadji-Lazaro, D. Hurtmans, C. Clerbaux, and P.-F. Coheur (2018), Industrial and agricultural ammonia point sources exposed, Nature, 564(7734), 99-103, doi:10.1038/s41586-018-0747-1.

Vicars, W. C., J. O. Sickman, and P. J. Ziemann (2010), Atmospheric phosphorus deposition at a montane site: Size distribution, effects of wildfire, and ecological implications, Atmospheric Environment, 44(24), 2813-2821, doi:https://doi.org/10.1016/j.atmosenv.2010.04.055.

Vitousek, P. M., S. Porder, B. Z. Houlton, and O. A. Chadwick (2010), Terrestrial phosphorus limitation: mechanisms, implications, and nitrogen–phosphorus interactions, Ecological Applications, 20(1), 5-15, doi:https://doi.org/10.1890/08-0127.1.

Walker, J. T., P. Spence, S. Kimbrough, and W. Robarge (2008), Inferential model estimates of ammonia dry deposition in the vicinity of a swine production facility, Atmospheric Environment, 42(14), 3407-3418, doi:https://doi.org/10.1016/j.atmosenv.2007.06.004.

Walker, J. T., et al. (2019a), Toward the improvement of total nitrogen deposition budgets in the United States, Science of The Total Environment, 691, 1328-1352, doi:https://doi.org/10.1016/j.scitotenv.2019.07.058.

Walker, J. T., M. D. Bell, D. Schwede, A. Cole, G. Beachley, G. Lear, and Z. Wu (2019b), Aspects of uncertainty in total reactive nitrogen deposition estimates for North American critical load applications, Science of The Total Environment, 690, 1005-1018, doi:https://doi.org/10.1016/j.scitotenv.2019.06.337.

Walker, J., G. Beachley, L. Zhang, K. B. Benedict, B. C. Sive, and D. B. Schwede (2020), A review of measurements of air-surface exchange of reactive nitrogen in natural ecosystems across North America, Science of The Total Environment, 698, 133975, doi:https://doi.org/10.1016/j.scitotenv.2019.133975.

Wang, R., et al. (2021), Monthly Patterns of Ammonia Over the Contiguous United States at 2-km Resolution, Geophysical Research Letters, 48(5), e2020GL090579, doi:https://doi.org/10.1029/2020GL090579.

Wang, R., D. Pan, X. Guo, K. Sun, L. Clarisse, M. Van Damme, P. F. Coheur, C. Clerbaux, M. Puchalski, and M. A. Zondlo (2023), Bridging the spatial gaps of the Ammonia Monitoring Network using satellite ammonia measurements, Atmos. Chem. Phys., 23(20), 13217-13234, doi:10.5194/acp-23-13217-2023.

Wang, Z., H. Tian, J. Yang, H. Shi, S. Pan, Y. Yao, K. Banger, and Q. Yang (2020), Coupling of Phosphorus Processes With Carbon and Nitrogen Cycles in the Dynamic Land Ecosystem Model: Model Structure, Parameterization, and Evaluation in Tropical Forests, Journal of Advances in Modeling Earth Systems, 12(10), e2020MS002123, doi:https://doi.org/10.1029/2020MS002123.

Warner, J. X., Z. Wei, L. L. Strow, R. R. Dickerson, and J. B. Nowak (2016), The global tropospheric ammonia distribution as seen in the 13-year AIRS measurement record, Atmos. Chem. Phys., 16(8), 5467-5479, doi:10.5194/acp-16-5467-2016.

Wentworth G. R., Murphy J. G., Benedict K. B., Bangs E. J., Collett Jr J. L. (2016), The role of dew as a night-time reservoir and morning source for atmospheric ammonia. Atmospheric Chemistry and Physics. 2016;16:7435–7449. doi: 10.5194/acp-16-7435-2016.

Wichink Kruit, R. J., M. Schaap, F. J. Sauter, M. C. van Zanten, and W. A. J. van Pul (2012), Modeling the distribution of ammonia across Europe including bi-directional surface–atmosphere exchange, Biogeosciences, 9(12), 5261-5277, doi:10.5194/bg-9-5261-2012.

Wipf, S., M. Sommerkorn, M. I. Stutter, E. R. J. Wubs, and R. van der Wal (2015), Snow cover, freeze-thaw, and the retention of nutrients in an oceanic mountain ecosystem, Ecosphere, 6(10), art207, doi:https://doi.org/10.1890/ES15-00099.1.

Wyer, K. E., D. B. Kelleghan, V. Blanes-Vidal, G. Schauberger, and T. P. Curran (2022), Ammonia emissions from agriculture and their contribution to fine particulate matter: A review of implications for human health, Journal of Environmental Management, 323, 116285, doi:https://doi.org/10.1016/j.jenvman.2022.116285.

Xing, Y. F., Xu Y. H., Shi M. H., Lian Y. X. The impact of $PM_{2.5}$ on the human respiratory system. J Thorac Dis. 2016 Jan;8(1):E69-74. doi: 10.3978/j.issn.2072-1439.2016.01.19. PMID: 26904255; PMCID: PMC4740125.

Xiu, A., and J. E. Pleim (2001), Development of a Land Surface Model. Part I: Application in a Mesoscale Meteorological Model, Journal of Applied Meteorology, 40(2), 192-209, doi:https://doi.org/10.1175/1520-0450(2001)040<0192:DOALSM>2.0.CO;2.

Yokelson, R. J., et al. (2009), Emissions from biomass burning in the Yucatan, Atmos. Chem. Phys., 9(15), 5785-5812, doi:10.5194/acp-9-5785-2009.

Yu, F. A.-O., A. A.-O. Nair, and G. A.-O. Luo (2018), Long-Term Trend of Gaseous Ammonia Over the United States: Modeling and Comparison With Observations, J Geophys Res Atmos(2169-897X (Print)).

Zhan, X., et al. (2017), Evidence for the Importance of Atmospheric Nitrogen Deposition to Eutrophic Lake Dianchi, China, Environmental Science & Technology, 51(12), 6699-6708, doi:10.1021/acs.est.6b06135.

Zhang, L., J. R. Brook., and R. Vet (2003), A revised parameterization for gaseous dry deposition in air-quality models, Atmos. Chem. Phys., 3, 2067–2082, doi:https://doi.org/10.5194/acp-3-2067-2003.

Zhang, L., L. P. Wright, and W. A. H. Asman (2010), Bi-directional air-surface exchange of atmospheric ammonia: A review of measurements and a development of a big-leaf model for applications in regional-scale air-quality models, Journal of Geophysical Research: Atmospheres, 115(D20), doi:https://doi.org/10.1029/2009JD013589.

Zhou, X., K. Josey, L. Kamareddine, M. Caine, T. Liu, L. Mickley, M. Cooper, and F. Dominici (2021), Excess of COVID-19 cases and deaths due to fine particulate matter exposure during the 2020 wildfires in the United States., Sci Adv.(2375-2548 (Electronic)), doi:10.1126/sciadv.abi8789.

Zhuang, Y., R. Fu, B. D. Santer, R. E. Dickinson, and A. Hall (2021), Quantifying contributions of natural variability and anthropogenic forcings on increased fire weather risk over the western United States, Proceedings of the National Academy of Sciences, 118(45), e2111875118, doi:10.1073/pnas.2111875118.

Appendix A

The Sensitivity of Simulated Ammonia Fluxes in Rocky Mountain National Park to Measurement Time Resolution and Meteorological Inputs

A.1 NH_3 concentration comparisons

AirSentry NH_3 concentration measurements at the nearby EPA shelter are compared with University Research Glassware (URG) denuder measurements taken on the tower during the summer of 2021. URG annular denuder and filter pack samplers were deployed at the site to measure inorganic gas and particle species (Allegrini et al., 1987; Allegrini et al., 1994; Fitz, 2021). For this work, we will only consider gas phase NH_3 measurements. Measurements were conducted as described in Naimie et al. (2022), with a few notable differences. The flow was increased from 10 L min^{-1} to 16 L min^{-1} to decrease the sampling time needed. Samples were collected for 4-hour periods during the day and 6 hours overnight. Samples were collected in duplicate at the tower top (25.35 m-agl) and a mid-canopy height. Only the tower top samples are considered for this work. The injection volume of both methods was increased from 50 μL to 200 μL and the analysis time was 17 minutes. Based on previous work the relative standard deviations (RSDs) of major aerosol ion concentration measurements (NO_3^-, SO_4^{2-}, and NH_4^+) are estimated to be between 3-5% and the RSDs for replicate denuder gas concentration measurements are estimated to be approximately 10% (Lee et al., 2004).

In Figure A.1, raw AirSentry NH_3 data (panel a.) and AirSentry NH_3 data normalized to the biweekly passive concentration (panel b.) are plotted against the URG NH_3 data. Generation of the 30-minute NH_3 data set (panel b.) is described in the main text. URG sample periods were 4 hours during the day or 6 hours overnight. On sampling days, 2 or 3 daytime samples were taken, and 1 overnight sample was taken. In both panels, the 95% confidence interval of the linear fit (shown shaded in red) overlaps with the one-to-one line (y = x). Here we note that the concentrations during the intensive sampling period agree well between the AirSentry and URG measurements of NH_3. Additionally, the normalized AirSentry data set (panel b.), which will be used for the bidirectional exchange simulations, agrees well with the URG measurements of NH_3.

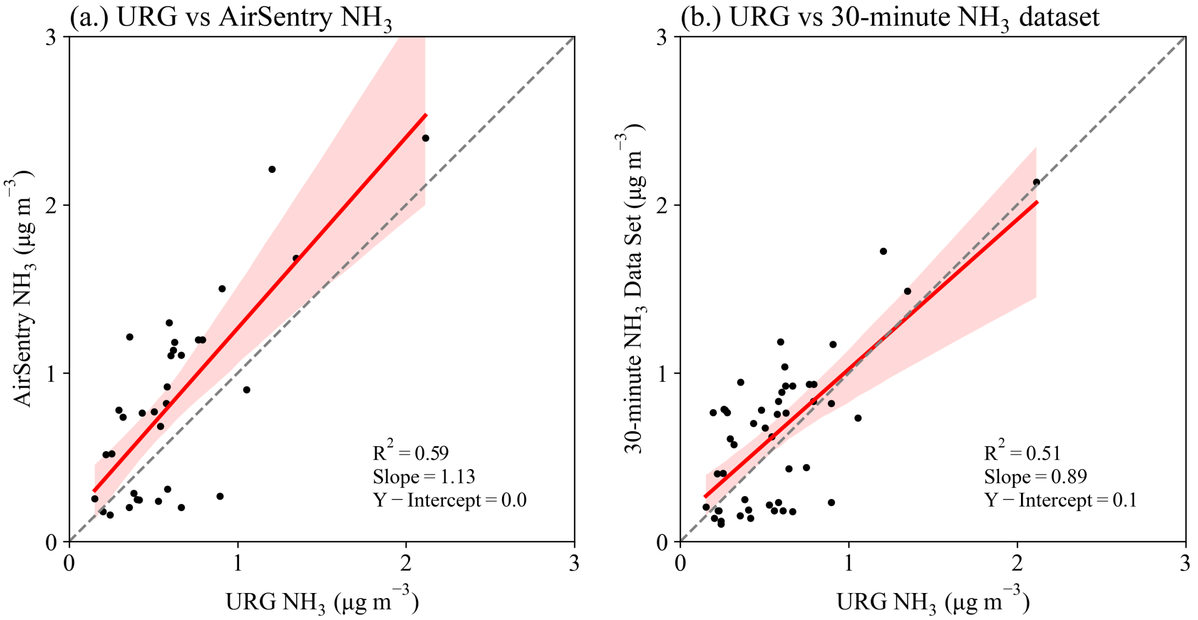

Figure A.1: NH_3 measurements from the nearby EPA shelter using an AirSentry are compared with URG denuder measurements taken at the NEON tower. The least-squares linear fits are shown in red, with the 95% confidence interval shaded for the fit. The one-to-one line is grey-dashed. (a.) Raw NH_3 concentration data from the AirSentry are compared directly to URG denuder measurements. (b.) The scaled AirSentry 30-minute NH_3 data were generated using the AirSentry NH_3 and biweekly passive NH_3.

A.2 Direct comparison of meteorological parameters

Parameters used for the bidirectional exchange simulations are compared between the ERA5 reanalysis and NEON tower *in situ* data (Figure A.2). Units for each parameter are given in the title. We find that temperature (e.), pressure (f.), air density (g.), and soil temperature (i.) agree very well. Each has an R^2 above 0.8 and a slope within 10% of unity. Notably, Obukhov length (c.) from ERA5 reanalysis and NEON tower *in situ* data are not correlated. The other parameters important

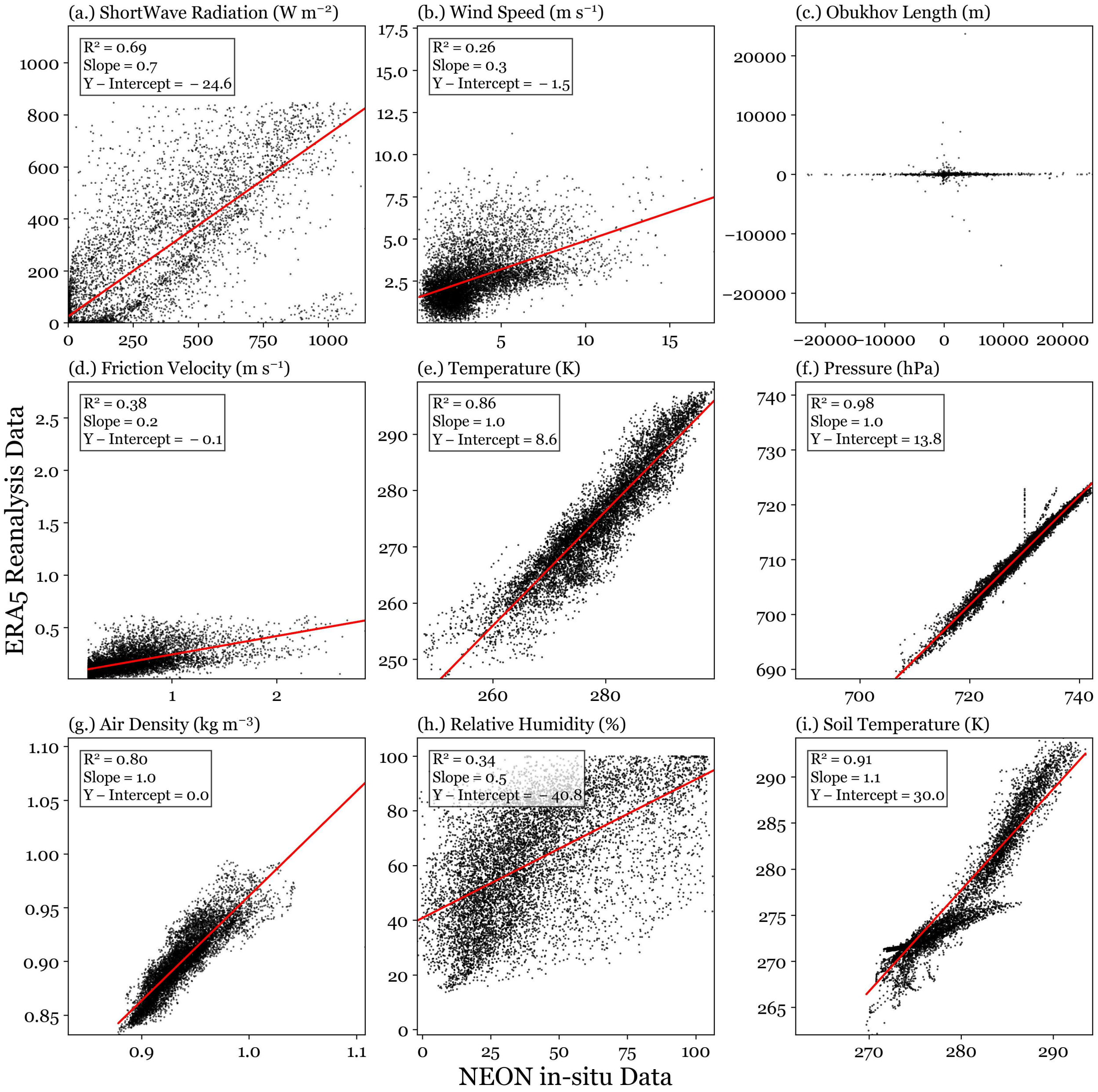

Figure A.2: NEON in-situ measurement data are plotted against the ERA5 reanalysis data for each parameter used in the bidirectional exchange simulations. The linear fit for each pair of data are given in red.

for understanding the turbulent nature of the atmosphere (wind speed, and friction velocity), have some correlation between data sets.

A.3 Diel pattern of NH_3 mixing ratios

NH_3 mixing ratios were used to generate an annual average diel pattern. The variability of mixing ratios at 30-minute time steps is shown in Figure A.3a. The mean diel profile is shown in Figure A.3b.

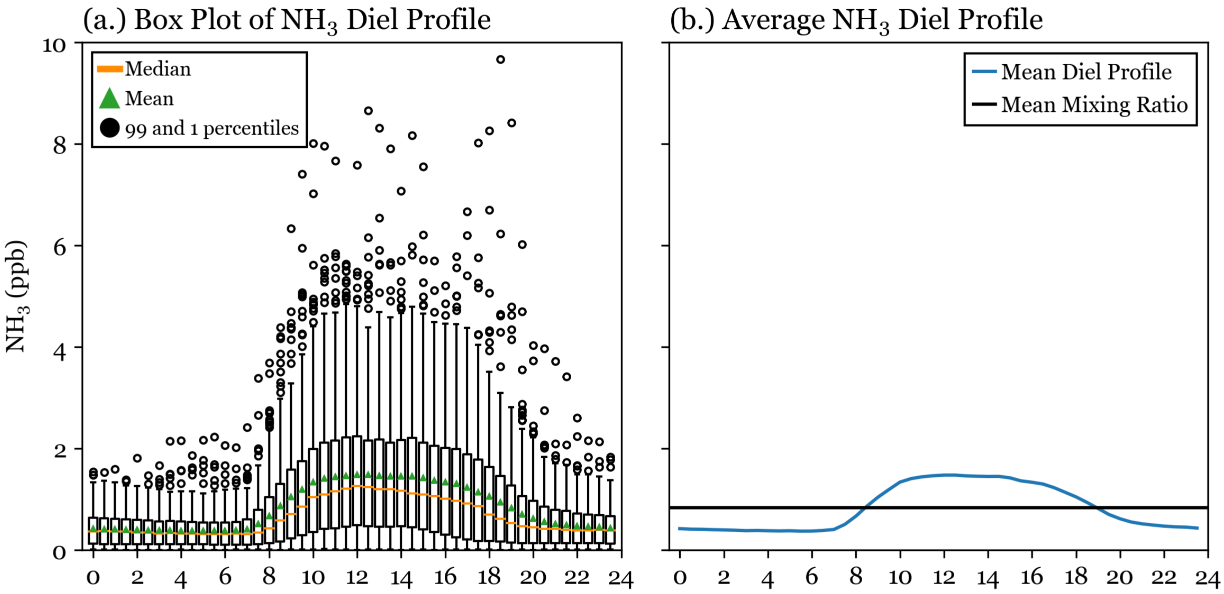

Figure A.3: The diel pattern of the NH_3 mixing ratio is shown for the full year of data. (a.) Box plot of 30-minute NH_3 mixing ratio values. The median of each box is shown in orange, the mean is shown as a green triangle, the boxes show the 25^{th} and 75^{th} percentile, the whiskers are determined at 1.5 times the interquartile range, and the black dots show outliers. (b.) The mean diel profile is shown in green, and the annual average mixing ratio is black.

A.4 Site-specific correction factor with ERA5 meteorology

Figure A.4 shows a comparison of the 30-minute NH_3 and biweekly NH_3 simulations. The 30-minute NH_3 simulation uses *in situ* meteorology. The biweekly NH_3 simulation has two sets of simulations run with biweekly integrated NH_3 concentration: 1. Simulated with *in situ* meteorology and 2. Simulated with ERA5 meteorology.

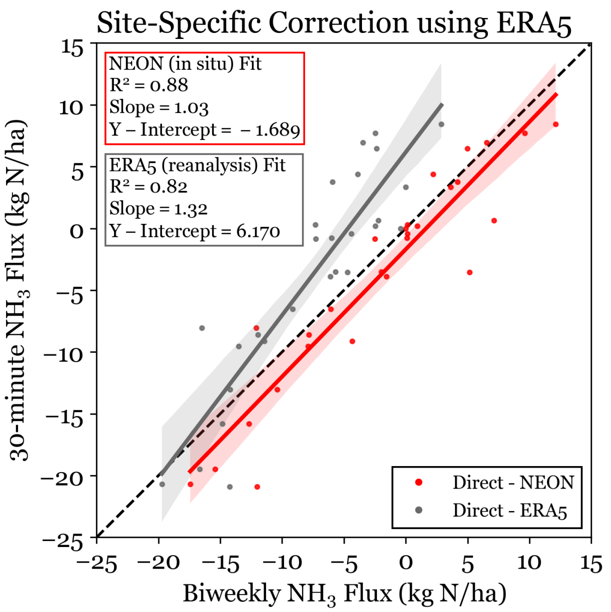

Figure A.4: Bidirectional NH_3 flux simulations are plotted for 30-minute NH_3 concentration data and biweekly integrated NH_3 concentration data. The biweekly NH_3 simulations were run using *in situ* (NEON Tower) and reanalysis (ERA5) meteorology and soil parameters. Bidirectional NH_3 fluxes are plotted as net flux over a two-week period. The least squares linear regression is plotted for the data. Shading around the linear regression shows the 95% confidence interval of the fit.

A.5 Sensitivity of simulations to LAI, TAN, and NH_3 concentration

The sensitivity of our flux results was tested against several key parameters: LAI, TAN, and NH_3 concentration. NEON derives LAI at 1 m resolution using remote sensing data. The 1 km by 1 km grid cell surrounding the NEON tower site in RMNP in shown in Figure A.5. The box used to estimate a mean LAI value for the area surrounding the site was generated to maximize the are covered without intersecting with roadways or buildings near the site.

For sensitivity testing, a set of mean values was generated for average square areas beginning at 1 square meter and increasing to 400 square meters around the tower site. The minimum value was

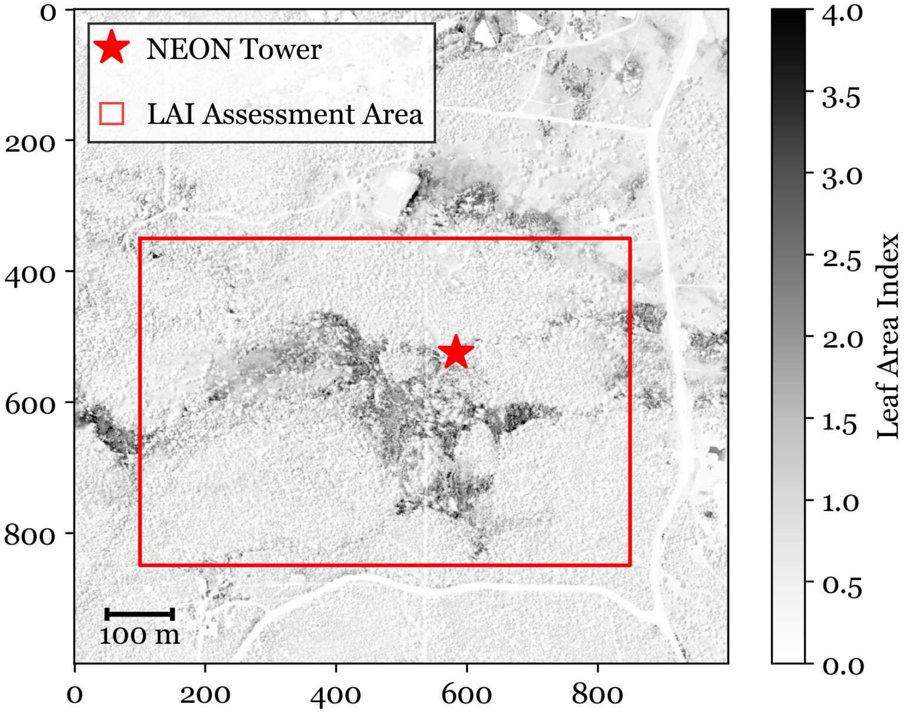

Figure A.5: Leaf area index is shown from the NEON product: “LAI-spectrometer-mosaic”. The axis values are meters of the given grid cell from the product output of 1 km by 1 km land surfaces.

0.2 and the maximum value was 1.4. These are likely extreme values. The response of simulations to LAI changes is shown in Figure A.6. On average, reducing LAI to 0.2 made NH_3 fluxes more positive by 0.08 ng N m^{-2} s^{-1} and increasing LAI to 1.4 made NH_3 fluxes more negative by 0.09 ng N m^{-2} s^{-1}. The sensitivity to TAN values was assessed using the standard deviation (4.7) of measurements taken by Stratton et al. (2018). In Figure A.6b., flux simulations using the mean TAN value measured by Stratton et al. (2018) is compared with simulations using a TAN value of 5.9 and 15.3 mg kg^{-1}. NH_3 fluxes shown here are more sensitive to the change in TAN than LAI. On average, decreasing TAN to 5.9 mg kg^{-1} made NH_3 fluxes more negative by 0.9 ng N m^{-2} s^{-1} and increasing TAN to 15.3 made NH_3 fluxes more positive by 0.9 ng N m^{-2} s^{-1}.

Lastly, we tested the sensitivity of NH_3 flux to changes in atmospheric NH_3 concentration (see Figure A.7). The atmospheric NH_3 concentration was scaled by values ranging from 0.5 to 1.5. The observed bias for passive NH_3 sampling methods from Puchalski et al. (2011) was a 9%

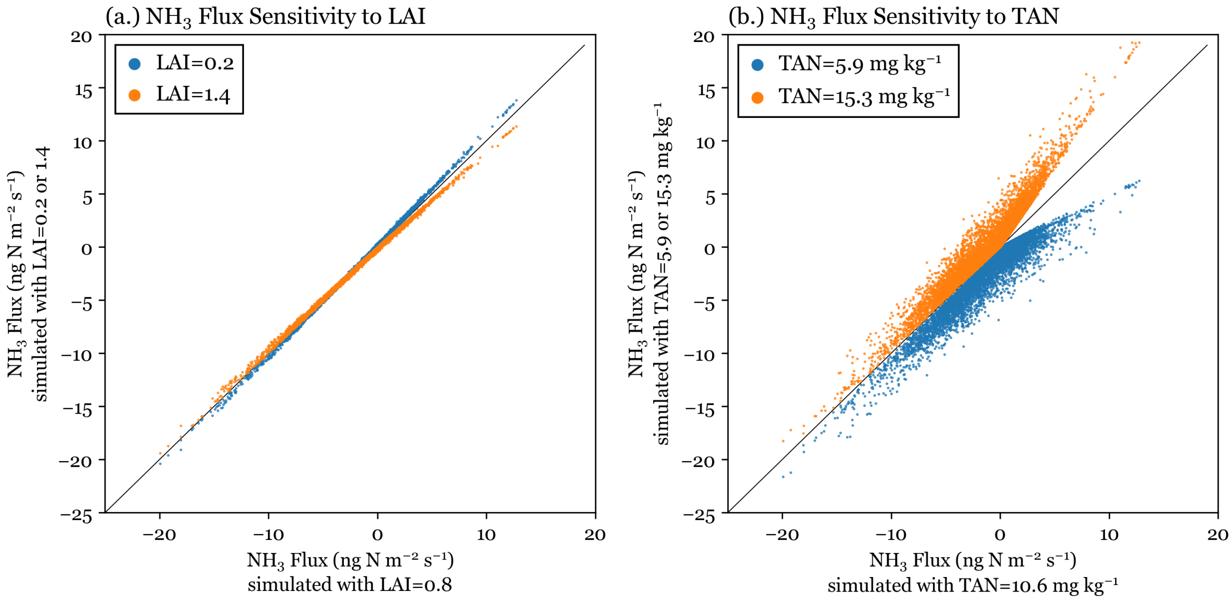

Figure A.6: NH_3 flux sensitivities are assessed for (a.) LAI and (b.) TAN. Each sensitivity test is plotted against the initial simulation parameters (LAI = 0.8 and TAN = 10.6 mg kg^{-1}).

underestimation. Increasing (decreasing) NH_3 concentration by 10% increased (decreased) the seasonal mean fluxes by 0.1 to 0.6 ng N m^{-2} s^{-1}.

At both times (12:00:00 and 00:00:00), the differences in simulated fluxes are uniformly distributed for the reduced and increased values. Notably, at 12:00:00, when all mean simulated fluxes are negative, the calculated fractional differences are very similar across seasons and close to the input scale factor. At 00:00:00, when mean fluxes are closer to zero, the fractional differences are much larger. We also see that flux direction changes for these simulations with a concentration change of only about 25The absolute difference in fluxes is typically, although not always, larger for the larger magnitude mean fluxes. While the largest spread at 00:00:00 is about 1.75 (ng N m^{-2} s^{-1}). Interestingly, in the night simulation (00:00:00), the difference between minimum and maximum simulated values is largest for JJA, which is not the largest magnitude flux value. NH_3 concentration sensitivity was also tested by scaling the input concentration by 9% to account for the error discussed in Puchalski et al. (2011). This resulted in an annual deposition increase of 47%, indicating the importance of accurate NH_3 measurements for flux modelling.

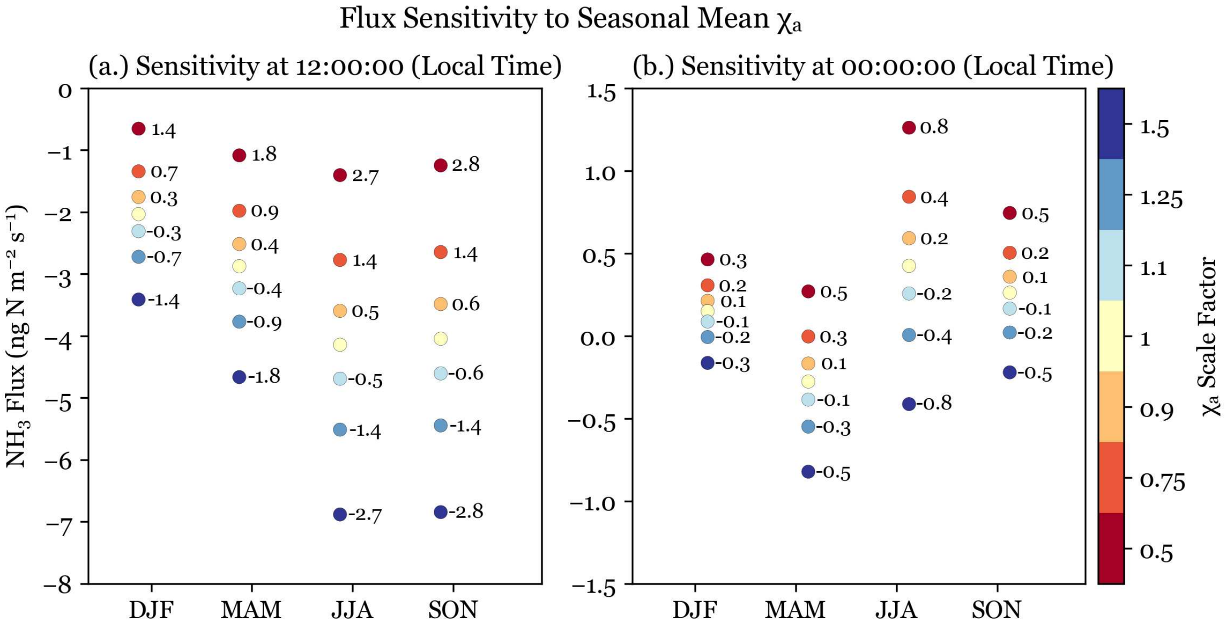

Figure A.7: NH_3 flux was simulated using Massad et al. (2010) using the mean seasonal meteorological parameters, mean seasonal NH_3 concentration at (a.) 12:00:00 and (b.) 00:00:00, and scaled NH_3 concentrations. Points are colored by scale factor applied to the NH_3 concentration. Colors are shown in the right hand justified colorbar. Difference to the mean concentration simulation values are listed next to each point (ng N m^{-2} s^{-1}).

A.6 Sensitivity to u* and L

We conducted two case studies to probe the importance of u* and Obukhov Length on simulated aerodynamic resistances. In case study 1 (2), friction velocity (Obukhov Length) from ERA5 was replaced with the value from NEON (see Figure A.8). This isolates the impact on R_a from each of the given parameters. In Figure A.8a and b, we see that the relative impacts of Obukhov Length and u* on Ra aresubstantial. Considering the simulated fluxes in Figure A.8c. we see that flux simulations with ERA5 meteorology inputs are more sensitive to changes in u* than L. InFigure A.8a. calculated Ra values are all below 30 s m^{-1} when using u* from NEON. This is likely due to the minimum u* value of 0.2 set by NEON.

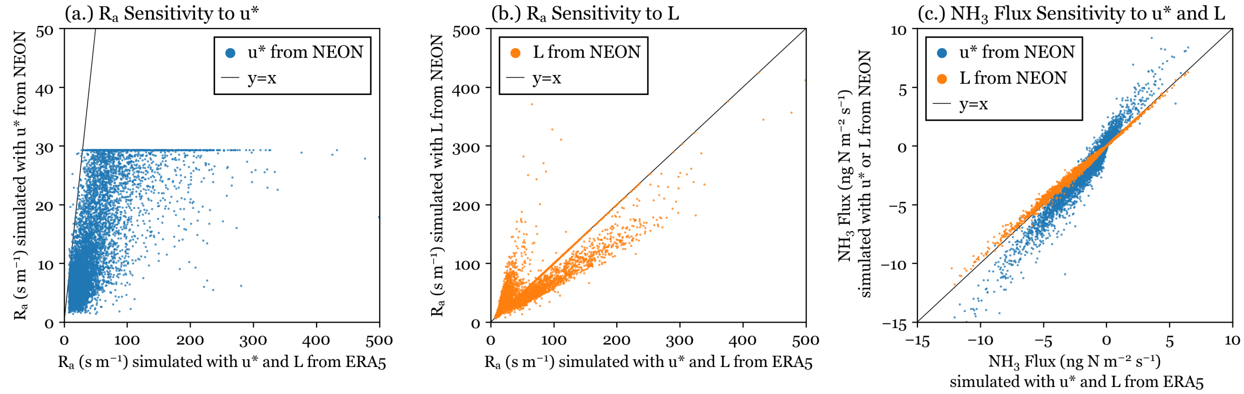

Figure A.8: R$_a$ simulations using ERA5 meteorology are compared to R$_a$ where (a.) u* and (b.) Obukhov Length, have been replaced with *in situ* values from NEON. (c.) NH$_3$ fluxes are compared where u* and L have been replaced with *in situ* values from NEON.

A.7 Folliage measurements

Measurements of foliage from the NEON site were used to determine the stomatal emission potential. At the NEON site, due to experimental constraints, foliage was collected in locations adjacent to the NEON tower footprint by CSU staff. Five trees were identified for each of the three primary overstory and understory species, for a total of 15 trees. Foliage samples were collected seasonally beginning in the summer of 2021. During each sampling event, 30 g of needles or leaves were collected from each tree by hand, where accessible (preferred) or using a slingshot method to collect a small branch from overhead. Samples were stored in Ziploc bags and shipped overnight to the EPA laboratory in a cooler with ice packs. Litter and foliage samples were processed and analyzed for pH and NH_4^+ by the EPA as follows. 5.0 g of fresh material is subsampled from the plot-level composite sample, ground in liquid nitrogen using a mortar and pestle and small coffee grinder, then extracted with 25 mL of deionized water. pH is determined directly on the extracts. [NH_4^+] in the extracts, which reflects the bulk tissue concentration, is determined by ion chromatography after separation of the NH_4^+ from the solution as NH_3 using headspace equilibration. For the headspace method, 5 mL of tissue extract is added to a 250 mL high-density polyethylene jar containing two ALPHA passive samplers (Center for Ecology and Hydrology; Tang et al., 2001), without the diffusion barrier, affixed to the interior of the lid. The jar is sealed, and 5 mL of 0.3 N NaOH is added to the extract via septum. NH_3 liberated from the liquid extract into the headspace is collected by the passive diffusion samplers over a period of 48 hours, after which the passive sampler is extracted with 10 mL of deionized water. NH_4^+ in the extracts is determined by ion chromatography. To determine the stomatal emission potential, the weighted mean of Γ_{st} was calculated using the percentages of evergreen forest and deciduous forest from the NEON site survey (NEON, 2025). The resulting Γ_{st} was 29.

Appendix B

Novel Quantification of Phosphate Wet Deposition by Flow Injection Analysis

B.1 Contaminated wet deposition sample

The wet deposition samples flagged as contaminated had visible debris. One of the samples, shown in Figure B.1, was yellow compared to the uncontaminated duplicate sample.

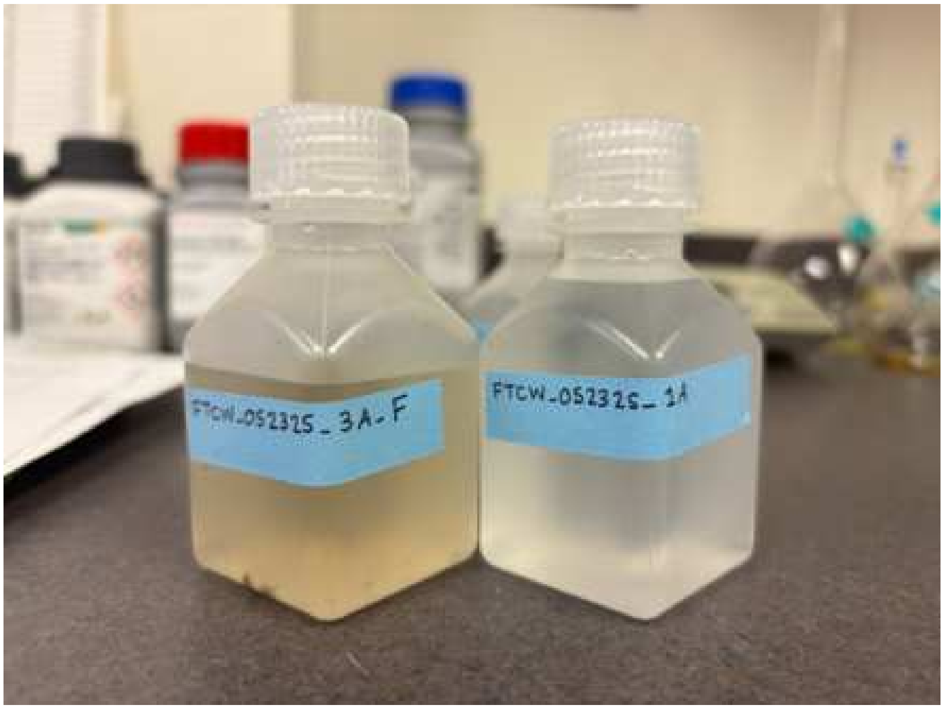

Figure B.1: Wet deposition samples from May 23, 2025, are shown. The left bottle was flagged as contaminated due to debris.